Precision tuning of silicon photonic devices using multi-shot femtosecond laser irradiation and characterization of incubation effect in multi-shot femtosecond laser irradiated silicon

by

Ruoheng Zhang

A thesis submitted in partial fulfillment of the requirements for the degree of

Doctor of Philosophy

in

Photonics and Plasmas

Department of Electrical and Computer Engineering
University of Alberta

Abstract

Silicon photonics has emerged as a promising platform for advanced on-chip integrated optical devices and advanced microelectronic circuits during the last decades. Due to its extreme sensitivity to fabrication precision and tolerance, a post-fabrication tuning method is typically required to correct phase errors in silicon photonic devices to achieve the resonant frequencies of interest. One of the most promising techniques is by applying the femtosecond (fs) laser to modify the refractive index of silicon, as it does not require additional material or processing steps. So far, in this method, only single-shot fs irradiation has been demonstrated, which still lacks precise control of the refractive index changes. A multi-shot approach, which takes advantage of the incubation effect, was investigated in this thesis to achieve precision tuning.

By applying multi-shot 130 fs laser irradiation at 800 nm wavelength, permanent tuning of resonance wavelengths for silicon microring resonators (SiMRR) with both positive shift and negative shift are achieved. The resonance wavelength spectra were obtained by a characterization system using a tunable laser and a power meter. Three regions ("increasing," "plateau," and "decreasing") exist in a fluence dependency tuning curve when the resonance wavelength shift is plotted as a function of laser fluences for a given number of pulses used. The formation of these regions depends on the relative contribution of the crystalline modification or ablation process.

An improved laser tuning platform was developed to demonstrate the high precision permanent tuning of silicon photonic devices. The platform consists of an irradiation system utilizing 800 nm fs laser pulses, allowing the resonance wavelength of the Si photonic device to be tuned in real time to the desired value, and a character-

ization system utilizing a Superluminescent Diode (SLED) and an optical spectrum analyzer (OSA). The use of SLED and OSA led to an order of magnitude speed improvement in obtaining the resonance wavelength spectra. The platform was used to measure the shot-to-shot tuning response of SiMRRs. Five regions ("insignificant change", "increasing", "plateau", "slow decreasing" and "fast decreasing") exist in a shot dependency tuning curve, when the resonance wavelength shift is plotted as a function of pulse numbers at a given laser fluence. Precision permanent tuning of SiMRRs was demonstrated through a multi-shot approach using 50 fs laser pulses at 800 nm wavelength with sub-microjoule pulse energies. Unprecedented fine-tuning of the microring resonance wavelength at a resolution of 2.5 pm per laser shot was achieved at a low laser fluence of 23.2 mJ/cm^2. This represents a 20 x finer resolution and 4 x lower fluence than previously demonstrated using single-shot femtosecond laser tuning. The low energy requirements allow for the use of compact, low-cost lasers for tuning.

Femtosecond laser pulses at low fluences can modify materials even when there is no visible damage; thus, the processes are difficult to characterize. The accumulated modifications due to these low fluence fs pulses eventually resulted in visible damage to the materials. Such a multi-shot low fluence process is commonly called the incubation effect. The detailed processes of the incubation effect are not well understood. In this thesis, the details of the incubation effect in multi-shot irradiated Si were studied using surface characterization methods and the refractive index changes in SiMRRs.

Multi-shot ablation thresholds, $F_{th}(N)$, for single crystalline silicon irradiated with 800 nm 130 fs laser pulses were investigated for fluences above ($F > F_1$) and below ($F < F_1$) the single shot ablation threshold F_1. It was observed that the ablation threshold for N shots $F_{th}(N)$ in the case of ($F < F_1$) is significantly larger than the case of ($F > F_1$). The critical minimum fluence or sub-ablation threshold of Si, when no ablation would result even with an infinite number of laser shots, was estimated. Multi-shot ablation thresholds for 250 nm Si thin film irradiated with 800

nm or 400 nm 130 fs laser pulses were also investigated. For the 800 nm irradiation, it was observed that the F_1 for the thin film Si is lower than the bulk Si, but their incubation coefficients are consistent with each other. It was also observed that the incubation effect is weak for the Si thin film under 400 nm irradiation.

The silicon microring resonator was utilized as a novel tool to obtain information about the incubation effect dynamics at laser fluences well below thresholds for modifications that can be detected using conventional surface characterization methods. From the shot-to-shot refractive index changes measured by SiMRRs at a given irradiated laser fluence, three pulse-number-thresholds (N_{th}) can be determined from low to high pulse numbers as: "defect generation threshold," "nano milling threshold," and "ablation Threshold." These N_{th} decrease with increasing laser fluence. The SiMRR results also confirm that the incubation effect is weak for the Si under 400 nm irradiation.

Preface

This thesis is an original work by Ruoheng Zhang. Some of the research in this thesis derives from collaborative works with researchers from University of Alberta. The research works in Chapter 4 were led by my supervisor Prof. Ying Yin Tsui with Prof. Frank Hegmann as the Major collaborator at University of Alberta, and in Chapter 5, the research work was also in collaborate with Prof. Vien Van. Chapter 6 and Chapter 7 was in collaborate with Prof. Vien Van and Prof. Robert Fedosejevs, and led by Prof. Ying Yin Tsui, where the experiments on laser irradiation side are mainly inspired by Prof. Tsui and Prof. Robert Fedosejevs, and the related analysis on silicon photonics side are inspired by Prof. Vien Van. The data analysis work in chapter 8 are inspired by Prof. Tsui. The thesis introduction part in Chapter 1, the part of research background in Chapter 2 and Chapter 3, and the summary and future work in Chapter 8 are my original work.

Most of the materials in Chapter 4 of this thesis have been published in R. Zhang et al., "A study of incubation effects in femtosecond laser irradiation of silicon and copper", Applied Physics A, (2023) 129: 131, with the exception of section 4.4.3 and 4.5. I was responsible to design the laser irradiation experimental setup, conducting the experiment and analyse the experiment results. Prof. Tsui provided me advices on the experiment and date analysis. Prof. Hegmann and his master student, Mr. Aran McDowell helped me with setting up the experiment setup with femtosecond laser source in his lab. Prof. Robert Fedosejevs gave suggestions on the draft of the manuscript. All the authors contributed to the discussion and writing of the manuscript.

Chapter 5 of this thesis has been published in Optics communication as R. Zhang et al., "Multi-shot near-infrared femtosecond laser tuning of silicon microring resonators.", Optics Communications 560 (2024): 130446. I was responsible of conducting optical characterization on the sample resonators before and after laser irradiation, loading expeirments on each of the silicon deviced and analyse the experimental data. Dr. Hanfa Song and Mr. Bo Leng helped me with the optical charaterization procedures on partial of the silicon photonics devices. Prof. Tsui gave advices on the experiment planning and experiment data analyzing. Prof. Vien Van Inspired me on the optical characterization and data analysis, and gives comments on the tunning experiments. Prof. Hegmann assisted me with the femtosecond laser source in his lab. Prof. Robert Fedosejevs gave suggestions on the draft of the manuscript. All the authors contributed to the discussion and writing of the manuscript.

Acknowledgements

I would like to thank everyone who has helped me with the work described in the thesis and during my Ph.D program. First and foremost, I would like to thank my supervisor, Dr. Ying Yin Tsui, for accepting me into his group and guiding me throughout my research work. During my research, he provided me with intellectual freedom in my work, supported my attendance at conferences and collaborative projects, encouraged me to get new ideas, and gave me suggestions on getting high-quality work. I also want to thank my committee members, Dr. Robert Fedosejevs and Dr. Vien Van for their interest in my work, for supporting me in using the laser and analyzing equipment from their lab as well as giving me suggestions on my experiments. I also would like to thank Dr. Frank Hegmann for allowing me to use the laser and conduct experiments in his lab for several months, which helped me carry through a difficult time for my project.

Additionally, I would like to express my appreciation for all the help and support from my fellow labmates and collaborators. The NanoFab staff were helpful and trained me on the various tools and processes I would need to learn to characterize my sample and fabricate photonic devices. I appreciate the help and advice I got from all our ultrafast laser research Lab members and collaborators, including Henry, Andrew, Mathew, Nick, Tanu and all the fellows who contributed to my work. I would also like to thank all the collaborators I have worked with on all the projects I have attended. I enjoyed working with them and gained much knowledge throughout the process. Finally, I would like to thank my family and my wife for all the support and love they gave me throughout the years.

Table of Contents

List of Tables

List of Figures

List of Symbols

Latin

D	Diameter
F	Fluence
N	Pulse Number
n	Index of refraction
R	Reflectivity
S	Incubation Effect
w	Beam Radius

Greek

α	absorption coefficient
λ	Wavelength
τ	Pulse duration

Abbreviations

AFM Atomic force microscope (or microscopy).

CCD Charge Coupled detector.

CPA chirped pulse amplification.

ECE Department of Electrical and Computer Engineering.

FCA Free-carrier absorption.

FSR Free spectra range.

FWHM Full width at half maximum.

GBLT Gaussian beam limiting technique.

HAZ Heat-affected zone.

MPA Multi-photon absorption.

NanoFab Nanofabrication Facility in the ECE Dept. at the U of A.

NIR Near-infrared.

NVM Nevermind.

OM Optical microscope (or microscopy).

SEM Scanning electron microscope (or microscopy).

SiMRR Silicon Micro Ring Resonator.

SOI Silicon on Insulator.

SPIC Silicon photonic integrated circuits.

TOF Time-of-Flight.

TPA Two-photon absorption.

U of A University of Alberta.

Chapter 1

Introduction

1.1 Background

In the last 20 years, ultrashort-pulsed laser systems have gained popularity in both scientific and industrial fields. These systems have a very short pulse duration, either in picoseconds or femtoseconds, which allows for precise and quick energy deposition while reducing the size of the heat-affected zone compared to longer pulse lasers. Especially, when using multiple femtosecond laser pulses to irradiate a sample on the same spot, the ablation thresholds depend on the number of irradiated pulses. According to the so-called "incubation effect," the multi-shot ablation threshold can be significantly lower than the single-shot ablation threshold [1]. The multi-shot approach can provide "more gentle ablation" for many applications. For example, ultra-high precision nanomilling of copper to a depth of 2 nm using 500 near-infrared (NIR) femtosecond (800 nm, 125 fs) pulses at a fluence three times below single shot ablation threshold fluence was demonstrated [1]. Another application that this thesis is focused on is the post-fabrication correction of fabrication deviation of silicon photonic integrated circuits.

Silicon photonics is a promising platform for advanced on-chip integrated optical devices and advanced microelectronic circuits. Silicon photonic integrated circuits (SPIC) typically consist of waveguide components such as couplers, Mach-Zehnder interferometers, microring resonators, gratings, etc., whose optical responses(typically

resonant frequencies) need to be accurately controlled for the proper operation of the whole circuit. Current fabrication methods for Silicon PICs are using standard CMOS processes from the semiconductor industry, while the process variations across a wafer (or even a die) cause device dimensions and material parameters to deviate from specifications, resulting in sub-optimal operation or even failure of the device. These process variations are currently unavoidable (e.g. better than 1 nm control of all waveguide dimensions is required for proper operation) and therefore it is necessary to tune the device characteristics after fabrication in order to restore the proper operation of the device.

General approaches to post-fabrication tuning of silicon photonics devices indlude: thermal and permanent tuning methods. The thermal tuning method is the most common approach currently, which provides a temporary change of index refraction due to the thermo-optic effect. Permanent modification of the index refraction is a more desirable approach, as it can be energy and cost efficient. However, most of the existing methods are still at the exploratory stage. One approach to permanently correct the fabrication errors is to use ultrafast laser-induced crystalline modifications and ablation [2–4]. The approach successfully demonstrated post-fabrication tuning of various photonic devices using NIR or Violet single pulses at various fluences. One niche application for the silicon micro-ring resonator that this thesis is focused on is to use it to better understand the dynamics of incubation effects in silicon generated by multiple femtosecond pulses with low fluences significantly below their melting thresholds.

Currently, the characterizing of laser damage or ablation thresholds is mainly based on using optical microscopy or Scanning Electron Microscopy (SEM) techniques to inspect the areas of samples after irradiation with energy fluences above the damage or ablation thresholds. Such an approach is especially insufficient for studying the evolution of incubation effects since there are no detectable damage areas for most of the shots. Because of its ability to detect very small refractive changes, the silicon mi-

croring resonator was used to detect crystalline modifications due to laser irradiation even at fluences significantly below single-shot ablation thresholds[5].

1.2 Research objectives and thesis overview

In this Ph.D. thesis, I have focused on two main research areas. A multi-shot approach based on the incubation effects has been developed in the first area for post-fabrication tuning of silicon photonic devices. An online characterization system has been built to perform a shot-to-shot measurement of the tuning process immediately after each laser shot. Such a system allows the "real-time" monitoring of the multi-shot radiation process, leading to fine-tuning with unprecedented resolution. In the second area, a detailed investigation is carried out to investigate the incubation effects using conventional and novel methods. The novel method applies an online characterization system to gain information about the dynamics of incubation effects during laser irradiation by using a microring resonator to measure the shot-to-shot refractive index changes. The organization of this thesis is described in the next paragraph.

In addition to this chapter, the rest of the thesis is divided into 7 chapters. Chapter 2 will present some aspects of the fundamental theory of femtosecond laser interaction with silicon, specifically focusing on the incubation effects. It will also provide details about the experimental setup of the femtosecond laser system, the laser irradiation system, and the details of the samples used in the experiments. Chapter 3 will present the principle of silicon microring resonators, fabrication method and femtosecond laser tuning technique for silicon photonics. Chapter 4 will study the incubation effects based on observing silicon and copper samples' sub-single-shot threshold irradiation behaviour. In particular, the "critical fluence" thresholds were estimated using a binary method. For a material irradiated with laser fluences below its "critical fluence" threshold, no damage can be resulted even after a significant amount of laser shots. Chapters 5 and 6 focus on the multishot femtosecond laser tuning of silicon microring resonators. In Chapter 5, the results from the multi-shot tuning of SMRR with

very low laser fluences will be discussed. The results were obtained using irradiation setups and characterization setups in two different laboratories. In Chapter 6, the refined results of using the online characterization system for multi-shot fine-tuning of SMMR will be discussed. The online characterization system was developed by combining the irradiation and characterization setups in one setup. In Chapter 7, the application of the online characterization system to gain information about the dynamics of incubation effects during laser irradiation with near infra-red (NIR) or violet light by using a microring resonator to measure the shot-to-shot refractive index changes will be discussed. Lastly, in Chapter 8, an overall summary highlighting the main results of this PhD thesis and a recommendation for future study opportunities will be provided.

Chapter 2

Femtosecond laser and Silicon Interactions

2.1 Background

Several femtosecond laser silicon interaction processes are relevant to this thesis. They include the modification of the refractive index, melting, ablation and incubation effect. The melting and ablation processes in laser silicon interaction received the most attention and less for refractive index modification and the incubation effect. Especially, the details of the incubation effect are poorly understood.

2.2 Theory and Experiment of Femtosecond Laser and Silicon Interactions

When femtosecond laser pulses come into contact with the surface of a silicon sample, photons interact with its electrons. This causes an increase in the excited electron density and electron system temperature to a critical value in less than a picosecond, which can lead to the "melting" of the silicon structure. The melting can happen in two ways: by coupling enough energy from the electron system into the lattice system, driving the lattice temperature to the melting point, or by disassembling the lattice structures due to the removal of many electrons from their bonding states. If enough energy is provided to the system, ablation will occur, causing material to be removed from the surface. In this PhD thesis, femtosecond laser pulses with 400 nm

or 800nm wavelengths were used, so the focus will be on the melting and ablation mechanisms for these two wavelengths.

As the laser beams interact with silicon, the electrons in silicon usually absorb the energy from the laser since they are lighter than the ions and more susceptible to the laser field. For femtosecond laser ablation in visible to NIR wavelengths, one-photon and multi-photon absorption are the two main ways electrons get excited. One-photon absorption happens when a photon's energy exceeds the band gap between the valence and conduction bands. A photon of 3.1 eV at 400 nm can be directly absorbed by an electron in Silicon. This absorption type is also known as "linear absorption" since the absorption coefficient varies linearly with the intensity. When a photon's energy is below or closer to the bandgap energy of silicon (1.12eV), such as in irradiation at 800 nm, multi-photon absorption (MPA) can occur. MPA is a non-linear process that requires the photons to be absorbed by a single atom before they decay from the transient state back to the original or another transient state. For our case when 800nm femtosecond laser pulses interacting with crystalline silicon, it is commonly believed that the two photon absorption dominated during the process, together with partial of the linear absorption. The linear absorption coefficient α and two photon absorption coefficient β reported by several literatures are set to be 1×10^{-5} and 1cm/GW, respectively[6–9] . The penetration depth for two photon absorption is typically $\sim$ 50 - 110 nm[10, 11].

The avalanche ionization can also play a role. It is induced by two excitation mechanisms: Free Carrier Absorption (FCA) and Impact Ionization. FCA is the process of coupling photons to conduction band electrons, continuously colliding with an ion core or a lattice vibration to transfer energy to electrons in the valence band. This is also known as electro-photon-phonon collision. When the conduction band electron gains energy greater than 2 times the bandgap energy, the collision can yield two electrons with energies just above the band gap energy, which is called impact ionization (electron-electron collision). These two processes repeatedly energize the conduction

band electrons and potentially increase the conduction band electron density, leading to a breakdown of the material.

At a wavelength of 400nm and 800nm, the linear absorption and two-photon absorption dominate for the conduction band electron generation respectively, and the avalanche ionization is smaller in comparison. As the density and temperature of excited electrons increase to a critical value, the breakdown of silicon structures will happen consequently. Generally, the material response includes two pathways: thermal melting and non-thermal melting. For a thermal pathway, electron systems will couple energy to the lattice system via electron-phonon coupling and drive the temperature of lattices to the melting point. A thin layer of material transforms into a liquid state, and the melting depth increases with laser energy. After irradiation, re-solidification occurs in several nanoseconds when the generated molten layer conducts heat away to the substrate driven by the thermal gradient. A fast re-solidification-front speed (larger than liquid to crystal relaxation rate 15m/s) will limit atoms from finding their equilibrium position and yield an amorphous silicon structure, and a slower re-solidification speed will lead to a crystalline layer. As for the non-thermal pathway, the breakdown of structures depends on the achievable conduction band electron density, where the excitation of electrons from their bonding states in the valance band and the generation of high-density plasma will affect the stability of silicon lattice, corresponding to the phase transition of silicon. This is also called cold melting and usually occurs on a shorter time scale than thermal melting. Distortion and dislocation in the lattice structures can be achieved during this process, while the amorphous silicon region (Heat-affected zone) is often found to be much smaller compared to the thermal process[12, 13].

At higher laser fluences above the ablation threshold, the irradiated silicon experiences a rapid expansion upon melting, which causes a rarefaction wave to travel through the melted silicon and can lead to a small amount of material being ejected from the surface. Various mechanisms such as vaporization, coulomb explosion, explo-

sive boiling or phase explosion by superheating can occur depending on the conditions of the incident laser pulses[14–18]. It was also believed that the strong laser ablation is attributed to phase explosion, while the gentle ablation is governed by Coulomb repulsion[19]. The experiments described in the thesis mainly focused on low fluences, which are close to or much lower than the single-shot ablation threshold. With the peak fluence close to the ablation threshold, a large portion of the laser beam has fluences below the ablation threshold. It is believed that at low fluences slightly below the ablation threshold, both the thermal melting and fast non-thermal melting can exist[9, 12] resulting in crystalline and amorphous regions in the heat-affected zone. Since the refractive index of the amorphous silicon ($n_{amouphous}$ = 3.73 @ 1550nm) is slightly higher than that of crystalline silicon($n_{crystalline}$ = 3.45 @ 1550nm)[20], it results in a small change in the overall refractive index of the heat-affected zone. Even when the peak fluence is significantly below the ablation and melting thresholds, refractive index changes are observed in the heated affected zone[5]. The refractive index likely originates from laser-induced distortions and defects in the crystal structure.

Multi-pulse material processing is especially complex due to the incubation effect, as the material's optical characteristics may change by each pulse[13], and the details of the incubation effects are poorly understood currently.

2.2.1 Single-shot melting and Ablation Thresholds

Gaussian beam limiting technique (GBLT), D-square method, or Liu's method[33, 34] is the most often used method for measuring damage, melting and ablation thresholds. In the GBLT, the ablation threshold fluence can be determined by plotting the squared crater diameter (D^2) against fluence (F). The data is extrapolated to $D^2 = 0$ to obtain the ablation threshold fluence. The measurement is usually conducted with fluences higher than the ablation threshold. Optical microscopy, Scanning Electron Microscopy (SEM) or Atomic Force Microscopy (AFM) are commonly used to de-

Table 2.1: Single shot ablation threshold F_{th} for silicon and the relevant experiment conditions. The silicon conditions are: X: crystalline, N: n-type; **T** is the material thickness; τ is the reported Gaussian FWHM pulse width; w is the e-folding elertric field beam radius. Env. is the background gas pressure, λ is the laser wavelength, and R is the percentage reflectivity of silicon. The detector methods are discussed in the text.

Cond.	**T**	τ (fs)	**Env.** (Torr)	λ (nm)	**R** (%)	$F_{th}(1)$ (J/cm^2)	w (µm)	**Det.**	**Ref**
N(111)	bulk	5	1×10^{-4}	780	33.1	0.2	15	GBLT	[7]
N(111)	bulk	25	1×10^{-4}	780	33.1	0.17		GBLT	[21]
Crystal	bulk	100	1×10^{-7}	780	20.8	0.15	316	TOF	[22]
Crystal	bulk	120	1×10^{-7}	780	33.1	0.3	160	TOF	[23]
N(111)	bulk	400	1×10^{-4}	780	33.1	0.28		GBLT	[21]
N	bulk	85	Air	786	33	0.158	20-120	AFM	[24]
N	bulk	200	Air	786	33	0.238	20-120	AFM	
N	bulk	633	Air	786	33	0.24	20-120	AFM	
N	bulk	1000	Air	786	33	0.362	20-120	AFM	
X	bulk	130	1×10^{-1}	790	33	0.15	6.7	SEM	[14]
X(100)	bulk	120	Air	800	32.9	0.21	8	GBLT	
X(100)	bulk	120	Air	800	32.9	0.11	24	GBLT	[25]
N(111)	bulk	130	Air	800	32.9	0.26(Melting)	50	GBLT	[7]
N(111)	bulk	130	Air	800	32.9	0.55(Ablation)	50	GBLT	
N(111)	bulk	130	Air	800	32.9	0.27(melting)	51	GBLT	[6]
N(111)	bulk	130	Air	800	32.9	0.41(annueling)	51	GBLT	
N(111)	bulk	130	Air	800	32.9	0.58(ablation)	51	GBLT	
X(100)	bulk	120	1×10^{-8}	800		0.15	100	TOF	[26]
X(100)	100um	150	Air	775		0.25	300	GBLT	[27]
N(111)	Bulk	60	Air	800		0.27	2.3	GBLT	[28]
N(111)	Bulk	40	Air	790		0.28	80	GBLT	[29]
X	Bulk	100	Air	800		0.25	69	SEM	[30]
N(111)	Bulk	10	1×10^{-3}	800		0.297		GBLT	[31]
N(111)	Bulk	30	1×10^{-3}	800		0.329		GBLT	
N(111)	Bulk	250	1×10^{-3}	800		0.405		GBLT	
N(111)	Bulk	550	1×10^{-3}	800		0.518		GBLT	
Crystal	Bulk	100	Air	800		0.25	69	GBLT	[30]
Crystal	Bulk	150	Air	800		0.156		GBLT	[32]

termine the crater diameters, which define ablation by the "appearance" of ablation spots in achieved SEM or AFM images. Another method is the pump-probe reflectivity technique, which defines the melting threshold as the fluence where the reflectivity reaches that of liquid silicon. Time-of-flight (TOF) technique defines ablation at the intercept of zero ion expulsion when analyzing the ion flux relationship with the incident fluence. In the literature, damage, melting or ablation threshold are often used interchangably, where the ablation threshold being most commonly used one. Table 2.2 shows the reported single-shot melting and ablation thresholds for silicon irradiated with visible or NIR femtosecond pulses. From Table 2.1, the average values for the ablation thresholds determined by GBLT for pulse durations less than 100 fs and in the range between 100 - 200 fs are 0.27 J/cm^2 and 0.33 J/cm^2 respectively. These values can be used for comparison since the pulse duration of 130 fs or 50 fs and the GBLT technique are used in this thesis.

2.2.2 Multiple-shot Ablation Threshold and Incubation Effect

It is well established that the multi-shot threshold reduces with the increase of pulse number N [35–37], and the effect is commonly referred to as "Incubation Effect". Currently the detailed mechanism of incubation effect is still not well-understood. It is beleived that the each of femosecond laser pulses well below single-shot ablation threshold may slightly modify the material properties, such as creating defects in the interaction region, and subsequently led to the lowering of the damage threshold. A number of models have been developed to describe the incubation effect. The most simple model assumes the N-shot ablation threshold fluences $F_{th}(N)$ is related to the single-shot ablation threshold fluence $F_{th}(1) = F_1$ by a power law [38], where

$$F_{th}(N) = F_1 N^{S-1} \tag{2.1}$$

The model assumes that there is a free parameter called the "Incubation coef-

ficient" (S) that is enough to describe the incubation effect for each material. The incubation coefficient S can be regarded as a quantitative index, where a smaller value of S indicates a stronger incubation phonomenon during processing, while when S =1, it shows that there is no incubation phonomenon occurs inside the material. A simple power-law model was found to provide a reasonable fit to experimental multi-shot ablation thresholds for many materials. The incubation coefficients were determined for various materials, including metal, semiconductor, polymer, and others. The multi-shot ablation thresholds and incubation coefficients for silicon from the literature are summarized in Table 2. The single-shot ablation thresholds are consistent with those in Table 2.2. The reported incubation coefficients S are narrowly ranged between 0.82 - 0.84.

It is reasonable to assume that there exists a critical laser fluence for each material, below which no ablation can occur even with an infinite number of shots. This critical laser fluence is called the "sub-ablation threshold" (F_∞). An attempt was made to improve the previous power law model by adding the F_∞ term to capture this effect. However, measured experimental data did not agree with the model very well in many cases.

A more sophisticated model, proposed by Zhanliang and Wolfgang et al.[39], is called the "generic incubation model". It takes into account F_∞ and the change of absorption. The model proposes that there is a decrease in the critical energy needed to damage the surface after each shot. It is assumed that the threshold fluence can be determined by the critical energy density, G, deposited in a skin depth of $1/\alpha$ from the previous pulse, where α is the absorption coefficient.

$$F_{th}(N) \approx \frac{G(N-1)}{\alpha(N-1)} \tag{2.2}$$

The fluence F, and pulse number N, dependent absorption coefficient, α, and critical energy, G, can be expressed as

$$\alpha(N,F) = \alpha_0 + \Delta\alpha\left(1 - e^{-\beta FN}\right) \tag{2.3}$$

and

$$G(N,F) = G_0 + \Delta G\left[1 - e^{-\gamma FN}\right] \tag{2.4}$$

Here, G_0, α_0, ΔG, and $\Delta\alpha$ represent the initial values for the critical energy, absorption and their corresponding maximum change, respectively. β and γ are two parameters, where β describes the efficiency of absorption coefficient change toward maximum value at a given fluence F, while γ is the coefficient for critical energy change. The final expression of threshold fluence can be given as

$$F_{th}(N,F) = \frac{F_1 - \left[F_1 - F_\infty\left(1 + \frac{\Delta\alpha}{\alpha_0}\right)\right]\left[1 - e^{-\gamma F(r)(N-1)}\right]}{1 + \frac{\Delta\alpha}{\alpha_0}\left[1 - e^{-\beta F(r)(N-1)}\right]} \tag{2.5}$$

Note F_{th} becomes F_∞ as N approaches infinity. The free material parameter $\Delta\alpha/\alpha_0$, β, and γ can be obtained by solving the nonlinear least-squares curve fitting problem using the experimental data. The model has been compared to the experimental data in literature ranging from metal to dielectric, showing that the generic model can fit better than the simple power-law model, especially with larger pulse number [34, 40–43]. However, no data for silicon with 800 nm or 400 nm femtosecond laser irradiation was found.

The details on microscopic mechanisms for incubation effects in laser-irradiated silicon are poorly understood. The incubation effects are likely related to the evolution of defects generated by femtosecond laser pulses with low fluences. Using Near-infrared femtosecond laser pulses, various laser-induced defects and phase transformations were studied by single and multi-shot irradiation of single crystal silicon with fluences above the melting threshold [14, 44, 45]. The authors in [45] used various numbers of pulses at $0.15 J/cm^2$, about 15% above the single shot melting threshold, with a wavelength of 1030 nm and a pulse width of 300 fs. For irradiation with a single shot, it was observed that a top layer of amorphous silicon where the

laser fluences are sufficient for melting and a dislocation layer underneath where the laser fluences are below the melting threshold but sufficient to induce dislocations and lattice distortions were generated. As the number of shots increased, the dislocation layer was enlarged, and a small portion of the amorphous silicon layer was removed. Further increase in the number of shots significantly increased the dislocation region, leading to the formation of a high-density defect layer and the appearance of macroscopic damage to the surface layer. The visible surface damage was in the form of Laser-Induced Periodic Surface Structures (LIPSS) and microholes, which would be accompanied by a relatively larger amount of material removal. The laser fluences used in this PhD thesis were significantly below the melting threshold, but the mechanisms observed in [14, 44, 45] may still provide useful insights.

2.3 Femtosecond Laser Irradiation Experimental Setups

In the thesis, femtosecond laser pulses with a wide range of laser fluences from slightly above the single shot ablation threshold to an order of magnitude below the threshold were used to irradiate the silicon, copper or silicon microring resonator samples. The laser systems used for these studies will be described below.

2.3.1 Femtosecond laser systems

Three commercial regeneratively amplified Ti: Sapphire femtosecond laser systems are used in this thesis research: the "Amplitude" laser system, the Coherent "Legend" system and the Spectra physics "Hurricane" system. Although the output properties of the laser systems vary between different systems, the fundamental pulse generation and the components are more or less similar to each other. The Amplitude laser system is a Ti: Sapphire laser based on the chirped pulse amplification (CPA) technique (Fig. 2.1). The chirped pulse amplification method is applied to avoid optical element damage when amplifying the pulses, where the pulses are firstly

Table 2.2: Table of multi-shot ablation thresholds and incubation coefficient for silicon and the relevant experiment conditions. The silicon conditions are: N: n-type; **T** is the material thickness; τ is the reported pulse width is Gaussian FWHM pulse width; $F_{th}(N)$ is the threshold corresponding to the specific pulse number N. Env. is the background gas pressure, λ is the laser wavelength, and R is the percentage reflectivity of silicon. S is the incubation coefficient value for the basic incubation model. The detector methods are discussed in the text.

Cond.	**T**	τ (fs)	**Env.** (Torr)	λ (nm)	$F_{th}(N)$ (J/cm^2)	**S**	**Ref**
N(100)	bulk	130	Air	800	$F_{th}(1) = 0.29$ $F_{th}(5) = 0.20$ $F_{th}(10) = 0.115$ $F_{th}(100) = 0.103$	0.84	[7]
N(100)	bulk	60	Air	800	$F_{th}(1) = 0.27$ $F_{th}(5) = 0.19$ $F_{th}(10) = 0.16$ $F_{th}(100) = 0.11$ $F_{th}(1000) = 0.08$ $F_{th}(10000) = 0.06$		[28]
N(100)	bulk	10	1×10^{-3}	800	$F_{th}(1) = 0.297$ $F_{th}(10) = 0.203$ $F_{th}(50) = 0.139$ $F_{th}(100) = 0.129$ $F_{th}(500) = 0.097$ $F_{th}(1000) = 0.092$	0.82	[31]
N(100)	bulk	30	1×10^{-3}	800	$F_{th}(1) = 0.329$ $F_{th}(10) = 0.228$ $F_{th}(50) = 0.172$ $F_{th}(100) = 0.155$ $F_{th}(500) = 0.120$ $F_{th}(1000) = 0.109$	0.83	[31]
N(100)	bulk	250	1×10^{-3}	800	$F_{th}(1) = 0.405$ $F_{th}(10) = 0.290$ $F_{th}(50) = 0.212$ $F_{th}(100) = 0.198$ $F_{th}(500) = 0.157$ $F_{th}(1000) = 0.140$	0.84	[31]

stretched by a grating to the nanosecond duration range to reduce their peak power, then amplified at the reduced power, and compressed back near to the original pulse duration using a grating near the output. The whole system is composed of different modules, each with a specific aim. A very low energy with a high repetition rate laser is generated from the Oscillator as the initial beam, going through each amplitude module. Two amplifying stages (MP0 and MP1) exist to achieve high enough gain, pumped by Inlite II amplitude laser and Powerlite Amplitude laser modules, respectively. The system operated at a 10 Hz repetition rate. In our experiment, we only applied the MP0 output as the laser source, generating an energy level of $\sim 20mJ$ with a pulse duration of 52 fs after the vacuum compressor.

The "Legend" and "Hurricane" run at a 1 kHz repetition rate and provide output energy of < 0.5 mJ, and a pulse duration of $\sim 130fs$. Both of these two systems have a similar lasing mechanism. Here we use "Hurricane" as an example to describe its components: The main component of the system includes an oscillator "Maitai" as a Seed laser, a Q-switched Nd-YAG laser system "Evolution" at 532.5 nm as a pump laser, and a regenerative amplifier(Fig. 2.2). The oscillator generates femtosecond pulses at 80 MHz with a selectable wavelength ranging from 750 nm - 800 nm. Amplification occurs when the seed laser passes through the Ti: sapphire solid crystal rod, which is excited by the pump laser. The regenerative amplifier is a folded cavity in which the input pulse is selected by a Pockels cell operating at a 1 kHz repetition rate. The output pulse then passes through the rod for ~ 13 times and is coupled out of the cavity by a second Pockels cell with a rotated polarization. The multiple passes through the rod result in a strong overall gain, where the seed laser of a few nJ can be amplified to 0.2 - 0.5 mJ.

2.3.2 Laser irradiation setup

The laser system used in most experiments reported in Chapters 4 and 5 are the two 0.5 mJ class, 130 fs, 1 kHz commercial regenerative amplified femtosecond Ti:

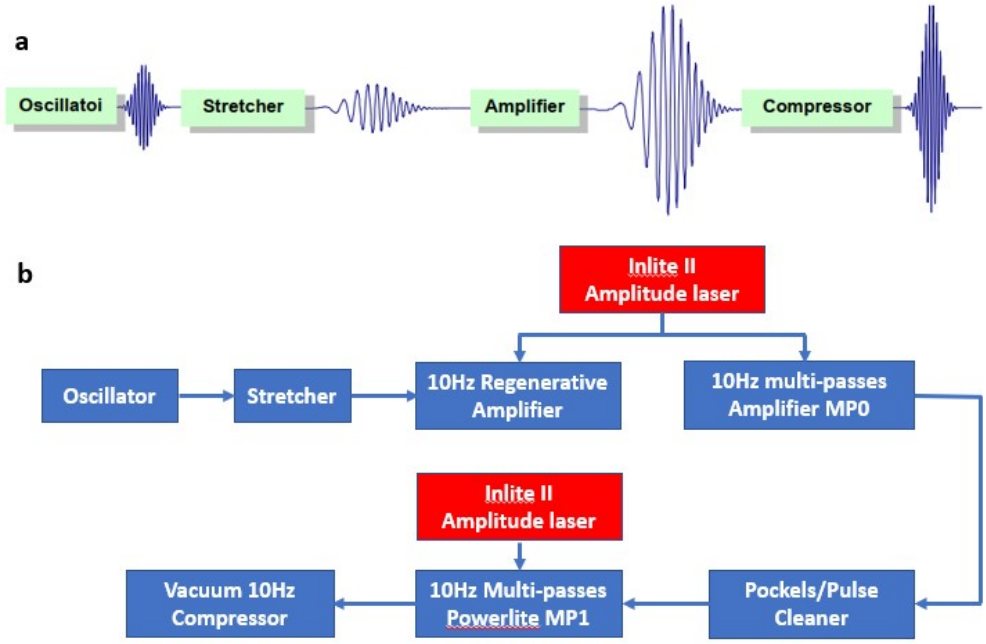

Figure 2.1: A scheme of "Amplitude" femtosecond laser system. (a) The simplest diagram of how the CPA technique works.(b) Laser block diagram of the "Amplitude" system.

sapphire laser systems ("Coherent Legend" and "Hurricane") (Fig.2.2). A commercial fiber-coupled spectrometer (Oriel USB2000) is used to examine the laser spectrum, yielding a bandwidth of 10 to 15 nm FWHM centered at 795 nm.

The experimental setup is shown in Fig. 2.3. All targets were mounted on a 3D motion stage with 200 nm resolution and irradiated at 0° angle of incidence. The incident laser goes through high reflect mirrors M1, M3, and M4, and is focused onto the sample using a 10 x long working distance microscope objective. The laser pulses with a wavelength of 400 nm are generated by removing M1, inserting M5 and passing through the BBO (Barium Borate) crystal to generate the Second harmonic frequency. A Gaussian-shaped spot can be obtained by positioning the target at focus. A semi-gaussian beam profile with a specific beam radius(such as 13.4 um in Chapters 5-7) can be achieved by moving the stage away by moving the target away from the focus position for a distance. In chapter 6 and chapter 7, when using

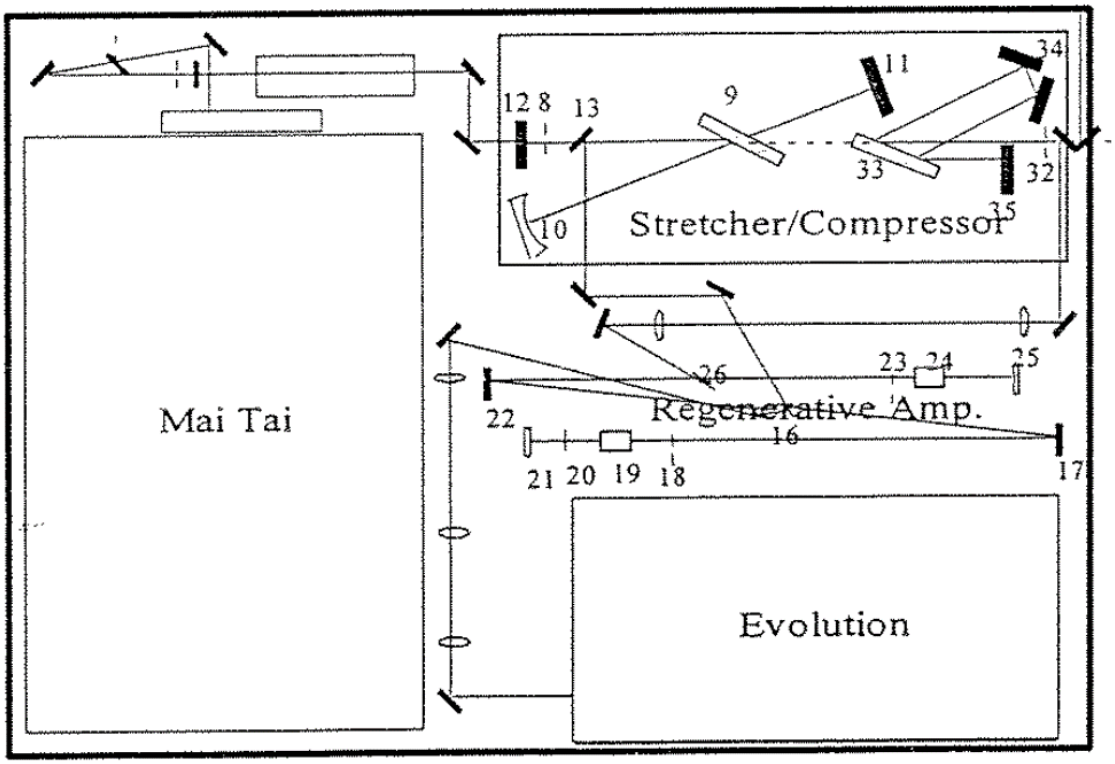

Figure 2.2: A scheme of "Hurricane" femtosecond laser system (will redraw later).

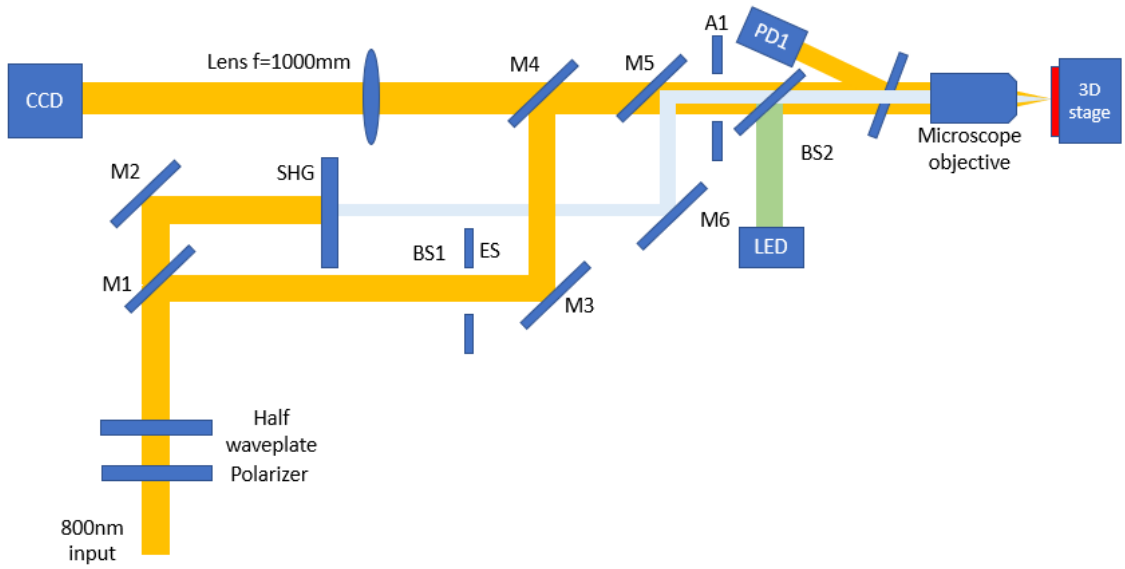

Figure 2.3: Laser irradiation system. M1-M6: HR mirrors at 400 nm and 800 nm, respectively, BS: Beam splitter. PD1: photodiode. L1: achromatic lens with 100 mm focal length.

the Amplitude TW laser system, the output of the top-hat beam from the laser system goes through several apertures, and we only picked up the middle part of the beam (8 mm in diameter) as the input laser source of our system. The beam profile distributed on our sample is actually an Airy pattern profile. The spot size measurement is determined by ignoring the relatively small outer rings of the Airy pattern and considering the central lobe with a Gaussian profile for approximation.

A CCD camera and a lens with a 100 cm achromatic focal length acting as a sample viewing system are employed to monitor where the beam is located on the sample surface, and a white light source LED is used for field illumination. The laser pulse energy is controlled by a combination of a half-wave plate followed by a Glan polarizer near the output of the laser, together with Schott NG absorbing glass filters. The higher order dispersion through these elements can be negligible, adding at most a few femtoseconds to the pulse width, and will not be considered in this work. The pulse energy is verified by several calibrated detectors. The turning angle for the half-wave plate will not exceed 30° to avoid pre-pulse while in our low energy fluence cases, the pre-pulse is not expected to perturb the sample prior to the arrival of the main pulse and the typical contrast ratio achieved was 5×10^{-3}. A fast photodiode PD1 (FND-100G) with a response time of < 1 ns was placed before the microscope objective for shot-to-shot energy measurements, and a Spectra-Physics Model 407A power meter with an accuracy of 10% is placed at the microscope objective in order to cross-calibrate the photodiode. The pulse-to-pulse energy fluctuation of the laser is recorded using a voltage follower and STM32 ADC board to the computer. The applied pulse energy is in the range of 0.01 uJ to 100 uJ. As for multiple shot irradiation, a combination of a fast electric shutter and delay generator is mounted in between the reflective mirror M1 and microscope objective to generate a specific number of shots required.

Both the top-hat and Gaussian beam profiles are applied to the experiment. The Gaussian beam with $1/e^2$ spot radius of 13.4 μm is generated by moving the target

away from the focus position by a distance of 400 µm.

2.3.3 Sample preparation and characterization

Several samples are employed in the experiment for threshold and incubation effect investigation. A commercial n-doped silicon sample with 1 mm thickness from University Wafer was diced into $10mm \times 10mm$ dimension pieces as silicon bulk samples, and the silicon thin film of 300 nm was fabricated using the LPCVD method. The poly-crystalline copper and Au thin films with 2 um in thickness are achieved through plasma sputtering deposition. All the fabricated samples mentioned above are carried out in the Nanofab of the University of Alberta. The SiMRR samples are used in experiments to study laser tuning and dynamics of the incubation effect. The SiMRR samples will be described in the next chapter.

The samples were irradiated under ambient conditions with varying laser fluences and numbers of pulses. The morphology of the irradiated surfaces, as well as the size and depth of craters, were analyzed using optical microscopy, Scanning Electron Microscopy, and atomic force microscopy. MicroRaman spectroscopy is used to analyze the phase of material within the irradiated zone. Errors and uncertainties are determined and presented as error bars in plots. They are associated with crater size measurement from SEM images, power measurement from the photodetector, and pulse-to-pulse energy fluctuation from the laser system.

Chapter 3

Silicon Microring Resonator and Post Fabrication Tuning Using Femtosecond Laser Pulses

3.1 Silicon Microring resonator and phase response

General silicon microring resonator (SiMRR) devices possess a continuous loop of waveguide with a circular shape or a racetrack, which in turn requires a high-contrast waveguide with strong confinement. All the devices used in experiments in this thesis were add-drop structures with racetrack resonators. In a SiMRR device, light trapped inside the microring travels around and returns to its starting point with a phase shift. A bus waveguide is placed close to the microring structure for coupling in and out of the resonator. Once the field of the light constructively interferes with itself after every round trip, the resonant condition of the microring cavity satisfies the condition:

$$\lambda_{\mathrm{m}} = \frac{2\pi \mathrm{R} n_{\mathrm{eff}}}{\mathrm{m}} \tag{3.1}$$

where m is the integer mode inside the resonator. When applied as filters and modulators, the microring resonators must have a resonance that occurs at a specifically designed wavelength.

The phase response of the SiMRR on the chip is achieved by sending probe light

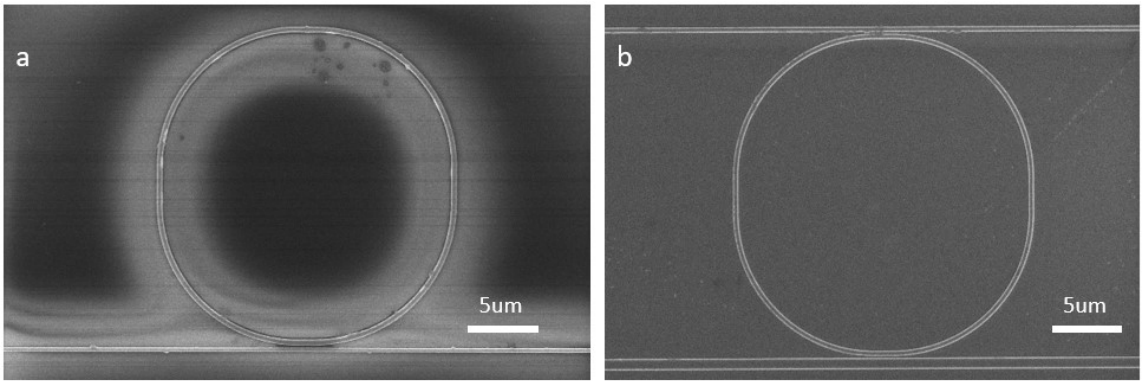

Figure 3.1: SEM image of the examples for typical ring resonators. (a) all-pass ring resonator.(b) add-drop ring resonator.

for measurement. The measurement light is coupled in and out of the long waveguide with a lensed fiber on both ends. Constructive interference occurs when the loop's waves reach an integer multiple of 2π in a round-trip phase shift, causing resonance in the cavity. Typically, the transmission spectrum of the bus waveguide with a single SiMRR shows resonance dips, each a free spectral range apart.

Common ring resonators can be separated into two forms depending on their structures: all-pass ring resonators and add-drop ring resonators. The simplest form of an all-pass ring resonator can be constructed with a single circular ring and a waveguide coupler by feeding one directional coupler output back into its input, as shown in Fig. 3.1. The transmission of intensity from the all-pass ring resonator can be described as

$$T_{\mathrm{n}} = \frac{I_{\mathrm{pass}}}{I_{\mathrm{input}}} = \frac{a^2 - 2ra\cos\phi + r^2}{1 - 2ar\cos\phi + (ra)^2} \tag{3.2}$$

Here, r is the self-coupling coefficient, a is the single-pass amplitude transmission relating to the power attenuation coefficient as $a^2 = \exp(-\alpha L)$, and ϕ is the single-pass phase shift relevant to the round trip length L and the propagation constant of the roundtrip circulation β, where $\phi = \beta L$.

For the add-drop microring resonator structure, the ring resonator is coupled to

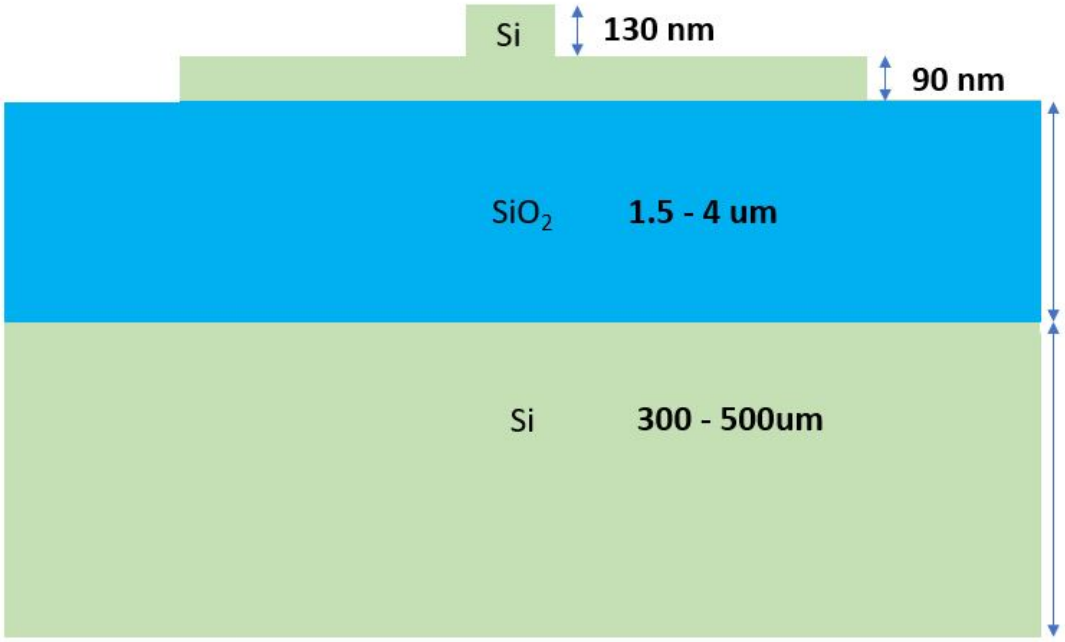

Figure 3.2: The Diagram of the crosssection view of the microring resonators used in our experiment.

two waveguides, in which the incident signal is also partially transmitted through the drop port, and the pass-transmission and drop-transmission can be shown as

$$T_p = \frac{I_{\text{pass}}}{I_{\text{input}}} = \frac{r_2^2 a^2 - 2r_1 r_2 a \cos\phi + r_1^2}{1 - 2r_1 r_2 a \cos\phi + (r_1 r_2 a)^2} \tag{3.3}$$

$$T_d = \frac{I_{\text{drop}}}{I_{\text{input}}} = \frac{(1 - r_1^2)(1 - r_2^2)\, a}{1 - 2r_1 r_2 a \cos\phi + (r_1 r_2 a)^2}. \tag{3.4}$$

r_1 and r_2 are the drop and pass-port coupling coefficients. When $r_2 a = r_1$, critical coupling occurs in a lossy resonator where no light passes through the waveguide.

3.1.1 Spectral characteristics and key parameters

The full width at half max (FWHM) bandwidth, or linewidth of the resonance for an add-drop microring resonator configuration, can be derived from equations 3.1

- 3.4 as

$$\mathrm{FWHM} = \frac{(1 - r_1 r_2 a)\,\lambda_{\mathrm{res}}^2}{\pi n_g L \sqrt{r_1 r_2 a}}. \tag{3.5}$$

The FSR of the resonator can be represented as [46]:

$$\mathrm{FSR} = \frac{\lambda^2}{n_g L} \tag{3.6}$$

which is defined as the wavelength change required to obtain a round-trip phase change of the wavelength range between two resonances. The group index of refraction of resonator n_g takes into account the dispersion in the waveguide and is related to the effective refractive index as:

$$n_g = n_{\mathrm{eff}} - \lambda_0 \frac{dn_{\mathrm{eff}}}{d\lambda} \tag{3.7}$$

The finesse, quality factor and roundtrip loss can characterize the quality of the microring resonator. The FSR and resonance width ratio define the finesse, indicating how narrow the resonances are in relation to their frequency distance. Commonly, a high finesse means sharp resonances.

The quality factor (Q-factor) is a measurement of the sharpness of the resonance wavelength profile relative to its central frequency, where

$$\text{Q-factor } = \frac{\lambda_{\mathrm{res}}}{\mathrm{FWHM}}. \tag{3.8}$$

The Q-factor is related to the number of round-trips made by the energy in the resonator before being lost to internal loss and the bus waveguide[46]. The round-trip loss can be derived from the transmission at the port using the field coupling approach [46]

$$\frac{\mathrm{S}_{\mathrm{thru,AP}}}{\mathrm{S}_{\mathrm{in,AP}}} = \frac{\tau - a_{\mathrm{rt}} e^{-j\phi_{\mathrm{rt}}}}{1 - a_{\mathrm{rt}} \tau e^{-j\phi_{\mathrm{rt}}}} \tag{3.9}$$

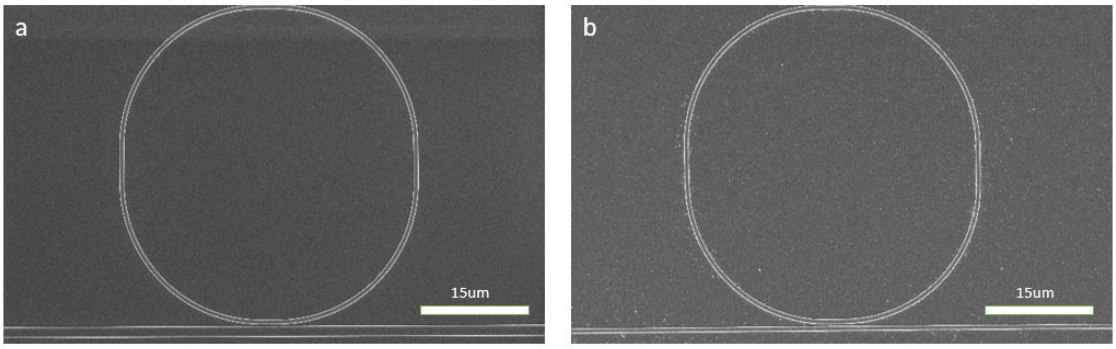

Figure 3.3: SEM images of the Silicon Microring resonators.(a) Commercially fabricated by Applied Nanotools(b) Self-Fabricated using Raith TWO EBL system in Nanofab at the University of Alberta

τ is the field transmission coefficient, $\phi_{\mathrm{rt}} = \mathrm{n_{eff}}(2\pi/\lambda)2\pi\mathrm{R}$ is the roundtrip phase of waveguide where λ is the free space wavelength of the light. The roundtrip field attenuation factor a_{rt} can be achieved from the curve fitting of the measured resonance wavelength profile.

3.2 Fabrication of SiMRR Samples

The SiMRR devices used in this thesis were designed by our group and fabricated either commercially by the Applied Nanotools or by ourselves in the nanofab at the University of Alberta. As shown in Fig.3.3, each microring had a radius of 15 µm and was coupled to a waveguide of 500 nm in width with a gap of 260 nm. It is a rib waveguide with a rib height of 130 nm and a slab height of 90 nm fabricated on the Silicon-on-insulator (SOI) platform. Fig.3.2 shows the diagram of crosssection view of the microring resonator, and the fundamental TE-mode inside the rib waveguide is similar to the ones in [47]. To maintain the consistency of the experiment, all the samples we used in Chapters 5 and 6 in this thesis are commercially manufactured by Applied Nanotools, which provided better shape uniformity and Q-factor.

A detailed fabrication flow of the SiMRR is shown in Fig.3.4. The fabrication process initiates with Commercial Silicon on insulator (SOI) pieces with 220 nm

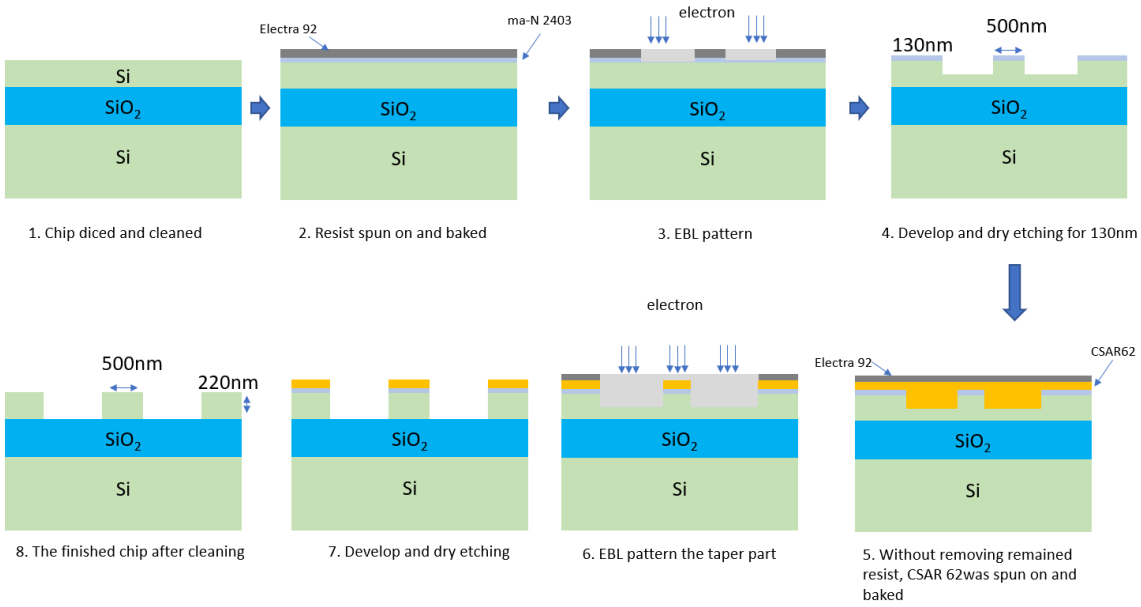

Figure 3.4: The simplified fabrication process flow of microring microring resonators using Raith TWO-EBL system. The first 4 steps are used for fabricating the microring resonator structures, and the following procedures are for fabricating edge couplers.

crystalline silicon layer on top of 1um thick SiO_2, and a 500 µm silicon structural box was employed in the fabrication process as a starting point. Each piece is diced into the silicon substrate from the backside for 300 µm, making it possible to break into 3mm x 2mm pieces after fabrication. Then, the individual chips are cleaned in piranha solution (A mixture of H_2SO_4 and H_2O_2 in a 3:1 scale) to avoid organic contamination, and the surface thin oxidation layer is removed with BOE solution for 60 seconds. The chips must also submerge in Surpass 3000 adhesion promotors for 60 seconds, which can help provide better resistance adhesion. After each solution process, the samples are rinsed with DI water and dried with an N_2 gun.

Patterning of the chips is then carried out on electron-beam-lithography (Raith - 150 TWO EBL Model). The patterning will be separated into two rounds of exposure, where the first round will create waveguide and resonators at 130 nm height, and the second round will open a window on each of the taper sides and etch the coupling taper to 220 nm height. During the fabrication of the waveguide structure, positive EBL resist ma-N 2403 is spun on the chips and baked for 60 s at $90°C$ using Brewer

Spinner and Hotplate. Electra 92 is also spun on and baked on the surface to increase the conductivity of the surface and reduce electron scattering. To expose the resist, the Raith 150-TWO system is operated at an accelerating voltage of 30 kV and 15 um aperture, providing a beam current of about 76 pA. The input and output waveguide is patterned in the fixed beam-moving stage (FBMS) option at a dose of $740pC/cm^2$ and a width of 500 nm.

The microring devices and tapers are patterned using the area write option at a dose of $300uC/cm^2$ and a step size of 0.02 µm. Each microring and input/output waveguide pattern takes around 10 min to write. After the exposure, the chip was developed in MF319 for 60 s and transferred in DI water for 60 s as a stopper. After inspection from an optical microscope, dry etching was used to transfer the pattern to the substrate with smooth and vertical sidewalls. The chip was etched for 130 nm in the Oxford Estrelas ICPRIE tool uses the recipe UNSWITCHED PROCESS for 95 s, which combines SF6 and C4F8 to provide vertical sidewalls while etching the silicon waveguides.

Right after the etching, without removing the remaining ma-N 2403, the chip is coated with a positive tone resist CSAR62, spun/baked, and coated with Electra 92 again. The exposure on EBL is operated at an accelerating voltage of 30 kV and 30 um aperture, with a beam current of about 340 pA. A patterned area of 20 um x 400 um is exposed with a dose of $400uC/cm^2$. After the exposure, the chip was developed in ZED-N50 for the 20 s and transferred to IPA for the 60 s. Dry etching on Oxford, Estrelas ICPRIE tool, uses the recipe UNSWITCHED PROCESS for 17.2 s. Lift-off solvent (Remover PG) and piranha solution are used to efficiently and completely remove the remaining resist films.

3.3 Post-fabrication of frequency tuning silicon devices

For the application of on-chip silicon devices, especially SiMRRs, a very specific operation wavelength is critically required so that the appropriate signal can be added or removed from the main waveguide path. The high index refraction and high optical mode confinement make silicon devices super sensitive to any deviation of dimension and geometry. For example, a variation of 1 nm width in a SiMRR waveguide can shift the operating resonance wavelength by 2 nm or more[48, 49]. Although the manufacturing technique of silicon photonics has been improved over the last decades, small errors in dimension from the designed waveguide values are still unavoidable, and the sub-nanometer resolution precision fabrication is still very costly and has low throughput. Post-fabrication methods are required to address the fabrication deviation issue.

Thermal tuning is the most widely used solution by temporarily modifying the refractive index and the spectral response according to the thermo-optic response of the silicon. This is usually achieved by applying micro-heaters placed on top or side of the devices as heat sources, providing a relatively linear resonant wavelength shift as a function of applied temperature. The drawback of such a method lies in the change being not permanent, and power must be continuously supplied to the device to maintain the index change. Although the method has shown its effectiveness and has been used in research areas or some industry applications, the large amount of additional power required by the microheaters, the additional fabrication steps, and the increased production and packaging cost strongly restrict its commercial usefulness.

Aside from actively tuning using microheaters, permanent change of resonant wavelength can be obtained by methods of permanent post-fabrication correction, namely trimming or permanently tuning devices to ensure their performance. The

advantage of trimming is that it can be done at the end of the fabrication process, and subsequently, the devices can be modified to obtain the required behaviour.

Trimming of devices requires a permanent change in the effective refractive index through changes in material properties, mainly the refractive index of the core(for passive devices) or the cladding material(active devices with oxidation cladding). Three main existing approaches have been investigated for SiPICs, including refractive index trimming of ultra-violet or visible light sensitive claddings [50–54], electron beam compaction and strain of silicon dioxide cladding[51, 55] or surface oxidation of silicon waveguide using an AFM tip[56, 57]. However, there are disadvantages to these methods, including the requirement of special materials for the cladding, which may not be compatible with the CMOS fabrication technology[51, 52], delicate setups involving either an electron microscope with vacuum chamber[55] or direct physical contact of AFM tapper with waveguide, which may cause additional damage to the structures[56, 57]. In general, these techniques are difficult to have high throughput.

A method for permanent tuning silicon photonic devices based on ultrafast laser-induced crystalline modifications and ablation has been demonstrated [5, 58]. From previous work in our group, we found that the resonance wavelengths of SiMRRs can be tuned with single femtosecond pulses of a Ti: Sapphire laser system at a wavelength of 800 nm(fundamental frequency)[5, 58] and 400 nm(second harmonic frequency)[2]. The operation wavelength of a silicon photonic device, such as a ring resonator, can be permanently changed by irradiating its silicon waveguide with a single femtosecond laser pulse. If the laser fluence is above the crystalline modification threshold, the wavelength can be increased, while if it is above the ablation threshold, the wavelength can be decreased. This contactless and robust method is relatively simple, requiring only an optical stage and a femtosecond laser, which is also relatively inexpensive and CMOS-compatible. Moreover, it is much faster than existing methods and can be performed on a production line. If many devices on the same chip need tuning, the only limiting factor would be the alignment stage's quickness and the laser's

repetition rate, allowing for tuning of many devices per minute or even second. This is significantly faster than all other permanent tuning techniques demonstrated.

The positive shifts in resonance wavelength are proportional to the increasing laser fluence[2]. When the laser fluences are increased to values beyond the ablation threshold of silicon, negative shifts result [2]. The physical mechanism responsible for the positive resonance wavelength shift is the change of refractive index of a thin layer of silicon as a result of modifications to the crystalline structures(e.g. amorphization) [5, 58]. The laser-irradiated layer would have a slightly larger refractive index than the crystalline silicon, slightly increasing the waveguide's overall refractive index. The physical mechanism responsible for the negative resonance wavelength shift is the removal of a thin layer of silicon due to ablation. For laser tuning using single near-infrared femtosecond laser pulses with fluences above the single shot ablation threshold, the surface and subsurface damages led to significant roundtrip microring losses[5].

In our previous work, we found that by applying many fs laser pulses with fluences significantly below the single shot ablation threshold on the same spot on the surface of a material. Such a more "gentle" laser irradiation approach, which we called "nanomilling," was applied to ablate copper foil, resulting in a depth resolution of about a nanometer[1]. This motivates the investigation of the multi-shot tuning approach in this thesis.

3.4 Experimental setups

3.4.1 SiMRR characterization setup

A typical laser irradiation setup is already described in Chapter 2. Two different SiMRR characterization setups are used in this thesis. The first setup[59] uses a tunable fibre laser as the light source and a power meter as the light detector. The tunable laser sweeps through the wavelength range of 1545-1565 nm, and the power

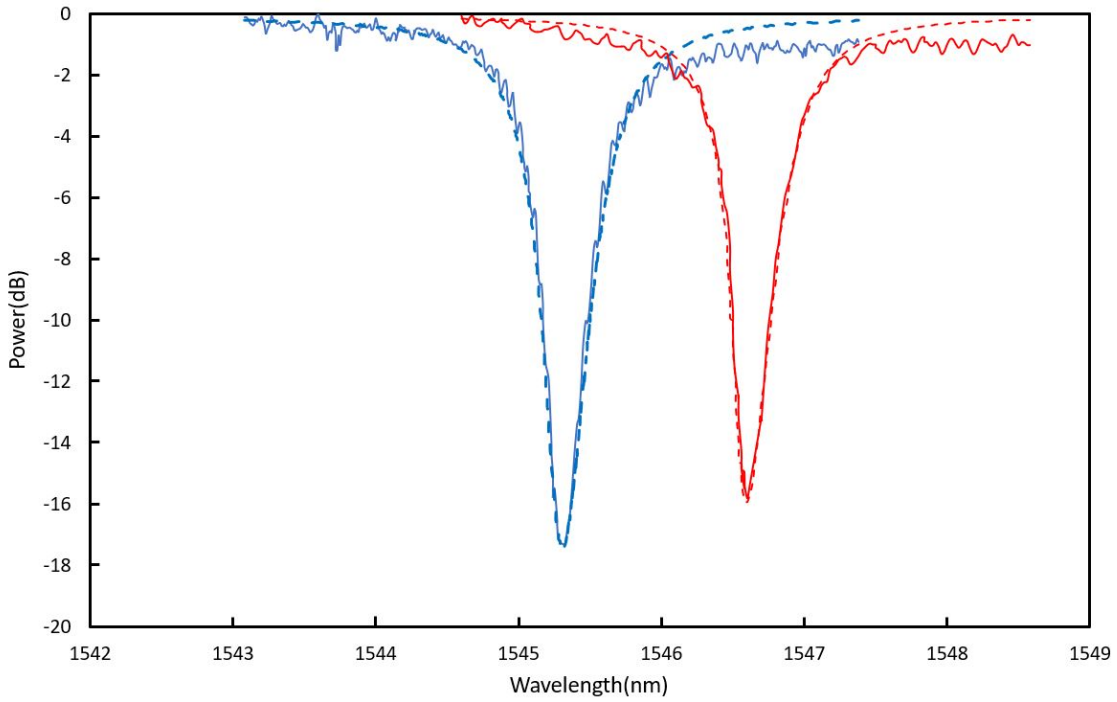

Figure 3.5: An Example of the curved fitting of resonance wavelength extracted from Chapter 5. The measured original resonance wavelength (solid blue) and measured data(solid red) of the microring resonator after laser irradiation with a laser fluence of $0.055 J/cm^2$ for N = 10 pulses. The corresponding curve fittings of the measured data are shown in dashed lines, respectively.

meter measures the output signals from the SiMRR. The details of the first setup are described in Chapter 5 (Fig 4). The second setup uses a superluminescent light emitting diode (SLED) to provide the broadband light, and the resonance wavelength spectrum is measured by an optical spectrum analyzer (OSA). The details of the second setup are described in Chapter 6. Typically, the acquisition time of a resonance wavelength spectrum from an SiMRR using the first "scanning" setup requires over 20 minutes, and an order of magnitude improvement in speed is achieved by using the "single-shot" second setup.

Chapter 4

Femtosecond laser multipulse ablation threshold and Incubation effect

4.1 Preface

Most of the materials in this chapter have been published in R. Zhang et al., "A study of incubation effects in femtosecond laser irradiation of silicon and copper", Applied Physics A, (2023) 129: 131, with the exception of section 4.4.3 and 4.5.

4.2 Introduction

Material processing using ultrashort laser pulses has been extensively studied for years due to its high precision and the small heat-affected zone generated during the laser energy deposition process. Ultra-high precision nanomilling of copper to depths of less than 10 nanometers was demonstrated using multiple femtosecond laser pulses with fluences below the single-shot ablation threshold by taking advantage of the incubation Effect [1]. The ablation threshold is a key parameter for laser micromachining or nanomilling techniques. The ablation threshold is usually defined as the minimum laser energy fluence that initiates the material removal process. A commonly used technique for determining the ablation thresholds for ultrafast laser irradiation is by plotting the squared crater diameter (D^2) as a function of fluence (F),

and the ablation threshold fluence is obtained by extrapolating the data to $D^2 = 0$ [33]. In this method, the measurement is normally performed with fluences higher than the ablation threshold, and the crater diameters can be determined using optical microscopy [7, 31, 60] or Scanning Electron Microscopy (SEM) [61, 62]. The method is commonly referred to as the "Gaussian beam limiting technique"[33].

It is well established that the multi-shot threshold reduces with the increase of pulse number N [35–37], and the effect is commonly referred to as "Incubation Effect". A number of models have been developed to describe the incubation effect. The most simple model assumes the N-shot ablation threshold fluences $F_{th}(N)$ is related to the single-shot ablation threshold fluence $F_{th}(1) = F_1$ by a power law [38], where

$$F_{th}(N) = F_1 N^{S-1} \tag{4.1}$$

This model assumes a free parameter S, called the "Incubation coefficient", is sufficient to describe the incubation effect for each material. The simple power-law model was found to provide a reasonable fit to experimental multi-shot ablation thresholds for many materials. The incubation coefficients were determined for a wide range of materials including metal [63], semiconductor [64], polymer [65] and others [22, 66].

One reasonable expectation is that there exists a critical laser fluence for material and below such fluence no ablation can occur even with an infinite number of shots. Such critical laser fluence can be named "sub-ablation threshold", F_∞. An effort to improve Eq.4.1 was done by adding the F_∞ term on the right side to Eq. 4.1 in an attempt to capture this effect [40]. However, many experimental data were found not to agree with the model very well [67, 68].

A more sophisticated model has been proposed by Zhanliang and Wolfgang et al. [39], which they called the "generic incubation model," taking into account F_∞ and the change of absorption. The model proposes that there is a decrease in critical

energy needed to damage the surface after each shot. It is assumed that the threshold fluence can be determined by the critical energy, G, deposited in a skin depth of $1/\alpha$ from the previous pulse, where

$$F_{th}(N) \approx \frac{G(N-1)}{\alpha(N-1)} \tag{4.2}$$

The fluence F, and pulse number N, dependent absorption coefficient, α, and critical energy, G, can be expressed as

$$\alpha(N,F) = \alpha_0 + \Delta\alpha\left(1 - e^{-\beta FN}\right) \tag{4.3}$$

and

$$G(N,F) = G_0 + \Delta G\left[1 - e^{-\gamma FN}\right] \tag{4.4}$$

Here, G_0, α_0, ΔG, and $\Delta\alpha$ represent the initial values for the critical energy, absorption and their corresponding maximum change, respectively. β and γ are two parameters, where β describes the efficiency of absorption coefficient change toward maximum value at a given fluence F, while γ is the coefficient for critical energy change. The final expression of threshold fluence can be given as

$$F_{th}(N,F) = \frac{F_1 - \left[F_1 - F_\infty\left(1 + \frac{\Delta\alpha}{\alpha_0}\right)\right]\left[1 - e^{-\gamma F(r)(N-1)}\right]}{1 + \frac{\Delta\alpha}{\alpha_0}\left[1 - e^{-\beta F(r)(N-1)}\right]} \tag{4.5}$$

Note F_{th} becomes F_∞ as N approaches infinity. The free material parameters $\Delta\alpha/\alpha_0$, β, and γ can be obtained by solving the nonlinear least-squares curve fitting problem using the experimental data. The model has been compared to the experimental data in literature ranging from metal to dielectric [34, 40–43].

In this paper, we have carried out experimental measurements of multiple-shot ablation thresholds for copper and silicon with irradiation fluences above and below the single-shot threshold i.e. $F > F_1$ and $F < F_1$. With a few exceptions, most incubation effect studies use $F > F_1$. It is important to investigate, especially for nanomilling applications, whether the results from studies using $F > F_1$ can be

applied to the $F < F_1$ cases. Our results are compared to the basic incubation effect models described by $Eq.4.1$ and the generic incubation model in $Eq.4.5$ to better understand the incubation effects of copper and silicon.

4.3 Experimental setup and Methods

4.3.1 Experimental Setup

A commercial Ti: sapphire laser system (Coherent Legend) was employed as the laser source, generating a laser beam with a repetition rate of 1 kHz and pulse duration of ∼130 fs at 800 nm wavelength. The experimental setup is shown in Fig. 4.1. Irradiation targets were mounted on a 3D motion stage with a step resolution of 200 nm. The laser beam focused using a 10x long working distance microscope objective, giving a $1/e^2$ spot size of approximately 2.9um and irradiated on the samples at 0° angle of incidence. Fig. 4.2 shows an example of the airy beam applied in the experiment and intensity distribution as well as its fitting to a gaussian profile. A CCD camera and an achromatic lens with 100cm focal length were employed to view the sample surface. The pulse energy was controlled by a combination of a half-wave plate and a glan-polarizer near the output of the laser source. The turning angle for the half-wave plate is limited to less than 30° to avoid pre-shot leakage. Fine energy control is achieved with an ND filter ranging from OD 0.5 to OD 3. The pulse number of multi-shot irradiation is achieved by combining a fast electric shutter and a delay generator to generate the required shots without shifting the beam profile. Two of the cross-calibrated silicon photodiode, PD 1 and PD 2, are placed before and after the electric shutter to track energy deposited on the sample's surface.

Samples of n-doped silicon wafers and poly-crystalline copper thin films are used as samples. A commercial n-doped silicon sample from University Wafer was diced into $10mm \times 10mm$ dimension pieces. The poly-crystalline copper thin films were $2um$ thick on a silicon substrate fabricated in the University of Alberta NanoFab

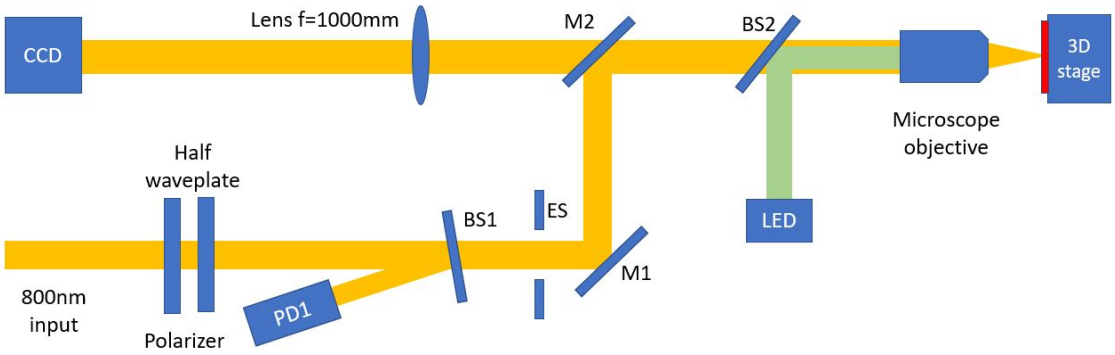

Figure 4.1: Experimental setup of irradiation system. M1 to M8 are high-reflection dielectric mirrors at 800 nm, A1 and A2 are alignment apertures, and ES is the electric shutter for pulse number controlling. The combination of a glan-polarizer and the half-wave plate is mounted near the beam entrance for energy tuning. A 10x microscope with a long working distance focuses the beam onto the sample for irradiation, and the LED at 532 nm wavelength is the light source for illuminating the sample surface for visualization. Two of the silicon photodiodes are placed before and after the electric shutter for cross-calibration of peak energy deposited on the surface of the sample.

Center using the Plasma Sputtering method. The samples were irradiated under air conditions with varying laser fluences and numbers of pulses. The morphology of the irradiated surfaces, as well as the size and depth of craters, were analyzed using optical microscopy, scanning electron microscopy, and atomic force microscopy. Errors and uncertainties are counted and presented as error bars correspond to 1std (approximately 68 percent of data points fall within one standard deviation of the mean average) in plots, and they are associated with the measurement of crater size from SEM images and power measurement from the photodetector, as well as the pulse-to-pulse energy fluctuation from the laser system.

4.3.2 Methods

Ablation thresholds were determined by studying the craters generated by laser pulses with fluences above the single-shot ablation threshold. The multi-shot ablation thresholds, $F_{th}(N)$, were determined using the Gaussian limiting technique. The $F_{th}(N)$ is related to the crater diameters, D, through the expression below:

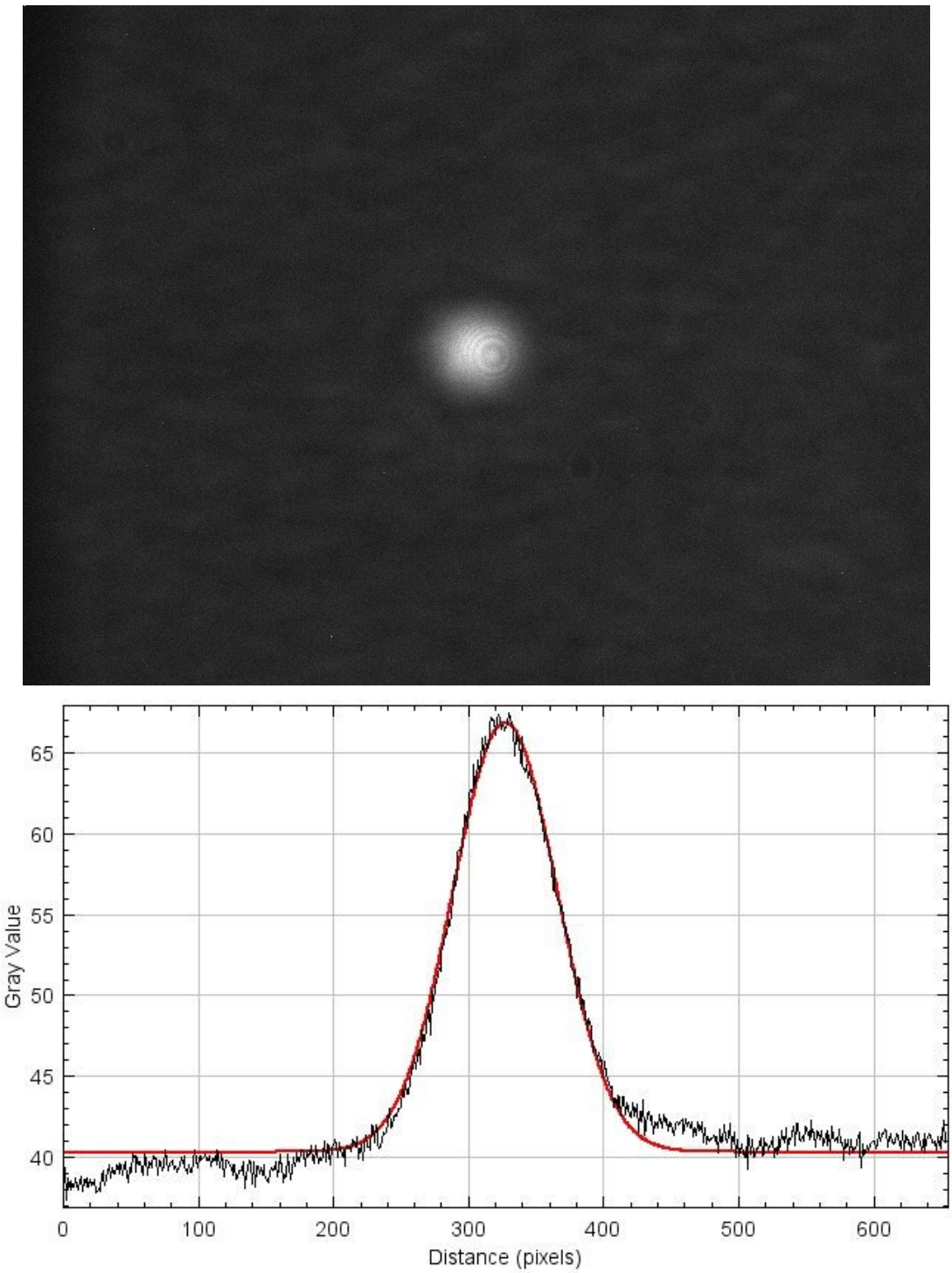

Figure 4.2: Example of the Beam profile applied in the experiment. (a) The greyscale image of the Airy beam profile obtained from a CCD camera. (b) Corresponded intensity distribution profile of the Gaussian beam. The black line is the really intensity profile and the red one is the gaussian fitting curve.

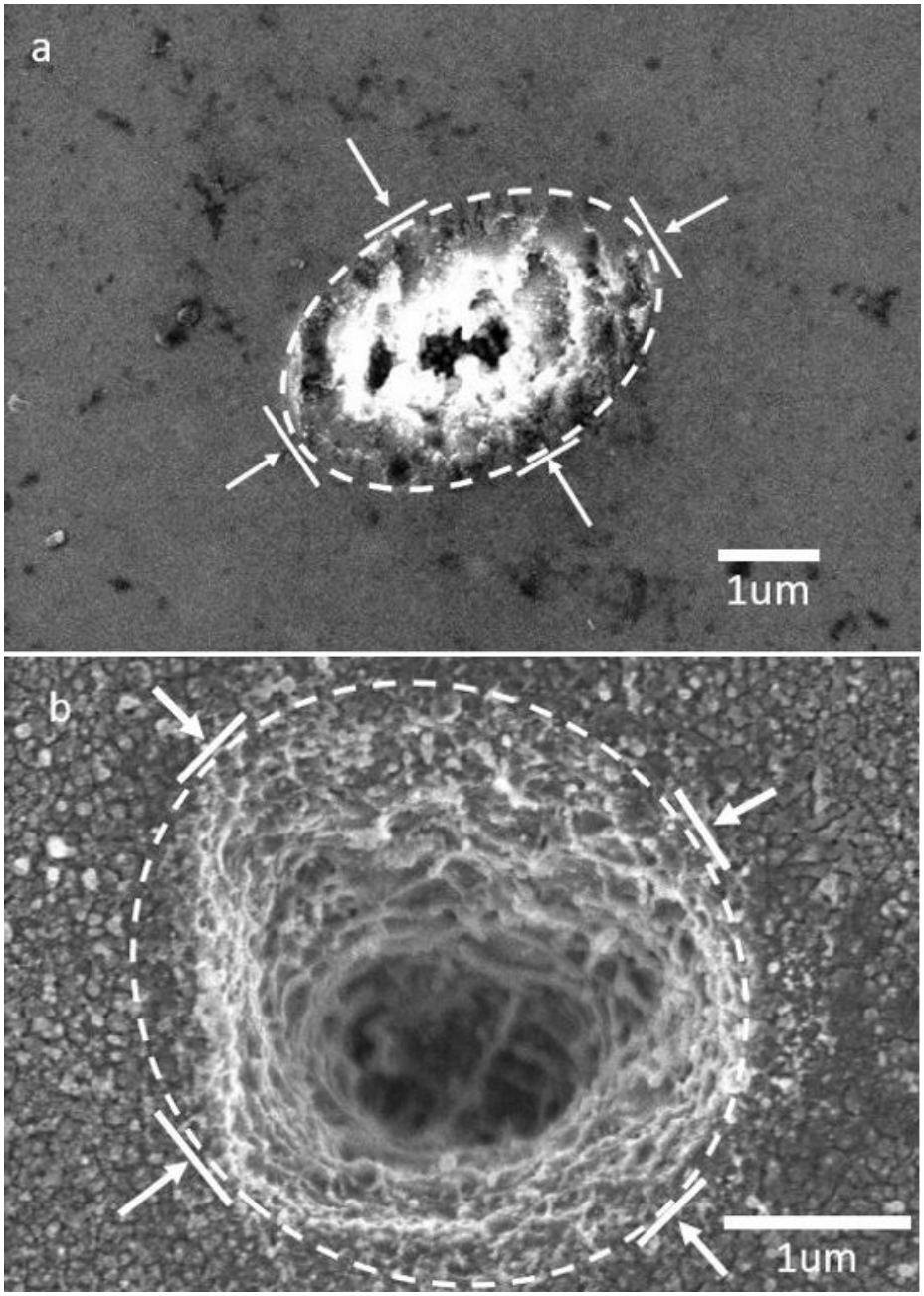

Figure 4.3: SEM images of craters generated by using laser fluences above the single-shot ablation thresholds. (a) Crater on silicon irradiated with $F = 0.52 J/cm^2$ at $N = 50$. (b) Crater on copper irradiated with $F = 1.03 J/cm^2$ at $N = 500$. The craters have elliptical shape. The diameters of the major axis and minor axis are indicated by the white arrows in the images.

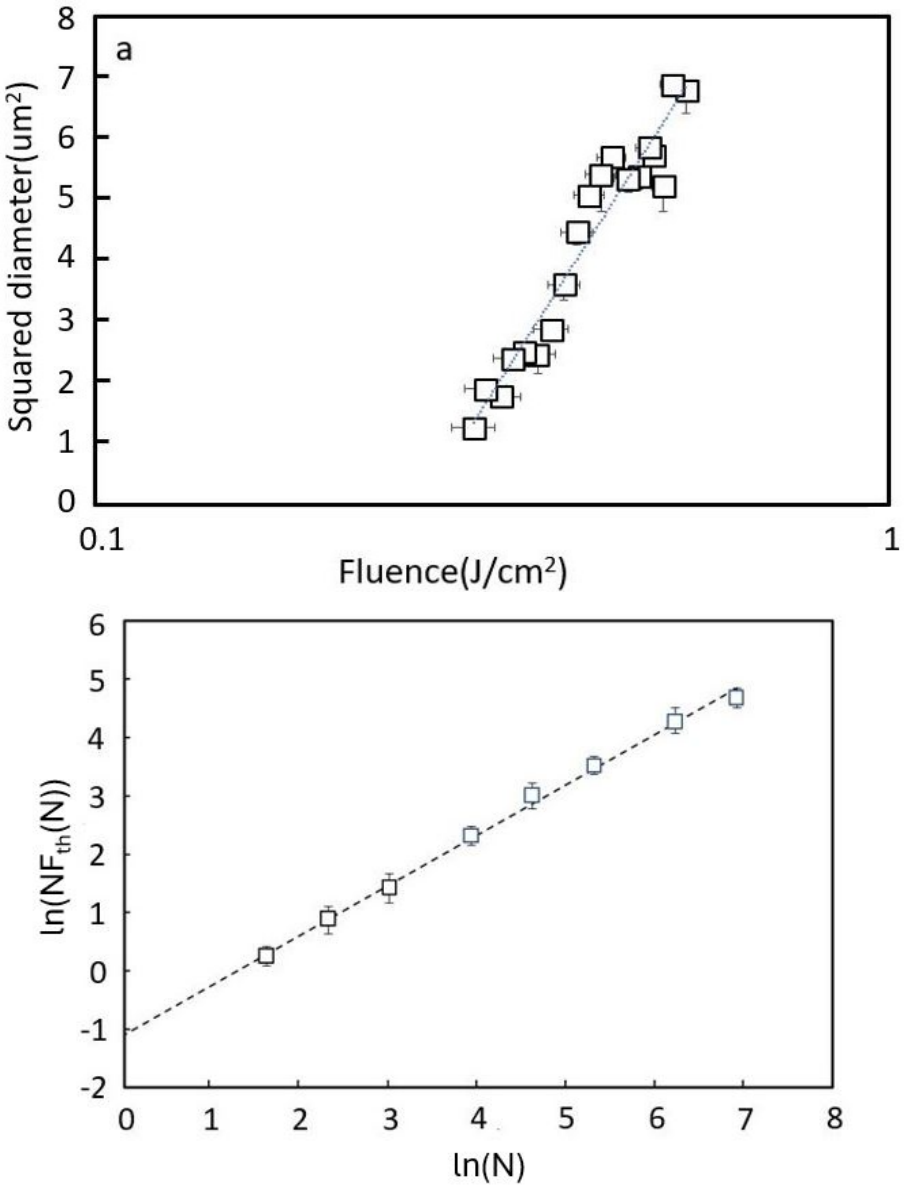

Figure 4.4: (a) Semi-log plot of squared crater diameters, D^2, as a function of laser fluence, F, for multi-shot ablation threshold for silicon with 5 shots, $F_{th}(N = 5)$. The line is the best fit of the data. (b) Plot for determining the incubation coefficient, S, and single shot ablation threshold, F_1, for silicon. The line is the best fit S and F_1 are obtained from the slope and y-intercept of the line.

$$D^2 = 2w^2 \ln\left(\frac{F}{F_{th}}\right) \tag{4.6}$$

Where w is the $1/e^2$ of the laser beam spot. Using silicon as an example, the craters were analyzed and measured using SEM and an optical microscope. As shown in Fig. 4.3, the craters have an elliptical shape. The diameters for the minor axis were used as values for D. A semi-log plot of D^2 versus F for Si with $N = 5$ is shown in Fig. 4.4a. The $F_{th}(N = 5)$ was determined from the plot by obtaining the best linear fit to the data. The uncertainties in determining the threshold fluence arise from uncertainties in spot size and energy measurements. Due to the incubation effect, the multi-shot ablation threshold $F_{th}(N)$ reduces with an increase of pulse number. The incubation coefficient can be obtained from the $Eq.4.1$, which can be re-written as:

$$\ln(NF_N) = S\ln(N) + \ln(F_1) \tag{4.7}$$

A plot of $ln(NF_{th}(N))$ versus $ln(N)$ for silicon and its best linear fit is shown in Fig. 4.4b as an example. The incubation coefficient S and the single-shot ablation threshold F_1 were obtained from the slope and the y-intercept respectively of the linear fit.

Multi-shot ablation thresholds and "no ablation" thresholds were determined from the irradiated spots created by using various numbers of laser pulses with fluences below the single-shot ablation threshold. An example of SEM images for a matrix of irradiated spots on a silicon wafer is shown in Fig. 4.5. The pulse number increased from left to right in row ranging from $N = 5, 10, 20, 50, 100, 200, 500$, and laser fluence gradually reduces from top to bottom from $0.282 J/cm^2$ to $0.275 J/cm^2$. A multi-shot ablation threshold was obtained using the following "bisection method" searching approach. Laser fluences are reduced in small steps while keeping the same number of shots N. When the fluence is reduced to a value, where the irradiated spot can no longer be seen (as shown in the dotted box in Fig. 3), the fluence and the previous

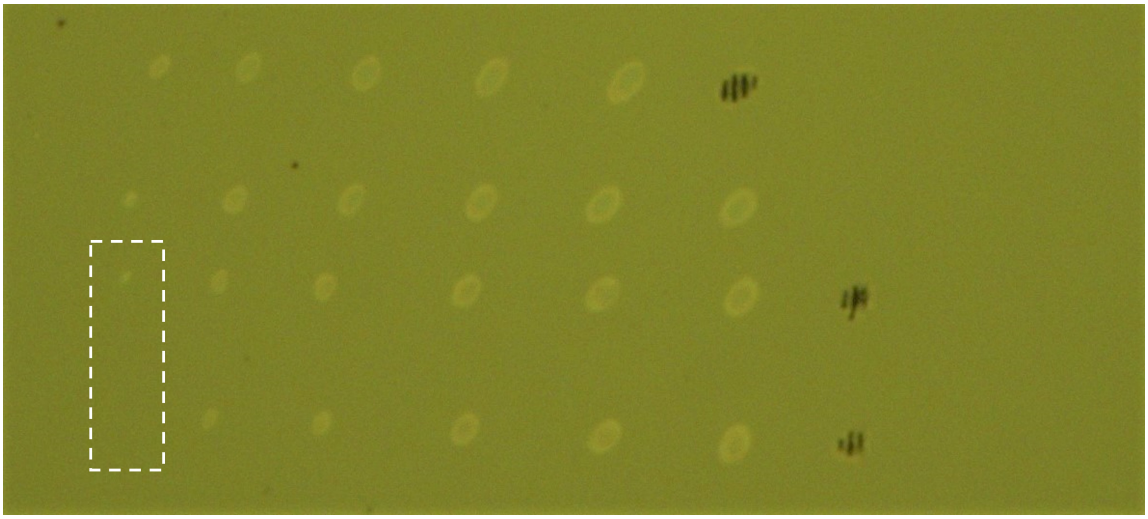

Figure 4.5: Optical image for a matrix of irradiated spots on a silicon wafer. Multiple laser pulses with fluences below the single-shot ablation threshold were used. The pulse number increased from left to right in rows ranging from $N = 5, 10, 20, 50, 100, 200, 500$, and laser fluence gradually reduced from top to bottom from $0.282 J/cm^2$ to $0.275 J/cm^2$.

higher one would define the first set of high and low values of the search. The fluence with a value in the middle of the high and low values would be used. If the irradiated spot can be seen, the fluence would become the high value of the second set, otherwise, it would become the low value. After several iterations, the $F_{th}(N)$ was considered to be the high value of the range from the last set of measurements in the bisection method.

4.4 Results and Discussion

4.4.1 Copper

The single-shot and multi-shot ablation thresholds for polycrystalline copper were determined for the "$F > F_1$" case using the method described in section 2.2. The single-shot ablation threshold, F_1, and incubation coefficient, S, were determined to be $0.87 J/cm^2$ and 0.78, respectively. Our F_1 is consistent with results from other studies which reported a range of $0.79 - 0.95 J/cm^2$ [31]. Our S value is also consistent with previous studies, which reported a range of 0.75-0.79 [31, 69]. The ablation

thresholds data (red diamonds), the fit based on the basic model (blue line) and the fit based on the generic model (red curve) are shown in Fig 4.8. The ablation thresholds fit the basic model (power law) and the generic incubation model well.

The multi-shot ablation thresholds for polycrystalline copper were investigated by applying laser pulses with fluences below the single-shot ablation threshold, i.e. $F < F_1$ case. The shots were carried out by gradually reducing the laser fluence. Fig. 4.6 shows the SEM image of the copper surface under irradiation with multiple pulses N = 20, 50, 100, 200, 500, and 1000 at a constant laser fluence of $0.571 \pm 0.015 J/cm^2$. With the first few shots ($N < 100$), only a melted-like area was observed at the center of the irradiated spot (Fig. 4.7). The melted-like area increased with the number of pulses. When N reached 200 and 500, it clearly shows different morphology for the outer side of the spot when compared to the inside region. An ablated crater was observed at the center of the zone, while the surrounding area looked like a melted ring. A crater was formed after 5000 pulses, even at $0.2 J/cm^2$. The $F_{th}(N)$ were determined using the method described in section 2.2, and they are plotted as blue squares in Fig. 4.8. Both $F_{th}(N)$ data generated using fluences above and below the single-shot ablation threshold are consistent with each other. The "sub-ablation" threshold, F_∞, was estimated to be $0.18 J/cm^2$. No damage spot was observed at $F = 0.18 J/cm^2$ even at $N = 1 \times 10^5$. Table. 4.8 provides a summary of the parameters for both incubation models for $F_{th}(N)$ data generated using fluences above and below the single-shot ablation threshold. Most of the values for both cases are consistent with each other.

As for sub-threshold irradiation, a significant crater was still spotted even at $0.2 J/cm^2$ corresponding to 22% at 5000 pulses, and the critical threshold fluence was estimated as lower than $0.18 J/cm^2 \pm 0.02 J/cm^2$ for sub-threshold irradiation, where no irradiation can be detected even with 1×10^5 pulses or more. A fitting of the generic incubation model with our sub-threshold fluence shown in Fig. 4.8 in the blue dashed line indicates that it matches well compared to the original above

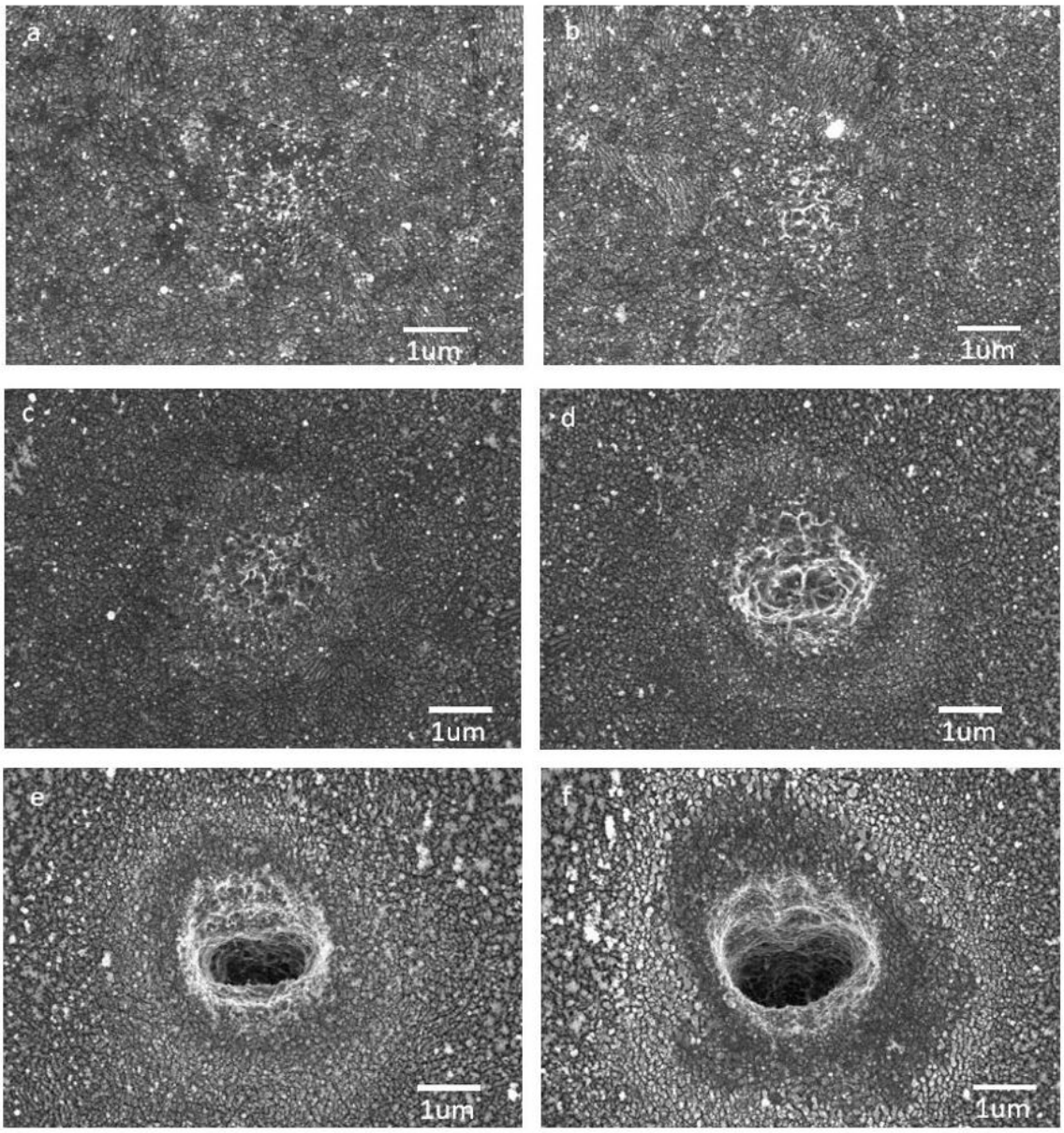

Figure 4.6: SEM image of irradiated copper surface with sub-threshold fluence of $0.571 J/cm^2$ ($F < F_1$) with different pulse numbers N., (a) $N = 20$, (b) $N = 50$, (c) $N = 100$, (d)$N = 200$, (e)$N = 500$, (f)$N = 1000$.

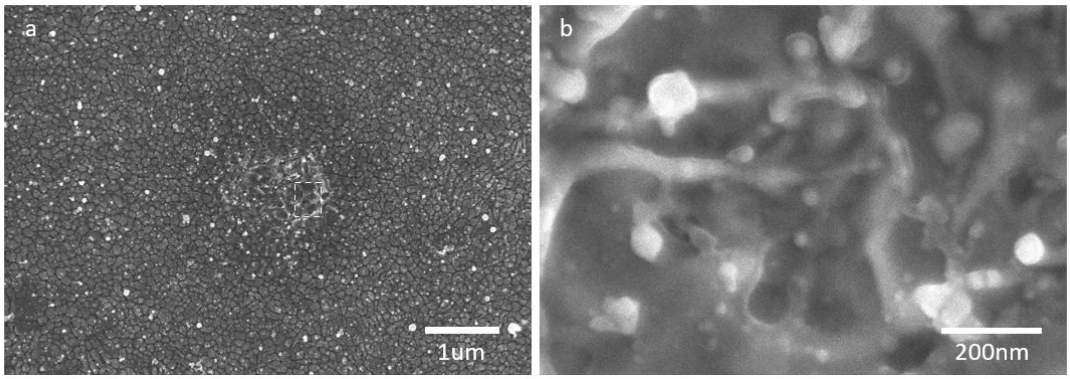

Figure 4.7: (a)SEM image of irradiated copper surface with fluence of $0.485 J/cm^2$ ($F < F_1$) with 50 pulses. (b)Enlarged image of the melting zone.

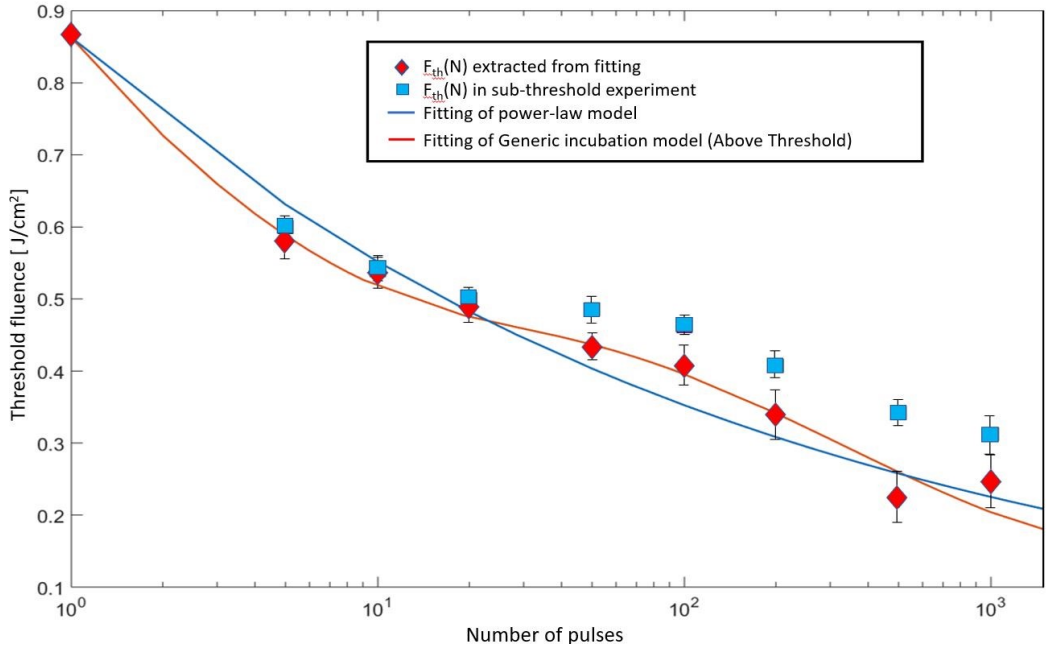

Figure 4.8: Ablation thresholds, $F_{th}(N)$, as a function of N for poly-crystalline copper thin film irradiated with fluences ($> F_1$) and ($< F_1$). Red diamonds are ablation thresholds ($F > F_1$ case), and blue squares are the measured ablation thresholds ($F < F_1$ case). The red curve represents the fitting of the generic incubation effect model with ablation threshold data generated from $F > F_1$. The blue line best fits the ablation threshold data generated from $F > F_1$ based on the simple incubation effect model (power law).

threshold ones. Table. 4.1 presents the parameters for both of the fittings, incubation coefficient, and F_∞. Most of the values match with each other within an error bar (γ is found larger by a factor of 2, which may be due to the small variation of deposition thickness [39]), indicating that the sub-threshold irradiation and incubation behaviour of copper can be properly fit with the generic incubation models. The non-ablation threshold fluence derived from the model is obtained at $0.169 J/cm^2$, while the F_∞ obtained from the binary approach in the sub-threshold regime was estimated at $0.18 J/cm^2 \pm 0.02 J/cm^2$, respectively.

Table 4.1: Summary table for copper including single-shot ablation threshold, F_1, "single-shot ablation" threshold, F_∞, and fitting parameters for the two incubation effect models: S is the incubation coefficient for the basic incubation effect model; $\Delta\alpha/\alpha_0$, β and γ are free material parameter for the generic incubation effect model

Fitting Data	S	F_1	F_∞	$\Delta\alpha/\alpha_0$	β	γ
$F > F_1$ case	0.78	$0.87 J/cm^2$		0.746	0.38365	0.00388
$F < F_1$ case	0.80		$0.18 J/cm^2$	0.773	0.40500	0.00839

4.4.2 Silicon

The single-shot and multi-shot ablation thresholds for single crystal silicon, for $F > F_1$ case, were determined using the method described in section 2.2. The single-shot ablation threshold, F_1, and incubation coefficient, S, were determined to be $0.34 J/cm^2$ and 0.84, respectively.

Our result of incubation coefficient and the single shot threshold was slightly higher than the value from Bonse et al. [7] where $S = 0.82$, $F_{th} = 0.28 J/cm^2$ at 130 fs, but matches well with a reported range of results from Nathala et al. [31]. The ablation thresholds data (red rhombus), the fit based on the basic model (blue line) and the fit based on the generic model (red curve) are shown in Fig. 4.9. The ablation thresholds are consistent with both the basic and generic incubation effect models.

The multi-shot ablation thresholds for single-crystal silicon were also investigated by applying laser pulses with fluences below the single-shot ablation threshold. The shots were carried out by gradually reducing the laser fluence. Fig. 4.10 shows SEM and optical microscopy images for an evolution of irradiated regime on silicon surface cat energy fluence of $0.27 J/cm^2$ with various pulse numbers, N. For $N = 20$, no significant change can be detected with SEM. A gradual increase in pulse number led to the formation of the dark, thin layer, as shown in the middle of the irradiated area, while the outer side of the region still presented a brighter field. The clear boundary of the irradiated zone was difficult to be identified for the first 50 - 200 pulses. At $N = 500$, a crater is generated with periodic structures at the middle part of the regime, which maybe formed due to the melting and recrystallizing processing. The corresponding optical image (inset of Fig. 4.9) of the irradiated area also presented a "bright spot" at a small pulse number and was found increasingly brighter flash during a shot as the number of shots increased until craters started to form and presented a "black spot" under optical microscope(shown in Fig. 4.11a). An enlarged image of the bright and dark interface for $N = 100$ case was shown in Fig. 4.11b, where no significant features were found within the area. EDS result shows that there is only a Si peak within the irradiated area, indicating that it is not due to oxidation. The spot in Fig. 4.11 was also scanned using Atomic force microscopy in taping mode to measure the height variation, and no significant change was observed within this area. We suspect the dark regime at the center of the irradiated area is a melted and re-solidified thin layer, while the outer bright region may be due to the formation of amorphous silicon, given that the outside region was exposed to lower fluence because of the Gaussian spatial profile. The $F_{th}(N)$ for the $F < F_1$ case were determined using the method described in section 2.2, and they are plotted as blue squares in Fig. 4.10. The $F_{th}(N)$ values for the $F < F_1$ case are significantly higher than those for the $F > F_1$ case. Thus, $F_{th}(N)$ values for silicon found using $F > F_1$ are not useful for femtosecond nanomilling studies [7, 70].

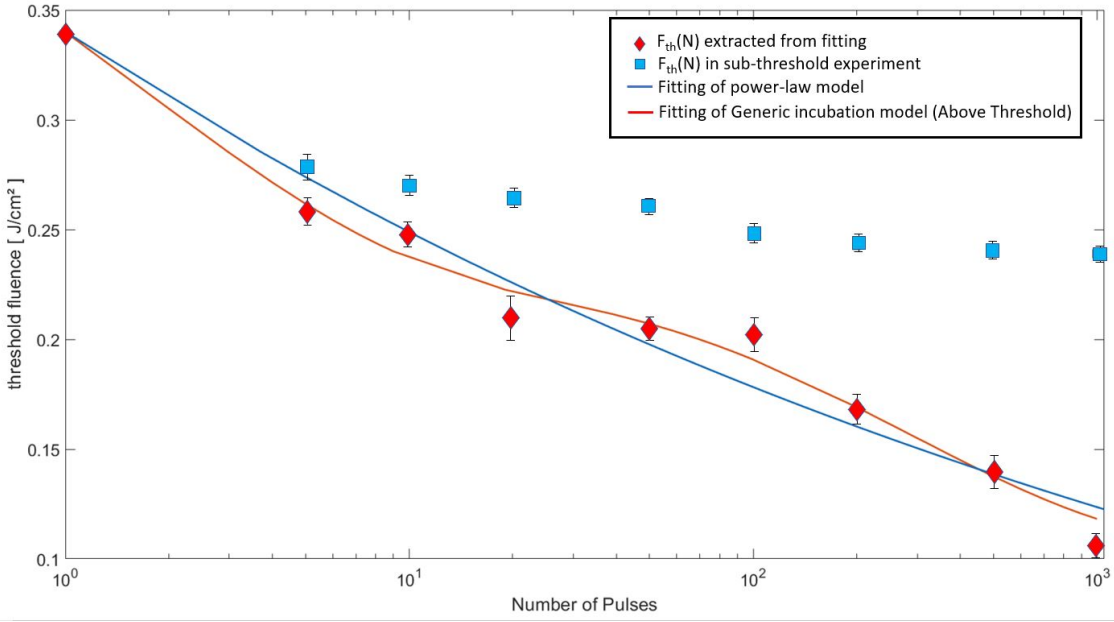

Figure 4.9: Ablation thresholds, $F_{th}(N)$, as a function of N for n-doped silicon wafer sample irradiated with fluences ($> F_1$) and ($< F_1$). Red rhombus represents extracted ablation thresholds ($> F_1$ case) from squared crater diameter to fluence, and blue squares are the ablation thresholds ($< F1$ case) obtained from fluences below the single-shot threshold. The red curve represents the fitting of the generic incubation effect model with ablation threshold data generated from $F > F_1$. The blue line is the best fit for the ablation threshold data generated from $F > F_1$ based on the simple incubation effect model (power law).

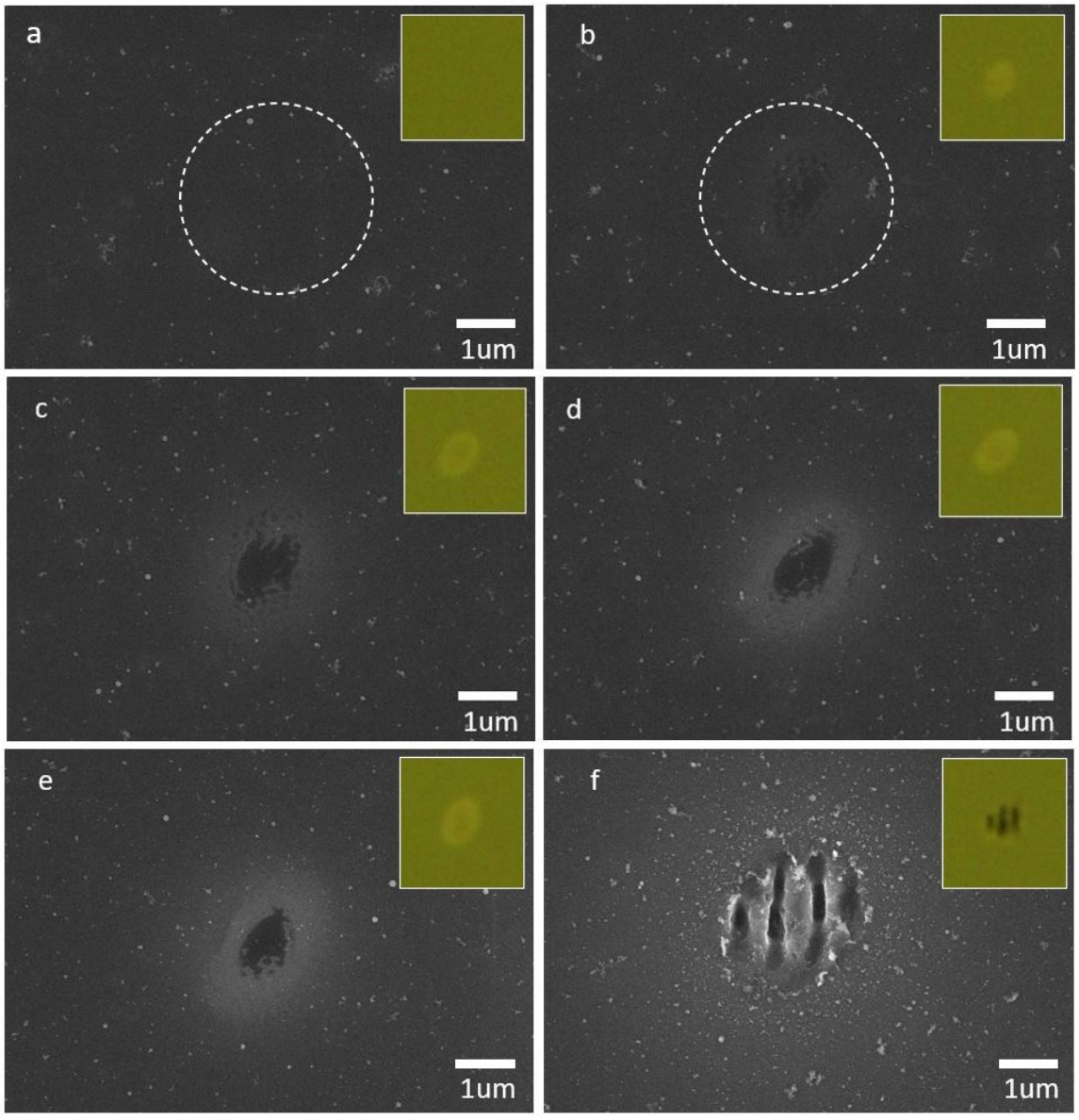

Figure 4.10: SEM image of irradiated silicon surface with fluence of $0.271 J/cm^2$ ($F < F_1$) with different pulse numbers.(a)$N = 5$, (b)$N = 20$, (c)$N = 50$, (d)$N = 100$, (e)$N = 200$, (f)$N = 500$. The dashed circles in (a) and (b) indicate the locations of the laser beam.

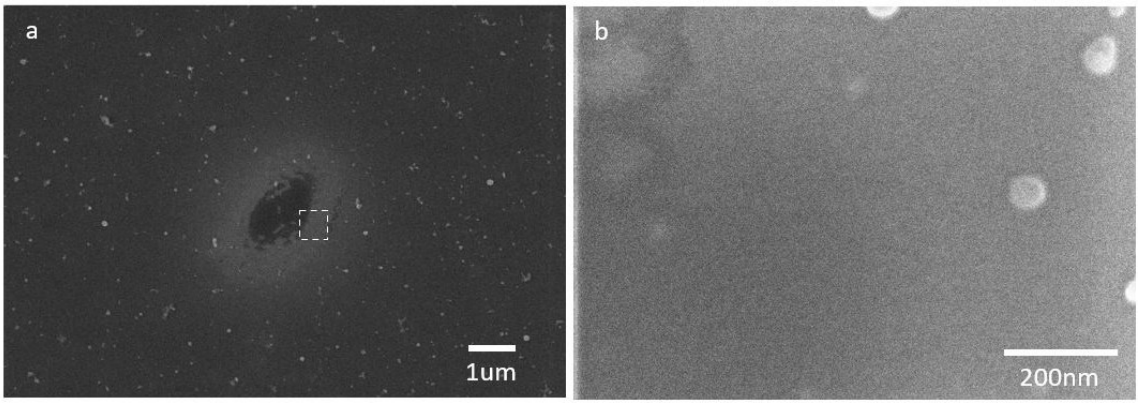

Figure 4.11: SEM images of irradiated silicon surface with fluence $F = 0.271 J/cm^2 (F < F_1)$ with $N = 100$. (a) The larger field of view. (b) Higher magnification image for the dark and gray region marked with a dashed box in (a).

The "sub-ablation" threshold, F_∞, was estimated to be $0.21 J/cm^2$. As can be seen from Fig. 4.9, the power law is not a good fit for the blue square data since they become flattened after a small number of shots. Table. 4.2 provides a summary of results for silicon found in this study. They include F_1, F_∞, and the parameters for both incubation models. These values can be useful for guiding femtosecond nanomilling of silicon studies. The parameters for the generic incubation effect models for the $F > F_1$ and $F < F_1$ cases have large differences, and it does adequately describe the data. The results point to the need for further improvements of incubation models by other effects, including multi-photon absorption and silicon defect physics.

Table 4.2: Summary table for silicon including single-shot ablation threshold, F_1, "single shot ablation" threshold, F_∞, and fitting parameters for the two incubation effect models: S is incubation coefficient for the basic incubation effect model; $\Delta\alpha/\alpha_0$, β and γ are free material parameter for the generic incubation effect model.

Fitting Data	S	F_1	F_∞	$\Delta\alpha/\alpha_0$	β	γ
$F > F_1$ case	0.84 ± 0.02	$0.34 J/cm^2$		0.479	0.86249	0.02029
$F < F_1$ case			$0.21 J/cm^2$	0.247	1.86146	0.04446

4.4.3 Silicon thin films

Investigations of the multi-shot threshold and incubation coefficient have also been carried out on silicon thin films. The beam size was cut down to $\sim 5mm$ using an aperture and a 10x long working distance microscope (Mitutoyo M plan Apo) to achieve a Gaussian $1/e^2$ beam radius of 13.4um on the sample surface. The sample surface is located 400 um in front of the focal plane of the lens. Both the fundamental wavelength, 800 nm, and the second harmonic wavelength, 400 nm, were used in the experiment. During the experiment, two different silicon thin film samples are employed here for comparison: a thin film with 250nm thickness deposited using the PECVD method on a bulk silicon piece and a commercial Silicon on Insulator(SOI) piece from the university wafer with the top silicon layer of 250nm.

800nm wavelength case

The single-shot and multi-shot ablation thresholds for PECVD thin film and SOI were determined by applying the "Gaussian beam limiting technique" method. The single-shot ablation threshold, F_1, and incubation coefficient, S, were determined to be $0.18J/cm^2$ and 0.84, respectively. As is shown in Fig. 4.12, for N = 10. the ablation threshold dropped to $0.102J/cm^2$, and for N = 100, the ablation threshold dropped to $0.08J/cm^2$. As is shown in Fig. 4.13, the multishot ablation threshold values for the commercial 250 nm Si thin film on SOI are consistent with those of the PECVD 250 nm Si thin film on Si. This indicates that the SiO_2 layer does not significantly affect ablation thresholds.

The ablation thresholds of the 250 nm Si thin films on bulk Si or on Si with a SiO_2 layer are significantly lower than those of bulk Si. The frequency tuning experiments reported in Chapter 5 also observe much lower ablation thresholds.

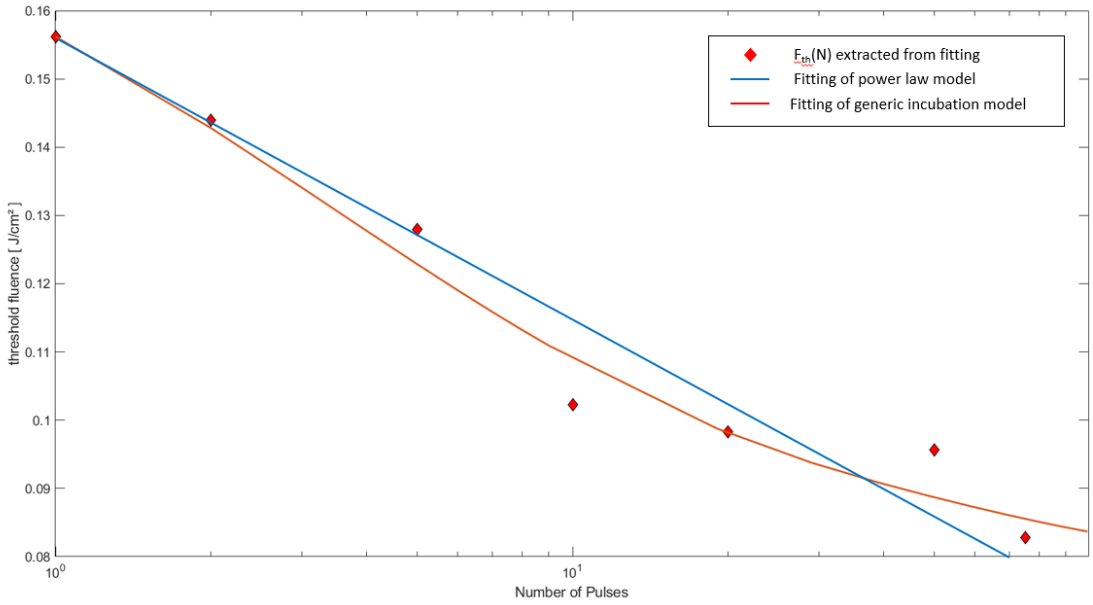

Figure 4.12: Ablation thresholds, $F_{th}(N)$, as a function of N for 250nm PECVD silicon thin film sample irradiated with fluences ($> F_1$). The red rhombus represents extracted ablation thresholds from squared crater diameter to fluence. The red curve represents the fitting of the generic incubation effect model with ablation threshold data, and the blue line is the best fit for the ablation threshold data based on the simple incubation effect model (power law).

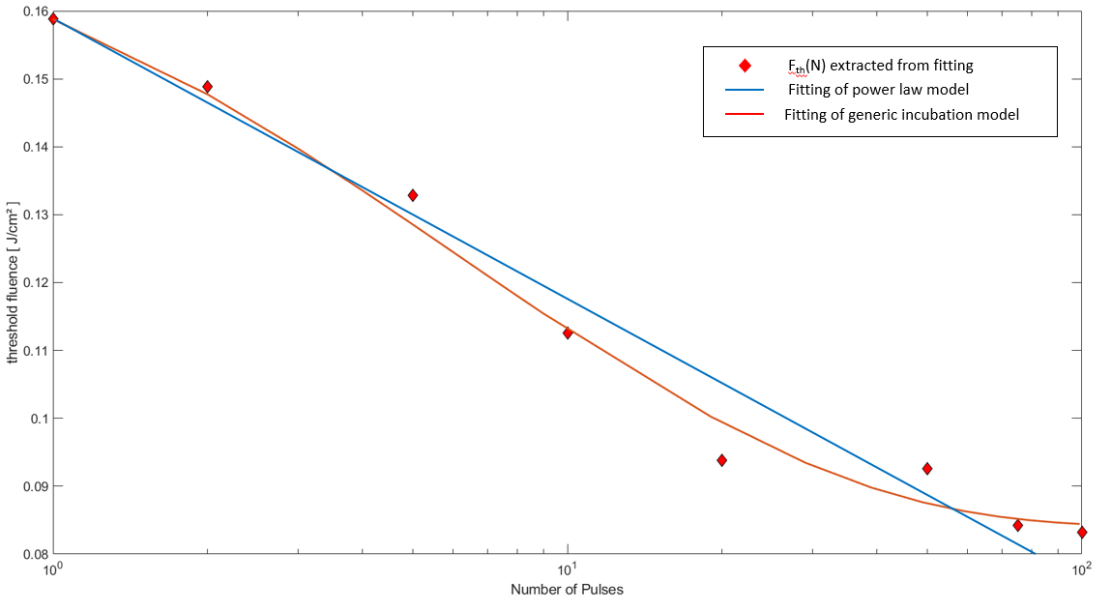

Figure 4.13: Ablation thresholds, $F_{th}(N)$, as a function of N for SOI sample irradiated with fluences ($> F_1$). Red rhombus represents extracted ablation thresholds from squared crater diameter to fluence. The red curve represents the fitting of the generic incubation effect model with the ablation threshold data, and the blue line is the best fit for the ablation threshold data based on the simple incubation effect model (power law).

Table 4.3: Summary table for SOI sample including single-shot ablation threshold, F_1, "single shot ablation" threshold, F_∞, and fitting parameters for the two incubation effect models: S is incubation coefficient for the basic incubation effect model(model 1); $\Delta\alpha/\alpha_0$, β and γ are free material parameter for the generic incubation effect model (model 2).

Fitting Data	S	F_1	F_∞	$\Delta\alpha/\alpha_0$	β	γ
F_{PECVD} case	0.83 ± 0.02	$0.1562 J/cm^2$	$0.0802 J/cm^2$	0.51929	1.27286	0.22782
F_{SOI} case	0.83 ± 0.02	$0.1588 J/cm^2$	$0.0832 J/cm^2$	0.86851	0.61081	0.07179

400nm wavelength case

Similar experiments have also been conducted on a 400nm wavelength laser beam ablated SOI thin film by applying the "Gaussian beam limiting technique" method. The single-shot ablation threshold and incubation coefficient, S, were determined to be $0.656 J/cm^2$ and 0.94, respectively. As is shown in Fig. 4.14, for N = 10, the ablation threshold dropped to $0.0628 J/cm^2$, and for N = 100, the ablation threshold dropped to $0.0593 J/cm^2$. At N = 2000, the threshold was achieved at $0.0528 J/cm^2$, which should be close to the critical threshold value.

Table 4.4: Summary table for 400nm irradiation on silicon including single-shot ablation threshold, F_1, "single shot ablation" threshold, F_∞, and fitting parameters for the two incubation effect models: S is incubation coefficient for the basic incubation effect model; $\Delta\alpha/\alpha_0$, β and γ are free material parameter for the generic incubation effect model.

Fitting Data	S	F_1	F_∞	$\Delta\alpha/\alpha_0$	β	γ
$F > F_1$ case	0.94 ± 0.02	$0.0656 J/cm^2$		0.077	1.41196	0.01289

Fig. 4.15 and Fig.4.16 shows OM and SEM images for an evolution of irradiated regime on silicon surface at energy fluence of $0.113 J/cm^2$ with various pulse numbers, N. For $N = 1$, a clear region of ablation at the center of the laser-irradiated area and the surrounding melting area with a brighter colour can be detected with OM and SEM. A gradual increase in pulse number led to significant enlargement of the ablated crater size and depth at the center of the laser irradiated area, while the

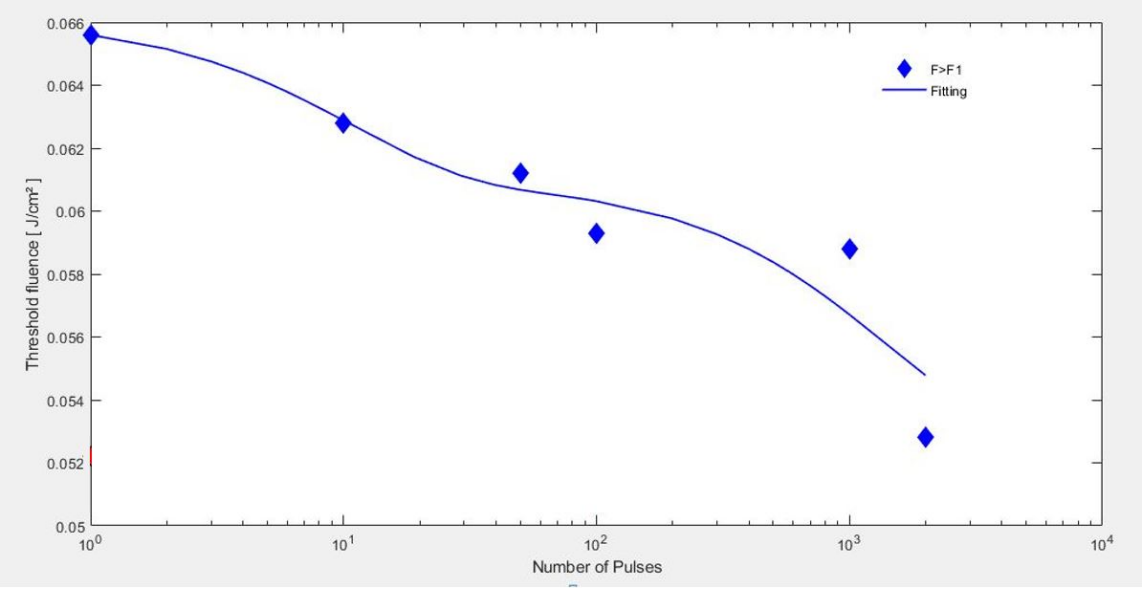

Figure 4.14: Ablation thresholds, $F_{th}(N)$, as a function of N for SOI sample by 400nm wavelength laser irradiation. Blue rhombus represents extracted ablation thresholds from squared crater diameter to fluence with fluences ($> F_1$). The red rhombus represents are extracted values of ablation threshold for different pulse numbers from SiMRR tuning experiments.

surrounding melting zone showed only a small increase in size. With the laser pulses, the ablation crater size gradually increases until it is similar to the size of the melting zone. At $N = 100$, the whole ablated area crater shows significant material removal, periodic structures and melting and recrystallizing features. The result indicated that for 400nm laser irradiation, the incubation effect is very weak since the surface modification area did not show significant enlargement with the increase of pulse numbers. Thus, the incubation effects for the 400 nm case are significantly different from that of the 800nm case. We believe this might be due to the different absorption for 400nm cases (linearly absorption) and 800nm cases(Two-photon absorption dominated); however, further investigation is needed for a better understanding of this phenomenon.

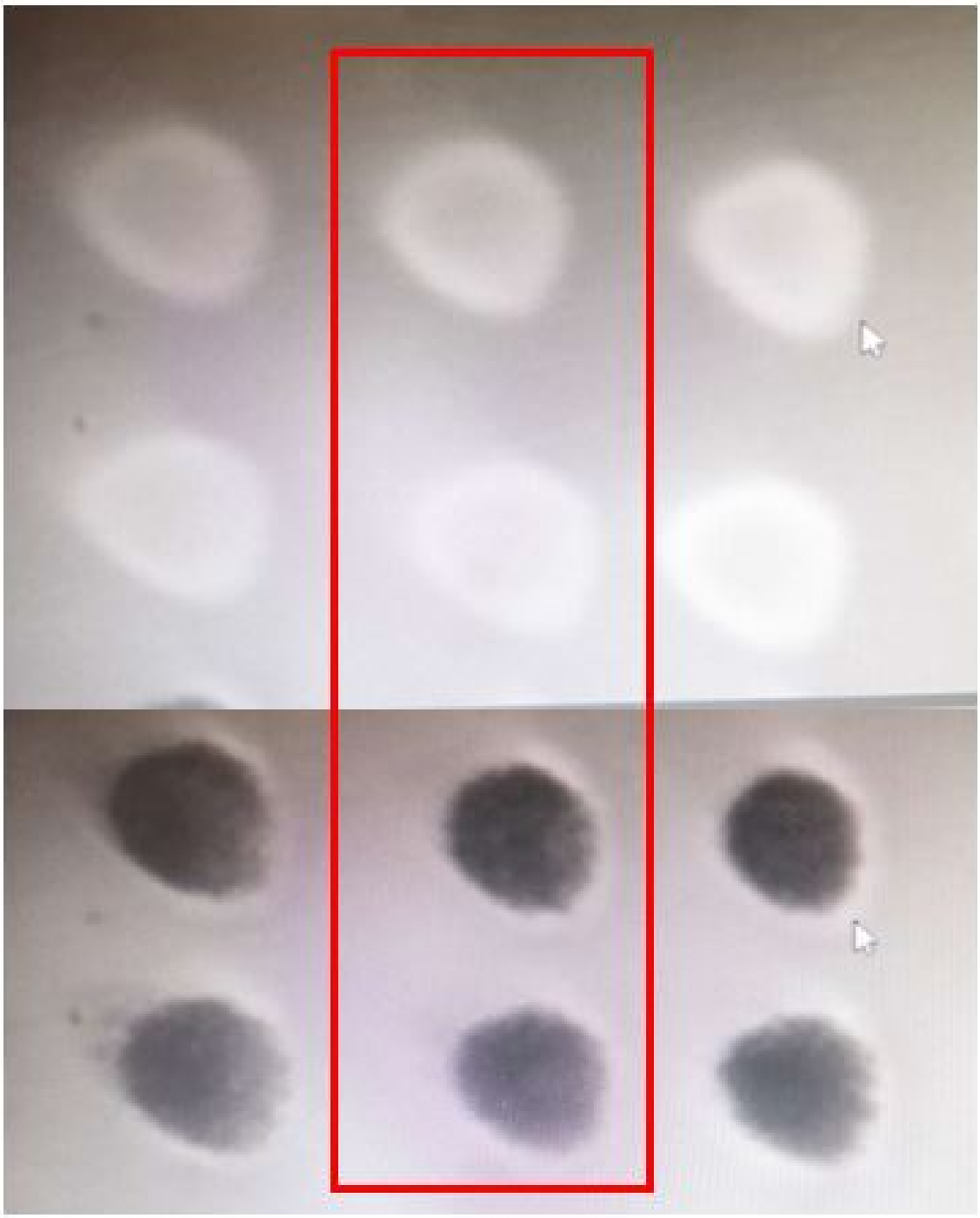

Figure 4.15: Optical microscope image and SEM images of ablated morphology when irradiated with 400nm laser beam. Optical microscope image at different pulse numbers N. Within the red frame from top to bottom, the applied pulse number gradually increases as N=1, N N=10, N=50 and N=100 when irradiated with the same fluence F= $0.113 J/cm^2$.

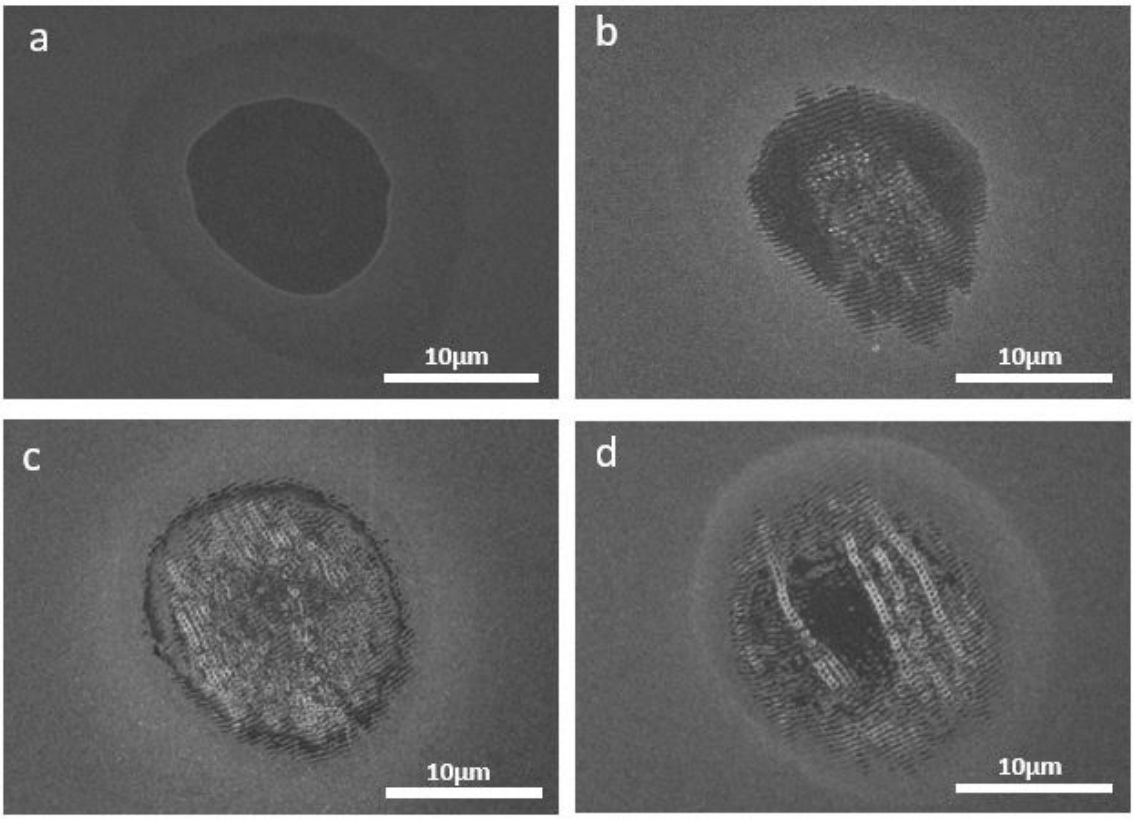

Figure 4.16: Optical microscope image and SEM images of ablated morphology when irradiated with 400nm laser beam. (a) - (d) are the corresponding SEM images of the ablated area at different pulse numbers after cleaning.

4.5 Conclusion

Multi-shot ablation thresholds were investigated for polycrystalline copper and single crystalline silicon using a Near Infrared femtosecond laser, with a wavelength of $800nm$ and pulse duration of 130 fs. Fluences above and below the single-shot threshold were used in the study. The results are compared to two existing incubation models for a better understanding of the incubation effect. The first model, the basic model, assumes the multi-shot ablation thresholds, and the single-shot ablation threshold is related by a power law giving an incubation coefficient, S, for a material. The second more sophisticated model, the generic model, includes additional effects of sub-ablation threshold and multi-shot absorption change. Ablation thresholds were determined from the data generated by using fluences above the single shot threshold. The single shot ablation thresholds are determined to be $0.87J/cm^2$ and $0.34J/cm^2$ for polycrystalline copper and single crystalline silicon, respectively, when the data are fitted to the power law. The F_1 and S for polycrystalline copper and single crystalline silicon found in this study are consistent with the literature results. The power law provides a good fit to the copper data for $N < 1000$ and the full range of the silicon data. The generic incubation effect models provide a reasonable fit for both materials.

From the data generated by using fluences below the single shot ablation threshold ($F < F_1$), multi-shot ablation thresholds, $F_{th}(N)$, and sub-ablation thresholds, F_∞, were determined. The sub-ablation thresholds are estimated to be $F_\infty = 0.18J/cm^2$ and $0.21J/cm^2$ for polycrystalline copper and single crystalline silicon, respectively. In the case of copper, the $F_{th}(N)$ for the $F < F_1$ case is consistent with those of the $F > F_1$ case. In the case of silicon, the $F_{th}(N)$ for the $F < F_1$ case is significantly higher than those of the $F > F_1$ case. Thus, $F_{th}(N)$ values for silicon found using $F > F_1$ are not useful for femtosecond nanomilling studies. Both incubation effect models are inadequate for describing the silicon data. New models

which include other effects, such as multi-photon absorption and defect physics in silicon, may be needed to describe silicon data fully.

The multi-shot ablation thresholds and incubation effects for Si thin films due to 800 nm irradiation were also investigated. The results indicate that Si thin films have lower ablation thresholds than the bulk Si, but their incubation coefficients are similar.

In addition, the multi-shot ablation thresholds and incubation effect for Si thin films due to 400 nm irradiation were also investigated. For 400nm laser irradiation, the surface modification area did not show significant enlargement with the increase of pulse numbers, indicating a weak incubation effect. Thus, the behaviour of the incubation effects for the 400 nm case is significantly different from that of the 800nm case.

The study in this chapter provides important information for guiding ultra-high precision femtosecond laser nanomilling studies and other multi-shot low fluences applications for copper and silicon.

Chapter 5

Multi-shot near-infrared femtosecond laser tuning of silicon microring resonators

5.1 Preface

The materials in this chapter have been published in Optics communication as R. Zhang et al., "Multi-shot near-infrared femtosecond laser tuning of silicon microring resonators.", Optics Communications 560 (2024): 130446.

5.2 Introduction

Silicon photonics has emerged as a promising platform for advanced on-chip integrated optical devices and microelectronic circuits during the last decades. Owing to its favourable optical properties, such as a high index of refraction and transparency to telecommunication wavelengths and potential applications, the field has attracted a large amount of interest from both the academic community and industry[48, 71, 72]. The waveguide's large refractive index refraction contrast in Silicon on Insulator (SOI) chips enables high-density device integration due to the high modal confinement[73, 74]. However, silicon photonics devices suffer from extreme sensitivity to fabrication precision and tolerance. Even highly advanced fabrication processes still introduce uncertainty in device shape and dimension, significantly deviating from a

device's designed spectral response. For example, a variation of 1 nm width in a Si-based micro ring resonator waveguide can shift the operating resonance wavelength by 2 nm or more [48, 49]. The fabrication errors mentioned above have prompted the development of methods of post-fabrication correction for permanently tuning the operation wavelength of devices to ensure their performance. Approaches include localized recrystallization via ion implantation [50], deposition of the photosensitive layer generating a high-index refraction layer [52], e-beam trimming [51, 55], UV laser trimming of hydrogenated amorphous silicon waveguide [53], visible laser annealing of hydrogen silsesquioxane cladding [54], and ultrafast laser-induced crystalline modifications and ablation [2, 5].

The main advantages of the post-fabrication techniques using laser pulses include the fact that the operations can be conducted rapidly in the ambient environment using relatively simple laser materials processing setups. In previous work, we found that the resonance wavelengths of silicon microring resonators can be tuned with single femtosecond pulses of a Ti: Sapphire laser system at a wavelength of 800 nm(fundamental frequency) [5, 58] and 400 nm (second harmonic frequency) [2]. The desired operation wavelength of a silicon photonic device, such as a ring resonator, can be permanently increased or decreased when its silicon waveguide is irradiated by a single femtosecond laser pulse with fluences above the crystalline modification threshold or the ablation threshold, respectively. The positive shifts in resonance wavelength are proportional to the increasing laser fluence [2]. When the laser fluences are increased to values beyond the ablation threshold of silicon, negative shifts result [2]. The physical mechanism responsible for the positive resonance wavelength shift is the change of refractive index of a thin layer of silicon as a result of modifications to the crystalline structures(e.g. amorphization) [5, 58]. The laser-irradiated layer would have a slightly larger refractive index than the crystalline silicon, slightly increasing the waveguide's overall refractive index. The physical mechanism responsible for the negative resonance wavelength shift is removing a thin layer of silicon due to

ablation. The physical mechanism responsible for the negative resonance wavelength shift is removing a thin layer of silicon due to ablation. For laser tuning using single near-infrared femtosecond laser pulses with fluences above the single shot ablation threshold, the surface and subsurface damages led to significant roundtrip microring losses [5]. Nanomilling of silicon with relatively small surface and subsurface damage was reported by using Atomic Force Microscope cantilever tips [56, 57]. Still, it is also possible to accomplish similar results using multi-shot laser nanomilling [1].

It was well established in the materials processing field that, when using multiple femtosecond laser pulses to irradiate a sample on the same spot, the ablation thresholds would depend on the number of irradiated pulses. The multi-shot ablation threshold can be significantly lower than the single-shot ablation threshold because of the incubation effect [35, 39, 75, 76]. It is believed that during such multi-shot irradiation of a silicon sample, even at relatively low fluences significantly below the single-shot ablation threshold, each subsequent laser pulse would generate an increasing number of defects, a process called the incubation effect. Ultra-high precision "nanomilling" of copper to depths of several nanometers was demonstrated using multiple femtosecond laser pulses with fluences below the single-shot ablation threshold by taking advantage of the incubation effect [1, 69]. The gentler "nanomilling" process may have an advantage over the single-shot ablation process, resulting in reduced waveguide losses during the negative shift tuning process. In this chapter, we report a study of post-fabrication tuning of silicon ring resonators using the multi-shot tuning approach.

5.3 Experimental setup

Figure. 5.1 shows a schematic diagram of the experimental setup used to perform multishot irradiation of silicon microring resonator. The femtosecond laser source used is a commercial Ti: sapphire laser system (Coherent Legend), which can generate laser pulses with pulse energy up to 0.5 mJ, a repetition rate of 1kHz, and a pulse

duration of ∼130 fs at 800 nm wavelength. The PTP and RMS stability of the laser output are observed to be within 15% and 3%, respectively. The laser pointing accuracy consists of two factors: the alignment accuracy and shot-to-shot pointing uncertainty of the laser system. The alignment accuracy of the beam for locating on the waveguide center of the resonator is measured to be approximately ± 1.5 µm, and the pointing uncertainty of the laser system on the sample surface is estimated to be approximately 1 – 2 µm. The sample targets (silicon ring resonators) were mounted on a 3D motion stage with a step resolution of 200 nm. The laser beam was focused using a 10 x long working distance microscope objective irradiating the samples at 0° angle of incidence, giving a semi-Gaussian beam profile with $1/e^2$ spot radius of 13.1 µm by moving the target away from the focus position by a distance of 400 µm(Fig.5.2). Since only the center part of the beam profile will be located on the surface of the microring resonator waveguide (500nm in width), there is ∼ 8 percent difference in the actual energy intensity lower than the measured ones considering the energy intensity profile a standard gaussian one. The double peak shown in the beam profile as shown in Fig.5.2 may due to the quality of the laser beam from output of laser source,and the difference of intensity when fitting to the standard gaussian profile was applied to the calibration of the fluence. The surface morphology and the beam were monitored by a CCD camera together with a 100 cm focal length achromatic lens. The energy of the laser was controlled with a combination of a glan-polarizer and a half-wave plate near the input of the laser source and calibrated using silicon photodiodes PD1 placed before the electric shutter. By tuning the angle of the half-wave plate, the energy deposited on the sample surface can be tuned by combining with the insertion of ND filters ranging from OD 0.5-OD3. The number of pulses for irradiation was controlled using a combination of a fast electric shutter and delay generator to generate the specified number of shots required without shifting the beam profile and location.

The silicon photonics devices used in this study were designed by us and com-

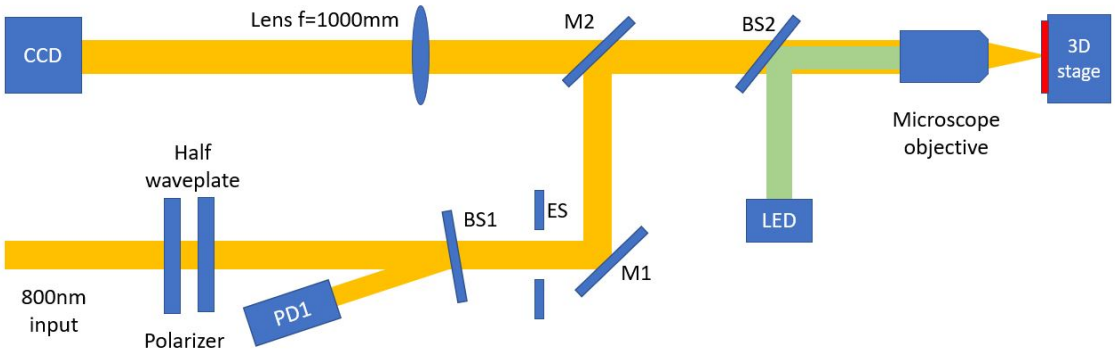

Figure 5.1: Experimental setup of the femtosecond laser irradiation system. M1 and M2 are high-reflection dielectric mirrors at 800nm. ES is the electric shutter for controlling pulse numbers. A combination of glan-polarizer and half-wave plate is mounted near the beam entrance for energy tuning, and the silicon photodiode(PD1) and beam splitter(BS1) are placed before the electric shutter for calibration and monitoring of peak energy deposited on the surface of the sample. A 10x microscope with a long working distance focuses the beam onto the sample for irradiation, and the LED at 532nm wavelength is the light source for illuminating the sample surface for visualization.

mercially fabricated by the Applied Nanotools. Each microring had a diameter of 15 µm and was coupled to a waveguide of 500 nm in width with a gap of 260 nm. It is a rib waveguide with a rib height of 130 nm and a slab height of 90 nm fabricated on the Silicon-on-insulator (SOI) platform. The device is air-clad. The free spectral range of the microring was 5.82 nm.

During the multi-shot irradiation processing, the laser position was located on one side of the microring. Before and after irradiation, the chip was moved to an optical characterization system to measure the response of the microring resonator. A continuous-wave tunable laser(Santec TSL-210V) is applied as the input light source and swept through the wavelength range of 1545-1565 nm. Then, the laser light is adjusted to TM polarization using a manual 3-Paddle Polarization Controller(Thorlabs FPC562) and coupled into the edged-coupled waveguide and resonators by lensed fibers (OZ optics). The alignment of fibers are done using 3D motorized stages with piezo-electric motors(Newport NanoPZ series). The output signal is measured with a High-sensitivity power meter and the final curve fitting of the resonance wavelength

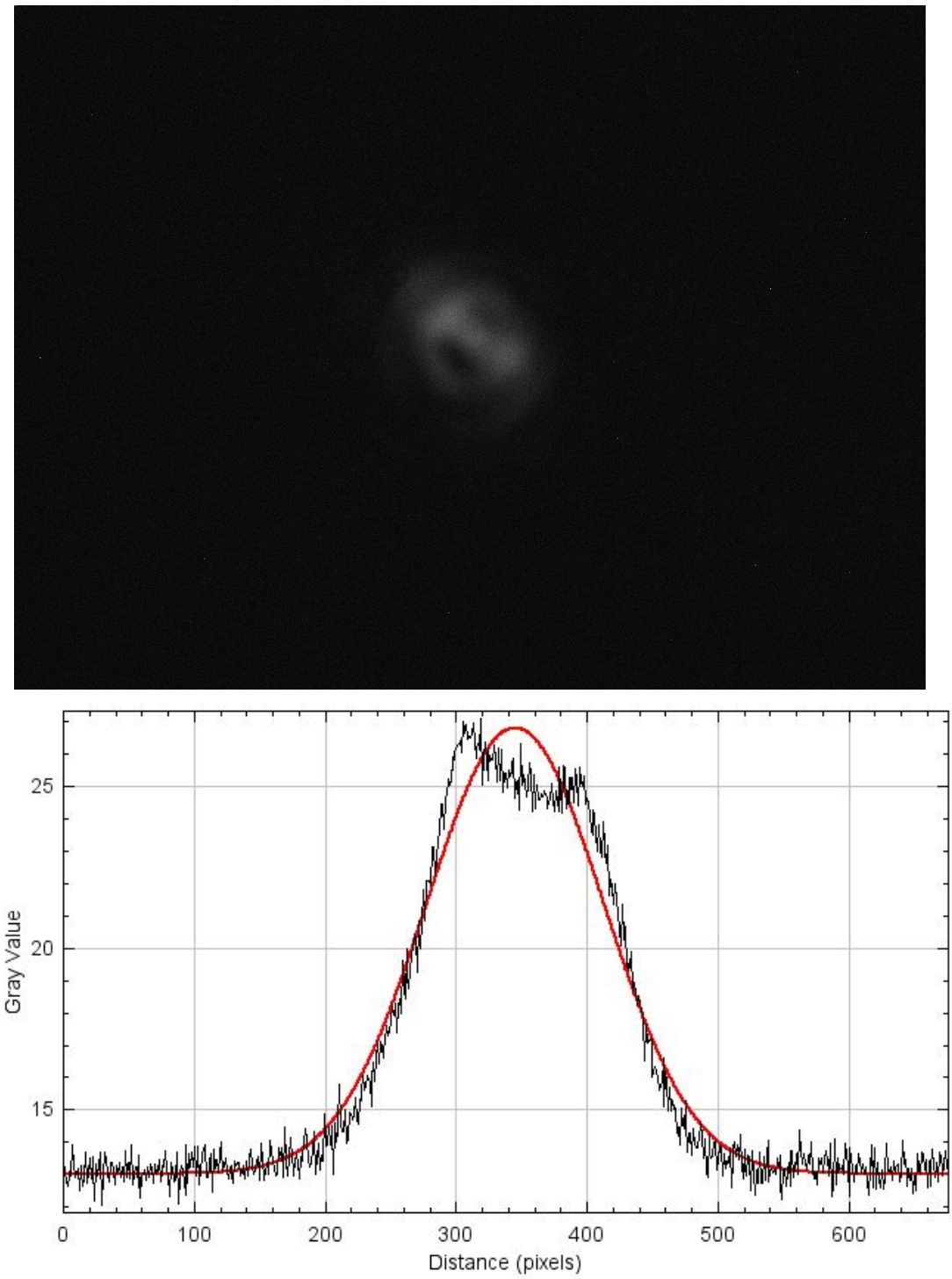

Figure 5.2: Example of the commonly beam profile applied in the experiment. (a) The greyscale image of the Airy beam obtained from a CCD camera. (b) Corresponded intensity distribution of the beam and fitting to the Gaussian profile. The black line is the real intensity profile, and the red one is the Gaussian fitting curve.

was accomplished using a MATLAB program. Figure. 5.3 shows examples of the measured microring resonance spectra before and after irradiation the same as reported in [72]. The roundtrip loss can be derived from the transmission at the through port using the measured power transmission versus frequency which is given by

$$\frac{P_{\text{thru}}}{P_{\text{in}}} = \frac{\tau^2\left(1 + a_{rt}^2 - 2a_{rt}\cos\varphi_{rt}\right)}{1 + \tau^4 a_{rt}^2 - 2\tau^2 a_{rt}\cos\varphi_{rt}} \tag{5.1}$$

where P_{in} is the input optical power, P_{thru} is the transmitted light power at the through port, τ is the field transmission coefficient of the coupling junctions between the waveguides and microring, $\varphi_{\text{rt}} = \eta_{\text{eft}}(2\pi/\lambda)2\pi\text{R}$ is the roundtrip phase and a_{rt} the roundtrip field attenuation factor of the microring. By curve-fitting the measured transmission spectrum at the through port with the expression in Eq. 5.1, we can obtain the roundtrip attenuation a_{rt} along with the transmission coefficient τ. Examples of the curve fit are shown by the dashed lines in Fig. 5.3.

5.4 Multi-shot Laser Tuning Results

Silicon microring resonators are irradiated with 130 fs laser pulses, and the peak fluence of each pulse ranges from $0.0045 J/cm^2$ to $0.069 J/cm^2$ (pulse energy from 12 nJ to 186 nJ). The number of shots (N) at each irradiated location was either 10 or 100 pulses. A semi-log plot of the tuning curves, i.e. resonance wavelength shifts versus the average fluence of each laser shot, for N = 1, 10, and 100 are shown in Fig. 5.4. The N= 1 results are reproduced from our previous studies[58] with laser pulses having similar conditions as in this study for comparison. The data points and error bars for the N = 10 and N = 100 tuning curves are the average and standard deviation of 3 to 9 irradiated samples, respectively. The errors in the resonance wavelength shifts are due to the laser pointing uncertainty, which can be larger than a micron. The laser pointing uncertainty can include the initial alignment uncertainty and the subsequent shot-to-shot variations due to laser beam pointing fluctuations [77]. The laser pointing

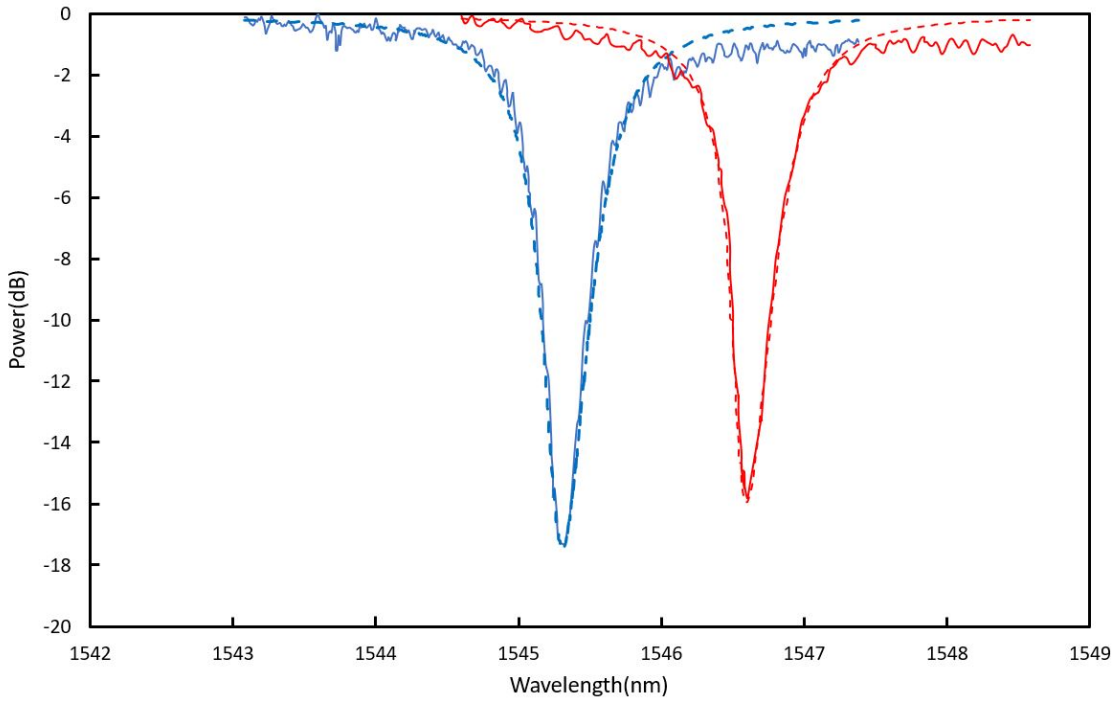

Figure 5.3: Examples of Measured original resonance wavelength (solid blue) and measured data(solid red) of the microring resonator after laser irradiation with a laser fluence of $0.055 J/cm^2$ for N = 10 pulses. The corresponding curve fittings of the measured data are shown in dashed lines, respectively.

uncertainty can lead to significant variation of the effective laser fluence across the 500 nm width of the waveguide. If the center of the Gaussian beam is positioned exactly at the middle of the 500 nm wide waveguide, the fluence across the 500 nm width would be almost constant with the fluence at the two boundaries only 1% lower than that in the middle. However, If the center of the Gaussian beam is positioned 1 μm off the middle of the 500nm width of the waveguide, the fluences at the two boundaries would be 92% and 79% of the peak value.

From Fig. 5.4, we observe that the laser thresholds for causing a permanent wavelength shift are lower for the multi-shot cases (N = 10 and 100) compared to the single-shot case, being as low as $0.02J/cm^2$ for the 10-shot cases and $0.05J/cm^2$ for the single-shot case. In addition, while the wavelength shift increases linearly with the fluence for the single-shot case (until reaching the ablation threshold of $0.19J/cm^2$ [58]), the multi-shot tuning curves consist of 3 regions: (i) a region of the positive resonance wavelength shifts increase with increasing laser fluences (region A "increasing region"), (ii) a region where the positive resonance wavelength shifts are approximately constant (region B "plateau region") and (iii) a region where the positive resonance wavelength shifts decrease with increasing fluences and eventually the resonance wavelength shifts became negative (region C "decreasing region").

Region A ("increasing region"): for N = 10 cases, within the fluence range of $0.0045J/cm^2$ to $0.014J/cm^2$, the resonance wavelength shifts were below the noise level of 0.07 nm. Within region A from $0.014J/cm^2$ to $0.028J/cm^2$, the resonance wavelength shifts increase with increasing fluences and rise to a value of around 4.5nm at a fluence value of around $0.028J/cm^2$.

Region B ("plateau region"): For the N = 10 case, in the fluence range from $0.028J/cm^2$ to $0.048J/cm^2$, the resonance wavelength shifts are approximately constant at around 4.5 nm. A plateau region was also observed for the N = 100 case with a slightly lower value at around 4 nm, but the values had larger fluctuations than those in the N = 10 case. The origins of the plateau region and the fluctua-

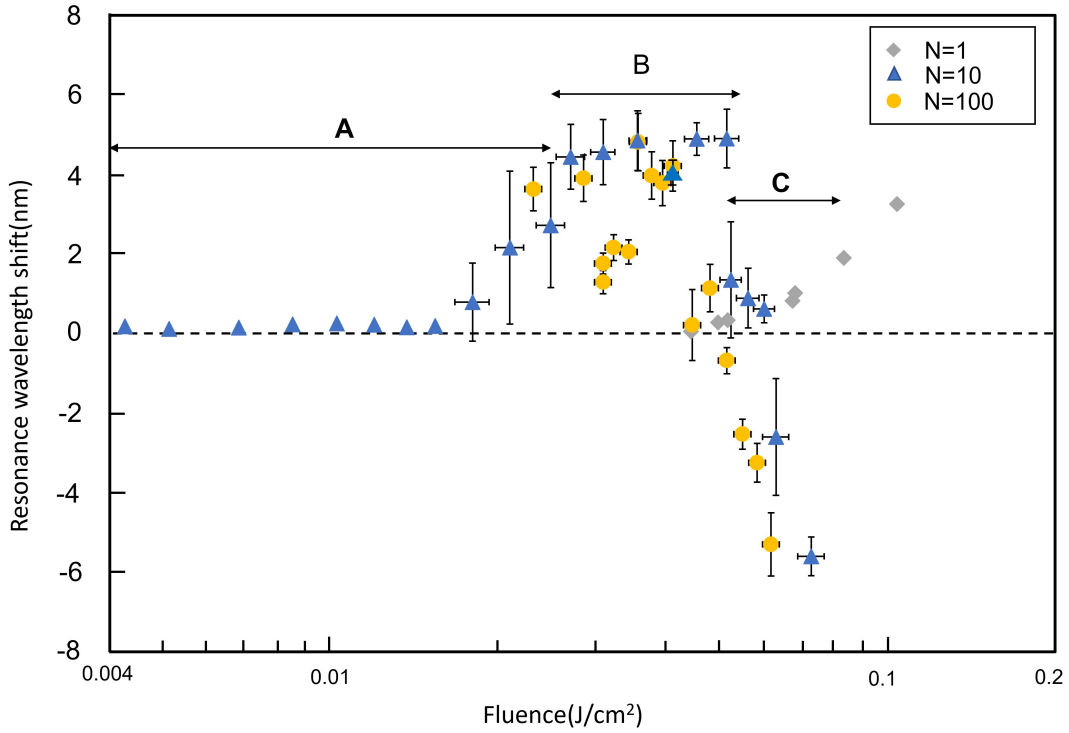

Figure 5.4: Resonance wavelength shifts of the resonators after irradiation with different fluences at a pulse number of N=1, 10, and 100. The N=1 data points are reproduced from reference [58] for comparison.

tions in the N = 100 case need further investigation. We speculated that each laser shot may modify a small region in the light absorption layer until the layer is fully modified and reaches the observed saturation. The fluctuations in the N = 100 case may result from the laser-pointing uncertainty, energy fluctuations, and focal position variations where small variations in fluence from shot to shot have a larger effect on the incubation behaviour. In our previous study [1] of multi-shot laser nano milling of copper, stochastic behaviour of ablation events is observed. Such stochastic behaviour in multi-shot laser nano milling can also contribute to the large fluctuations in the N = 100 case.

Region C ("decreasing region): for the N = 10 case, for the laser fluence larger than $0.048 J/cm^2$, the resonance wavelength shifts decrease with increasing laser fluence likely because of the amount of material removal increases with increasing laser fluence. For the N = 100 case, the behaviour is similar with the onset of the decrease of resonance wavelength shifts starting at a lower laser fluence value of $0.034 J/cm^2$. The decrease in the wavelength shift with increasing laser fluence is likely caused by a thin layer of material being removed by the ablation process, resulting in a decrease in the effective index of the waveguide. The resonance wavelength shift becomes negative when the negative effective index change caused by ablation is larger than the positive index change caused by the amorphization of the silicon material. The fluence where the resonance wavelength shift becomes negative is lower for N = 100 than for N = 10, the values being $0.052 J/cm^2$ for N = 100 and $0.063 J/cm^2$ for N = 10. For the single-shot case, the ablation threshold where the wavelength shift became negative was much higher at $0.19 J/cm^2$ [58].

Figures .5.5 (a) and (d) show examples of positive and negative wavelength shifts of the microring resonance spectra for the N = 10 case. The positive wavelength shift was obtained at a laser fluence of $0.055 J/cm^2$ while the negative wavelength shift was obtained at a larger laser fluence of $0.065 J/cm^2$. For the positive shift case, the SEM image of the device after irradiation in Fig. 5.5(c) shows no surface damage on

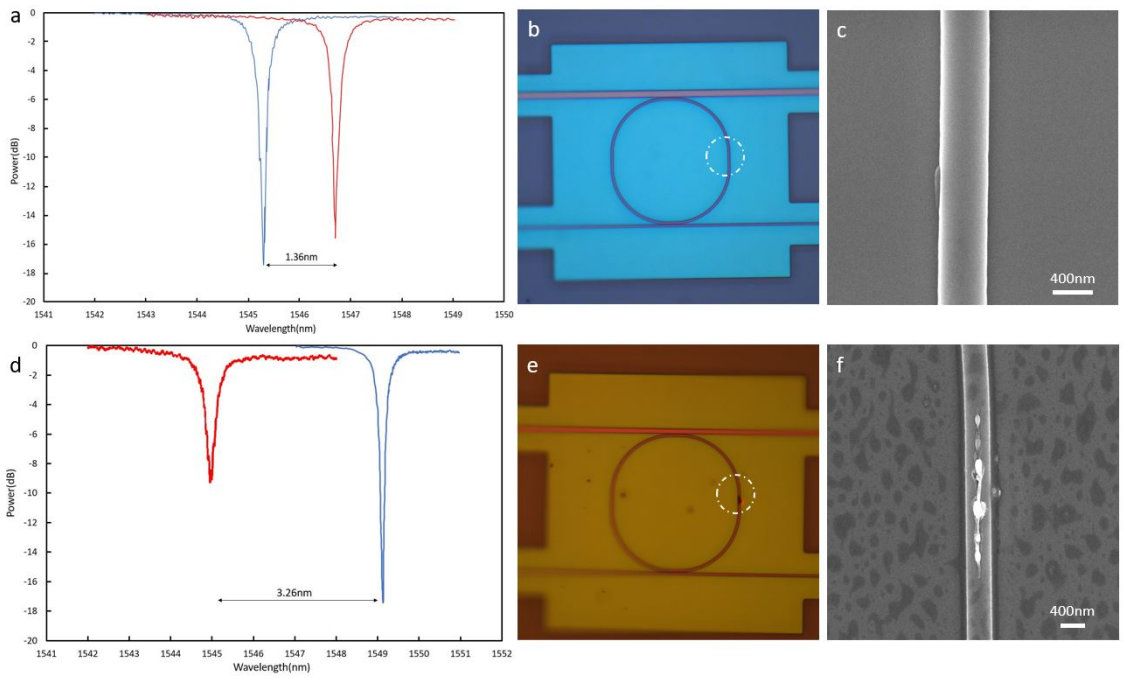

Figure 5.5: Examples of positive and negative resonance wavelength shifts with N = 10 pulses. The spectral response is shown before irradiation (blue curve) and after irradiation (red curve). (a) A positive wavelength shift of 1.14 nm was achieved when irradiated at $0.055 J/cm^2$. (b) and (c) are corresponding optical microscopy and SEM images respectively for case (a). (d) A negative wavelength shift of -3.26 nm was achieved at a fluence of $0.063 J/cm^2$. (e) and (f) are corresponding optical microscopy and SEM images of the irradiated area respectively for case (d).

the microring waveguide. However, for the negative shift case, a change in surface morphology on the waveguide can be observed in the SEM image in Fig. 5.5(f).

Measurement of the averaged roundtrip losses in the waveguide before and after-irradiated microring resonator can provide information about the change in the quality of the microring resonators after laser processing. The roundtrip losses a_{rt}^2 are obtained by performing curve fitting of the measured resonance spectrum using Eq. 5.1 (see Fig. 5.3). Figure .5.6 shows the change of roundtrip loss after irradiation versus the resonance wavelength shift for N = 10 and N = 100, respectively. For N = 10, the induced roundtrip losses are below 0.5 dB in both the negative and positive shift regimes. For N = 100, the induced roundtrip losses are slightly larger than the N=10 case, with the largest loss value reaching 0.8 dB. The error bars of the

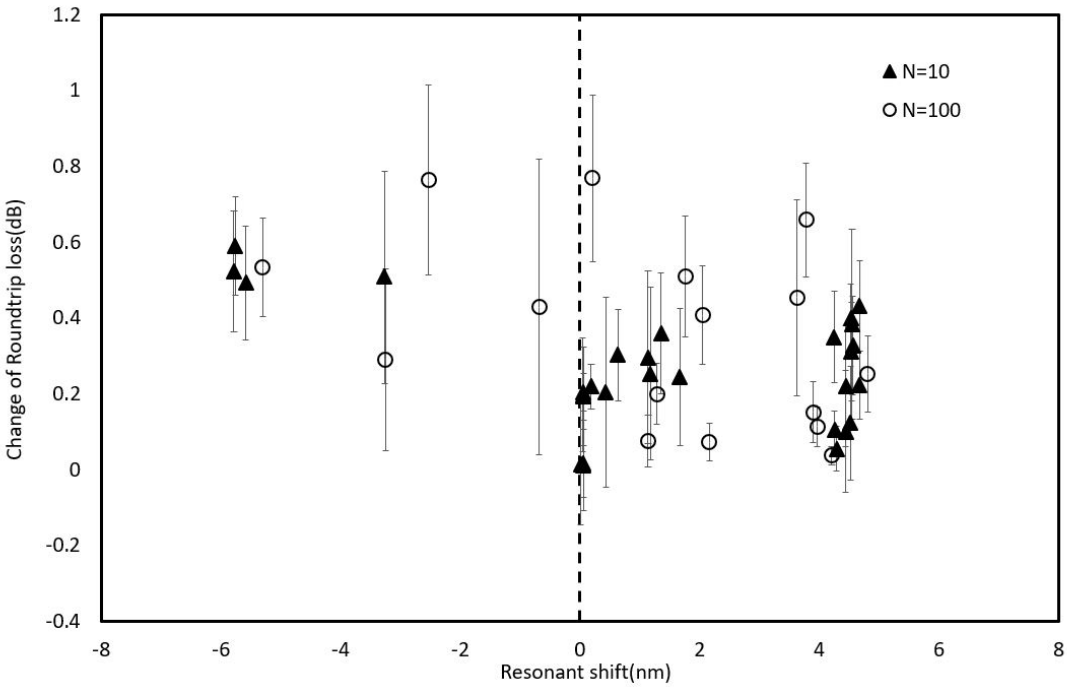

Figure 5.6: Induced roundtrip losses for the microring resonators as a function of resonance wavelength shifts for the N=10 (solid triangle symbol) and N =100 (hollow circle symbol).

roundtrip loss in the plots are caused by uncertainty in achieving the best curve fit of the measured resonance spectra. One source of this error is due to the coherent back-scattering inside the resonator, which causes splitting of the resonance spectrum, resulting in errors in the extracted roundtrip loss [75, 78]. The uncertainty in defining the background baseline of the resonance spectrum also contributed to the fitting error.

5.5 Scanning Electron Microscope and Raman study of surface morphology

Various laser-induced defects and phase transformations have been studied by single and multi-shot irradiation of single crystal silicon with fluences above the melting threshold using Near-infrared femtosecond laser pulses [14, 44, 45]. The authors in [45] used various numbers of pulses at $0.15 J/cm^2$, about 15% above the single shot

melting threshold, with a wavelength of 1030 nm and a pulse width of 300 fs. For irradiation with a single shot, two layers were observed: a top layer of amorphous silicon where the laser fluences are sufficient for melting and a dislocation layer underneath where the laser fluences are below the melting threshold but sufficient to induce dislocations and lattice distortions. As the number of shots increased, the dislocation layer was enlarged, and a small portion of the amorphous silicon layer was removed. Further increase in the number of shots significantly increased the dislocation region, leading to the formation of a high-density defect layer and the appearance of macroscopic damage to the surface layer. The visible surface damage was in the form of Laser-Induced Periodic Surface Structures (LIPSS) and microholes, which would be accompanied by a relatively larger amount of material removal. Although the laser fluences used in our study were significantly below the melting threshold, the mechanisms observed in [14, 44, 45] provide useful insights for our study. Based on the results from Scanning Electron Microscopy (SEM) and Raman Spectroscopy with N = 10, the evolution of multi-shot femtosecond irradiation on crystal silicon with increasing fluences (these fluences are significantly lower than the single-shot melting threshold) can be described below:

I. For laser fluences below $0.014 J/cm^2$, no modifications of the surface can be detected by SEM (Fig. 5.7a) or Raman Spectroscopy. Even if there are some laser-induced dislocations, the amount is sufficiently small so no change in the induced index refraction could be detected.

II. When laser fluences are increased to higher than $0.014 J/cm^2$ ("increasing" region A of Fig. 5.4), the laser irradiation generated dislocations and lattice distortions due to plastic deformation and higher temperature [45]. The amount of dislocations and lattice distortions grows with increasing fluence, leading to an increase in induced index refraction and wavelength shift. However, no surface modifications can be detected by SEM or Raman Spectroscopy (Fig .5.8 yellow and gray traces).

III. As laser fluences are further increased to $0.028 J/cm^2$ (beginning of the

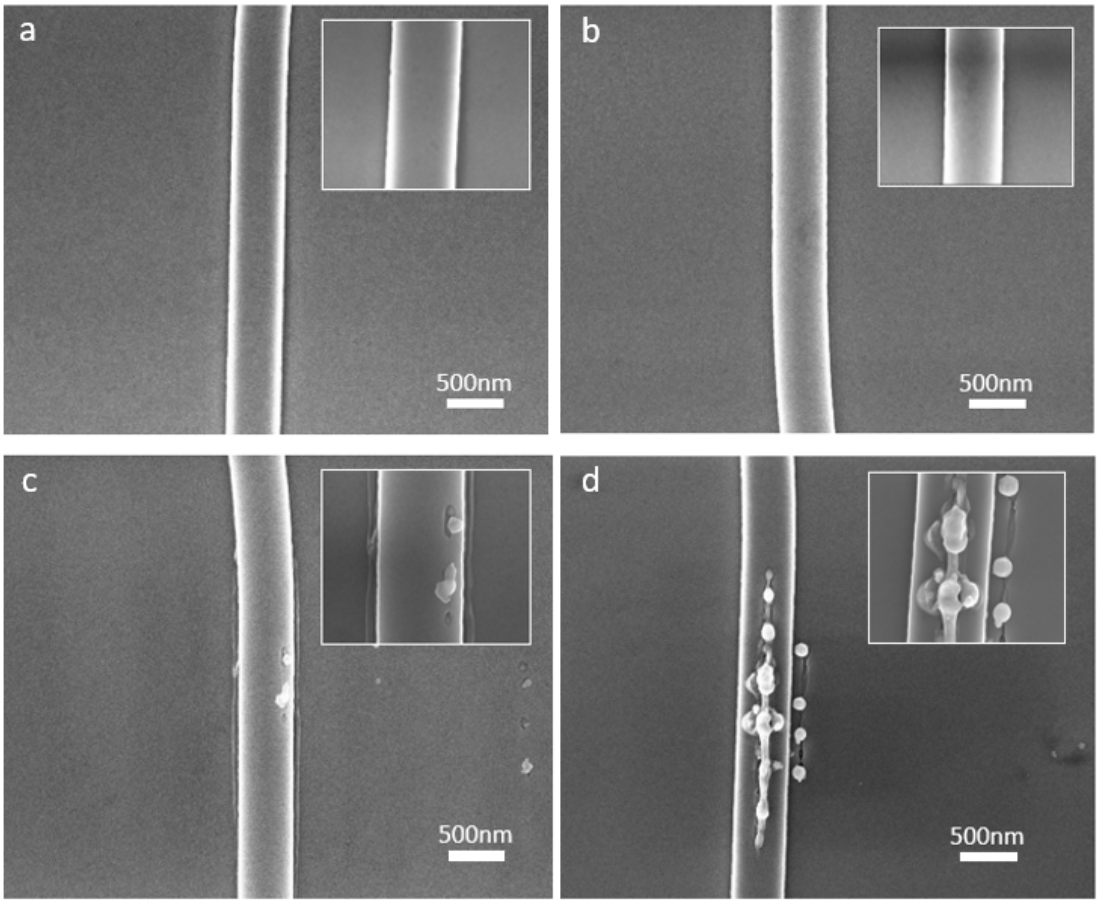

Figure 5.7: SEM images and enlarged details of the irradiated area on microring resonators at different laser fluences for N=10 pulses. (a) $0.012 J/cm^2$.(b) $0.03 J/cm^2$.(c) $0.06 J/cm^2$.(d) $0.063 J/cm^2$.

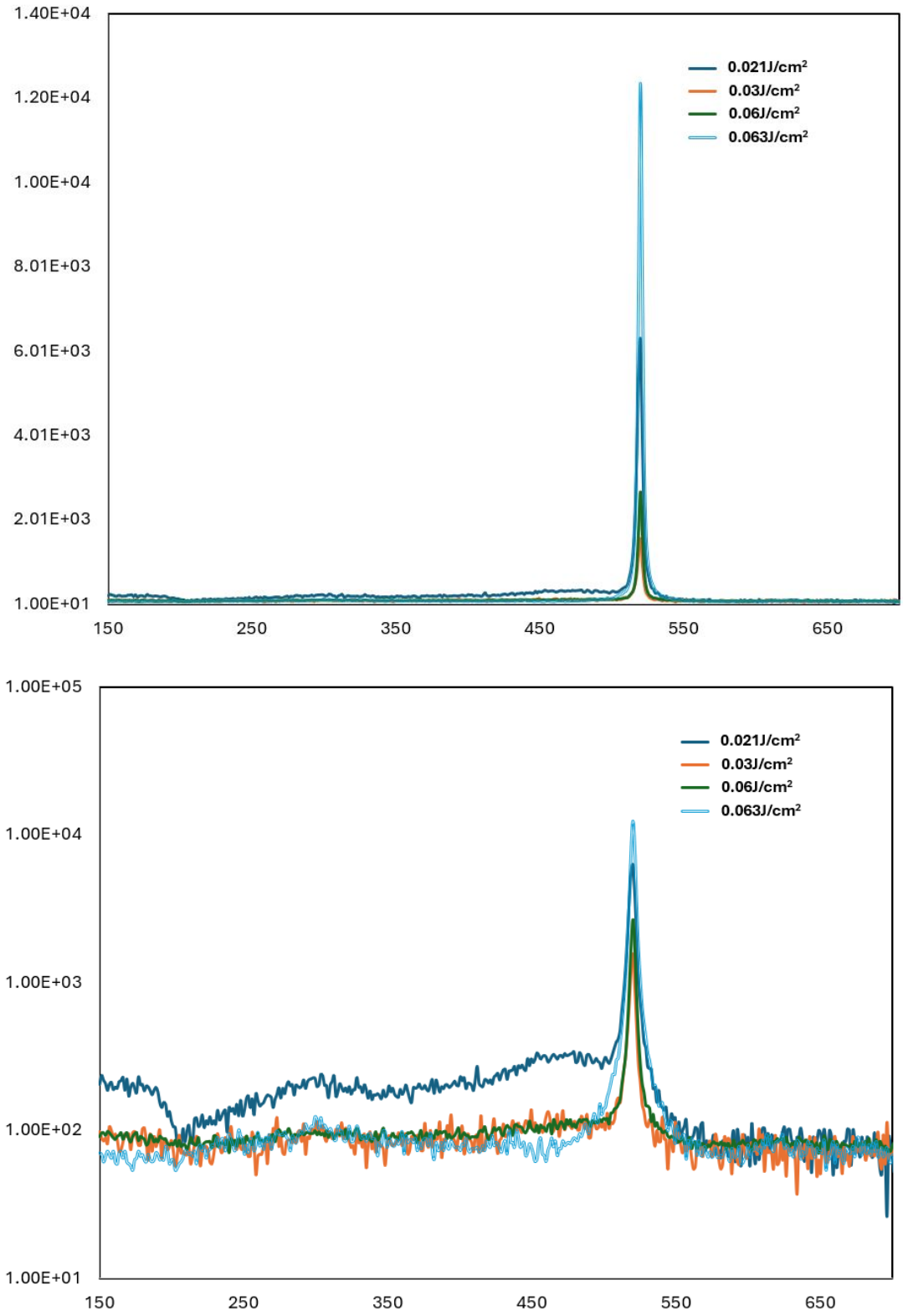

Figure 5.8: (a)Raman spectrum of the irradiated area at different laser fluences from $0.021 J/cm^2$ to $0.063 J/cm^2$, respectively. (b) Raman spectrum on a log scale shows the amorphous silicon peak at $0.063 J/cm^2$.

plateau region B), the increase of induced index refraction begins to saturate, as the generated dislocations and defects completely fill the light absorption layer. SEM and Raman Spectroscopy still show no evidence of surface modification(Fig. 5.7b) or generation of amorphous silicon(Fig. 5.8 grey trace).

IV. When the fluences further increase to $0.05 J/cm^2$ (end of the "plateau" region B and beginning of the "decreasing" region of Fig. 5.4), the decrease of induced index refraction started and eventually led to negative resonance wavelength shifts. The decrease in induced index refraction results from material removal due to surface ablation. Ablation occurs typically when the surface temperature rises beyond the melting point and this is expected to be signified by the presence of amorphous silicon on surface and sub-surface damages [14, 44, 45]. At fluences of $0.06 J/cm^2$ slight surface modifications can be observed from the SEM images (Fig. 5.7c) while no significant amorphous silicon band is present in the Raman spectroscopy measurement (Fig. 5.8 orange trace). At a higher fluence of $0.063 J/cm^2$, nanodroplets, nanostructures and nanocracks can be clearly observed from SEM images (Fig. 5.7(d)) and the amorphous silicon band can be clearly observed from the spectroscopy measurement (Fig. 5.8 blue trace).

5.6 Discussion

From the results in the previous sections, we find that for application in permanent tuning of silicon photonic devices, it is advantageous to use N = 10 for tuning when compared with using N = 100 for a couple of reasons: (i) there are fewer fluctuations in the tuning curve in the plateau region for the N = 10 case and (ii) the induced roundtrip losses in the waveguide is smaller for the N = 10 case and are kept below 0.5 dB in the microring waveguide. The loss increase may not be tolerable for very high Q factor devices, but it is still enough for many applications as demonstrated in [2, 3, 5].

When compared to the single-shot laser tuning, the multi-shot approach also

offers several advantages. Due to the incubation effect, the thresholds for both negative and positive resonance wavelength shifts are significantly lower for the multi-shot approach. This helps reduce the range of laser fluences required for tuning, which allows the use of low-cost compact laser systems with sub-microjoule pulse energies. For example, a fluence of 0.1 J/cm^2, which is above the ablation threshold, can be achieved with a Gaussian beam radius of 13.1 µm at 270 nJ or lower. Another advantage of multi-shot tuning over the single-shot approach is that the induced waveguide losses are significantly lower. For example, for a resonance wavelength shift of 3.4 nm the induced roundtrip loss for a single shot was 1.3 dB [5], while for the N = 10 multi-shot case, the induced losses for all positive wavelength shifts are below 0.5 dB. For negative wavelength shifts, single-shot irradiation with fluences near the ablation threshold induced significant roundtrip microring losses, causing the microring resonances to completely disappear in the measured spectra[5]. For the N = 10 multi-shot case, the induced roundtrip loss is also kept below 0.5 dB for most negative wavelength shifts. The result confirms that the more gentle "multi-shot laser nanomilling" process has an advantage compared to the single-shot ablation process resulting in reduced waveguide losses.

The alignment and pointing uncertainty for a Gaussian beam can lead to significant variations of the effective laser fluence on the waveguide surface. This can be mitigated by using a laser fluence value in the plateau region on the multi-shot tuning curve. In the N = 10 case, a constant resonance wavelength shift of 4.5 nm was observed in the plateau region from 0.028 J/cm^2 to 0.048 J/cm^2. This wavelength shift is directly proportional to the beam waist radius of the Gaussian beam and can be easily changed by varying the microscope to the target distance while keeping the fluence within the plateau region. For example, we found that when we reduced the beam waist radius 4 times to 3.3 µm, the resonance wavelength shift reduced correspondingly 4 times to $\sim$ 1nm. Preliminary experiments have conducted using top-hat intensity profile of 800nm femtosecond laser beams. However, results

are inclusive beacause the less ideal quality of the beam. A summary of the results is provided in Appendix 2.

5.7 Conclusion

We have shown that multi-shot femtosecond laser surface modification of silicon waveguides is a promising technique for tuning silicon microring resonators. Both positive and negative resonance wavelength shifts can be achieved with reasonable induced waveguide losses. Owing to the incubation effect, the laser fluence requirement for the multi-shot approach is significantly lower than the single-shot approach, which allows for the use of low-cost, compact laser systems. Interestingly, we found that three regions ("increasing," "plateau," and "decreasing") exist in the multi-shot tuning curves depending on the relative dominance of the crystalline modification or ablation process. In particular, for N = 10 we have found a new plateau region where the tuning remains stable over a wide fluence range of $0.028 J/cm^2$ to $0.048 J/cm^2$. This region allows for better control of the tuning process, which is less sensitive to fluence fluctuations or laser-pointing uncertainty. SEM and Raman spectroscopy measurements indicated no damage or amorphization occurred during multi-shot femtosecond laser irradiation of crystal silicon at fluences significantly lower than the single-shot melting threshold. Amorphization, material removal and damaged structures were observed when the multishot ablation threshold was reached. The multi-shot irradiation method can potentially provide a low-cost and versatile method for post-fabrication tuning of silicon photonic devices.

Chapter 6

Shot-to-shot characterization of multi-shot tuning of silicon microring resonators irradiated by near-infrared femtosecond pulses at low fluences

6.1 Introduction

As discussed in previous chapters, it demonstrated that post-fabrication tuning of silicon ring resonators can be achieved by giving either a positive or negative shift of resonance wavelength using multiple femtosecond laser pulses at low fluences. The results in Chapter 5 were obtained with a femtosecond laser irradiation system and an optical characterization system for silicon photonic devices located separately in two different laboratories. Each data point in Fig 5.3 of Chapter 5 was obtained by using the following steps: (i) the resonance spectrum of an unirradiated silicon microring resonator (SiMRR) was measured at the optical characterization laboratory; (ii) the silicon microring resonator (SiMRR) was irradiated with a specific number of shots (e.g. N = 10) at a desired low fluence value at the femtosecond irradiation lab; (iii) the irradiated silicon microring resonator (SiMRR) was brought back to the characterization Lab to measure the resonance spectrum of the irradiated circuit and determined the shift of resonance peak. It required a few hours to obtain each data

point and a few days to obtain a complete data set. This introduces many unwanted uncertainties, such as day-to-day fluctuations of laser conditions (laser output energy, pulse duration, beam profile, and variation of laser pointing location between different sample chips. Additionally, the repeated mounting and removal of SiMRR circuit chips from different sample holders can further increase uncertainties and possibly even cause damage to the edge-coupled waveguide, leading to a failure of resonance measurement. These issues motivated the development of an online characterization platform in the femtosecond laser laboratory.

This chapter will discuss the development of an online characterization platform and its use to study the shot-to-shot response of SiMRR circuits. The online characterization platform consists of two sub-systems: (i) a femtosecond laser irradiation system and (ii) an optical characterization system for measuring the resonance spectrum from a silicon photonic device. Compared to the former characterization system described in Chapter 5, the online characterization platform has improved the measuring speed for obtaining a resonance spectrum from a photonic device. The system described in Chapter 5 used the usual method of optical characterization. It involves using a tunable laser as a light source and a photodetector for recording. This method typically requires scanning wavelengths in 0.005 nm steps over a full Free Spectral Range (FSR) range of $\sim$ 5.8 nm. The whole exercise can take more than 20 minutes in addition to the time spent on alignment. During that time, the lensed fiber can move due to environmental vibrations; the drifts often introduce errors in the curve fitting procedure of the resonance spectrum or occasionally even cause a measurement failure. To mitigate these undesired issues, a superluminescent light emitting diode (SLED) is used as the input light source in the characterization system rather than a tunable laser, providing a constant output power level within the 150 nm range of wavelengths from 1450-1600nm. The output signal is analyzed with an Optical Signal Analyzer (OSA), where the scanning of wavelength for an FSR at its highest resolution is less than 1 minute.

6.2 Experimental setup

A diagram of the online characterization platform is shown in Fig.6.1. The laser-irradiation subsystem and optical characterization subsystem share the same sample holder and imaging system, where the laser beam comes perpendicular to the silicon resonator sample surface. The lensed fibers are installed parallel to the sample surface for waveguide edge-coupling.

6.2.1 Laser irradiation system

Figure 6.1 shows a schematic diagram of the experimental setup used to perform multishot irradiation of a SiMRR. The femtosecond laser source used is the first stage amplifier from a commercial Ti: sapphire laser system (Amplitude TW system), which can generate laser pulses with pulse energy up to 20 mJ, a repetition rate of 10 Hz, and a pulse duration of 50 fs. During the experiment, the wavelength of 800 nm or 400nm can be applied. The 800nm wavelength is the fundamental wavelength from the output of the laser system. The laser beam shares part of the optical paths after M5 and then it is focused onto the sample surface. The other components of the laser irradiation system, such as imaging and calibration of pulse energy, are kept the same as detailed in Chapter 4.

An Airy focal spot distribution of the Laser beam was used in the experiment. We pick up the middle part of the airy spot using the aperture, and it creates an intensity profile of a quasi-Gaussian beam with a $1/e^2$ spot radius of 13.4 µm(Fig 6.2), generated by moving the target away from the focus position by a distance of 400 µm.

6.2.2 Optical characterization subsystem setup

A schematic diagram of the optical characterization system is shown in Fig. 6.1b. The laser beam comes perpendicular to the silicon resonator sample surface through a microscope objective. The laser irradiation subsystem and optical characterization

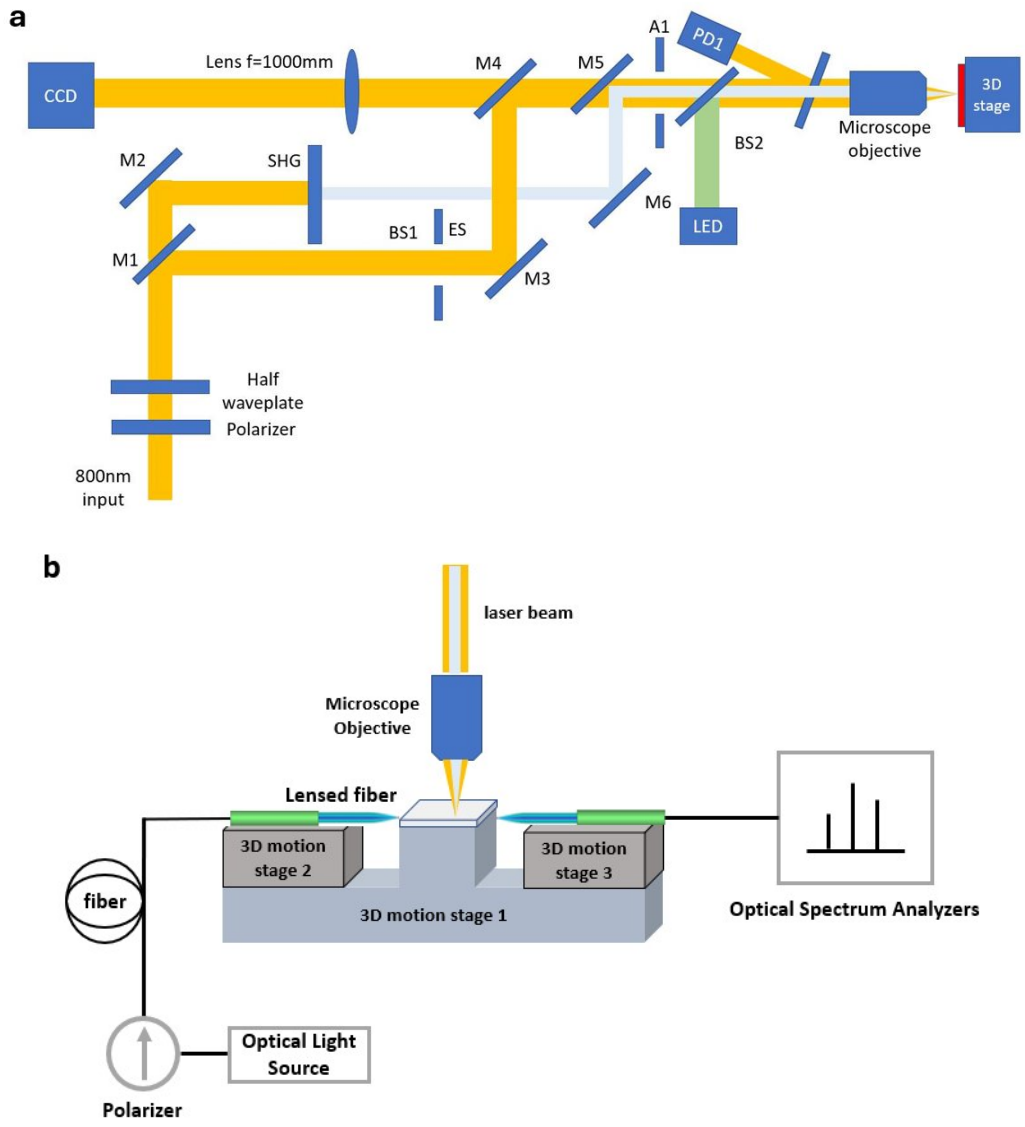

Figure 6.1: (a)Experimental setup of the femtosecond laser irradiation subsystem. M1 and M2 are high-reflection dielectric mirrors at 800nm. ES is the electric shutter for controlling pulse numbers. A combination of glan-polarizer and half-wave plate is mounted near the beam entrance for energy tuning, and the silicon photodiode(PD1) and beam splitter(BS1) are placed before the microscope objective for calibration and monitoring of peak energy deposited on the surface of the sample. A 10x microscope with a long working distance focuses the beam onto the sample for irradiation, and the LED at 532nm wavelength is the light source for illuminating the sample surface for visualization. (b) Experimental setup of the optical characterization subsystem. Two lensed fibres are installed parallel to the sample surface on each side. The fibre-coupled optical light source goes through the fibre polarizer first and connects to the lensed fibre on the input side, and the output fibre is connected to an optical spectrum analyzer for signal processing.

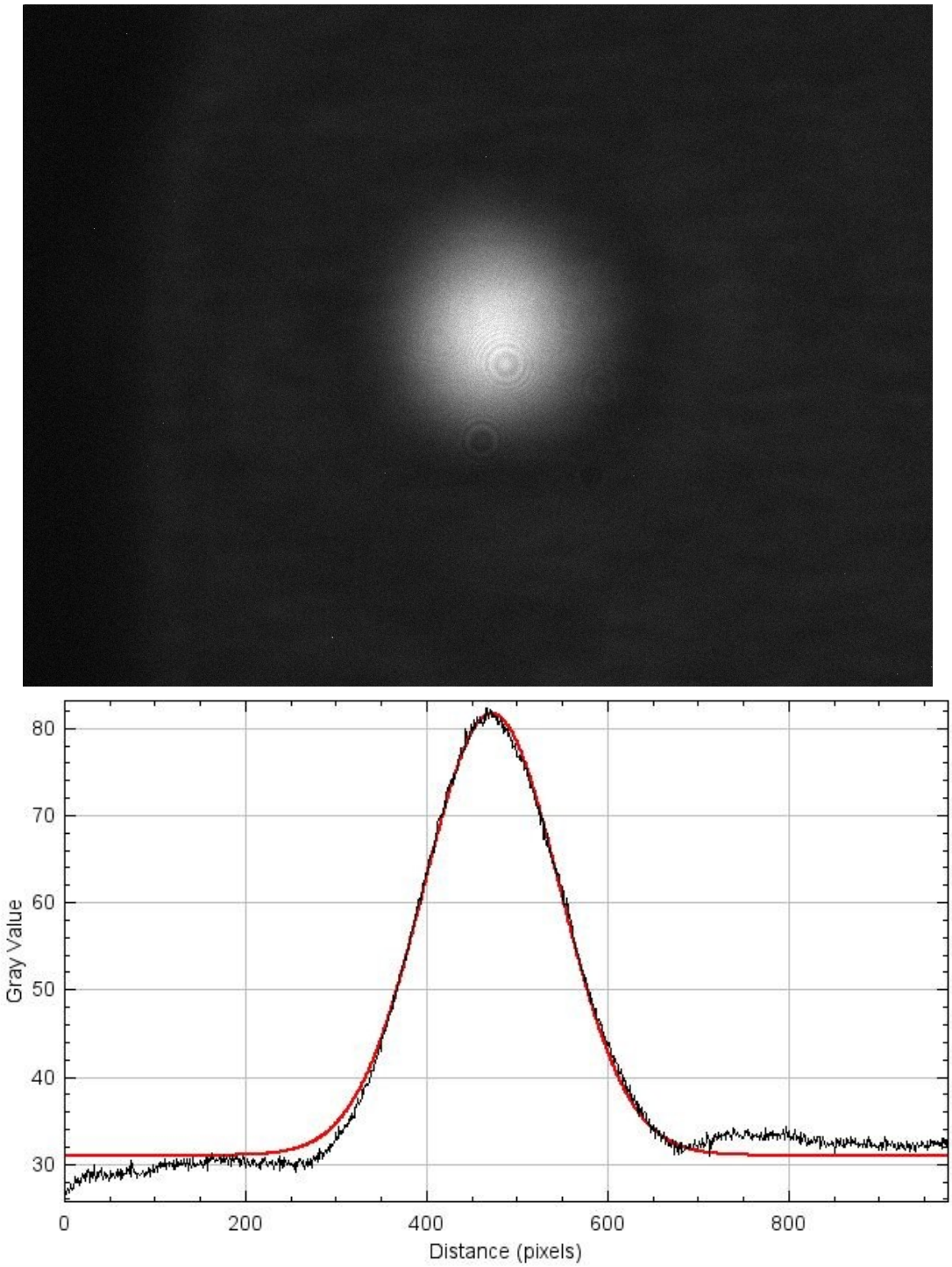

Figure 6.2: Example of the Beam profile applied in the experiment. (a) The greyscale image of the Airy Ring beam obtained from a CCD camera.(b) Corresponding intensity distribution profile of the beam and the fitting to Gaussian profile.

subsystem share the same sample holder. The overall principle and characterization method are similar to that discussed in Chapter 5. However, instead of using a tunable laser and swapping a specific range of wavelengths, two of the key components, Superluminescent LEDs (SLED) and an Optical Spectral analyzer (OSA), are applied in our system for resonant wavelength measurement with high accuracy and efficiency. The SLED equipment is applied as the input light source in the characterization system, which can provide a constant and similar output power level within the 150 nm range of wavelengths from 1450 - 1600 nm. Simultaneously, the output signal from the waveguide is analyzed using an OSA instead of the power meter, which displays the full resonance wavelength spectrum instantaneously. More details of the optical characterization subsystem are provided in Appendix A.

Superluminescent LEDs (SLEDs) are high-power semiconductor light sources with a broadband output optical spectrum, similar to LEDs, but at high power levels, like laser diodes. These SLEDs are based on a PN junction embedded in an optical waveguide. When electrically biased in the forward direction, they show optical gain and generate amplified spontaneous emission over a wide range of wavelengths. SLEDs are designed to have high single-pass amplification for the spontaneous emission generated along the waveguide, but they cannot achieve lasing action due to insufficient feedback. However, they possess high optical output powers and a smooth spectrum achieved by tilting the waveguide with respect to the end facets and applying an antireflection coating to the facets. This combination translates into a small beam divergence, which enables the coupling of the output into a single-mode fibre with an efficiency similar to that of laser diodes.

SLEDs have already been applied to telecommunications with wavelengths within the C-band region. They have been used in fiber optics for testing of components or network management purposes, including coarse wavelength division multiplexing (WDM) characterization, which requires a multi-wavelength source. For optical networks, SLEDs can be used as optical sources to measure the polarization mode

dispersion of optical fibers. In our case, SLEDs can provide a light source with an extreme broadband spectrum covering at least tens of nm range and an almost flat-band energy output.

Optical spectrum analyzers (OSA) are precise instruments used to measure optical spectra, which can be further analyzed. Some typical applications include characterizing light sources like lasers and LEDs, testing optical systems (such as wavelength division multiplexing systems in optical fiber communications networks, where one may need to test the optical powers of different wavelength channels and measure signal-to-noise ratios), measuring the wavelength-dependent transmissivity or reflectivity of optical systems or devices by comparing spectra with and without the device, and characterizing fiber amplifiers (e.g., telecom erbium-doped fiber amplifiers) in terms of wavelength-dependent gain and noise figure.

An example of the full spectrum of our SLED from the wavelength range of 1200 nm to 1700 nm measured by our OSA is shown in Fig. 6.3. The relatively constant output power from 1450-1600nm was used in the characterization study of the unirradiated and irradiated SiMRRs. Most measurements used the flat spectra range of 1540 nm to 1560 nm which is shown in the insert.of Fig.6.3.

6.2.3 Procedures of sample loading to optical characterization subsystem

Before conducting the experiment, a comparison was made between the resonance wavelength obtained from the former characterization system described in Chapter 5 and our online characterization system, using sample microring resonators as shown in Fig.6.4. The results showed that the two measurements of the resonance peak are agreed to within 0.002 nm. This is well within the fluctuations of the resonance wavelength due to temperature variations in the lab.

The alignment procedure involves coupling the lensed fiber to the edged coupler of the waveguide on both sides. A tunable laser, set at a specific wavelength and

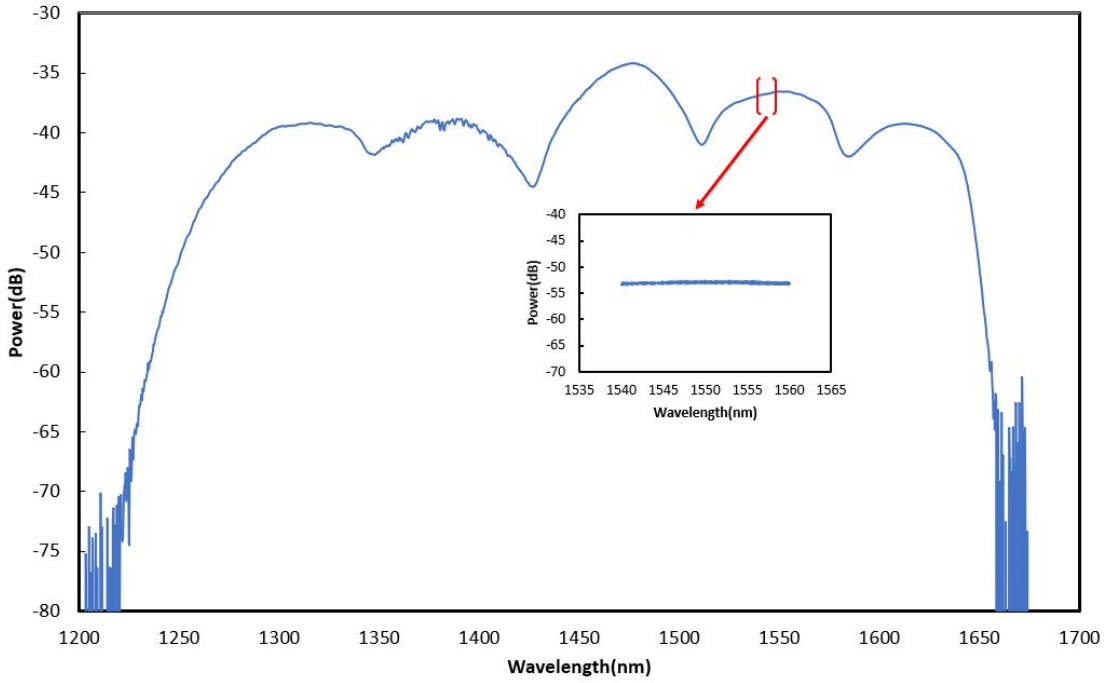

Figure 6.3: Example of SLED spectrum extracted on OSA with wavelength range from 1200nm to 1700nm. The figure insert presents the narrower bandwidth of the spectrum from 1540nm-1560nm.

power (e.g., 1 mW output power at 1550 nm wavelength), is used as the input light source to make monitoring the intensity change on the OSA easier because of its much narrower bandwidth spectrum. The alignment of the lensed fiber on both sides is usually performed alternatively by adjusting the lensed fiber using all the 3-axes-motion stages in small steps until the best coupling efficiency of the laser is obtained. The lensed fiber is usually placed roughly 5 µm away from the edge of the waveguide coupler.

After completing the alignment of the lensed fibers, the input light source is switched to SLED, and the full resonance wavelength spectrum should appear on the OSA display. Final optimization of the OSA settings, such as scanning resolution and number of sampling points, is conducted. The SiMRR is successfully loaded onto the optical characterization subsystem and is ready for further irradiation experiments.

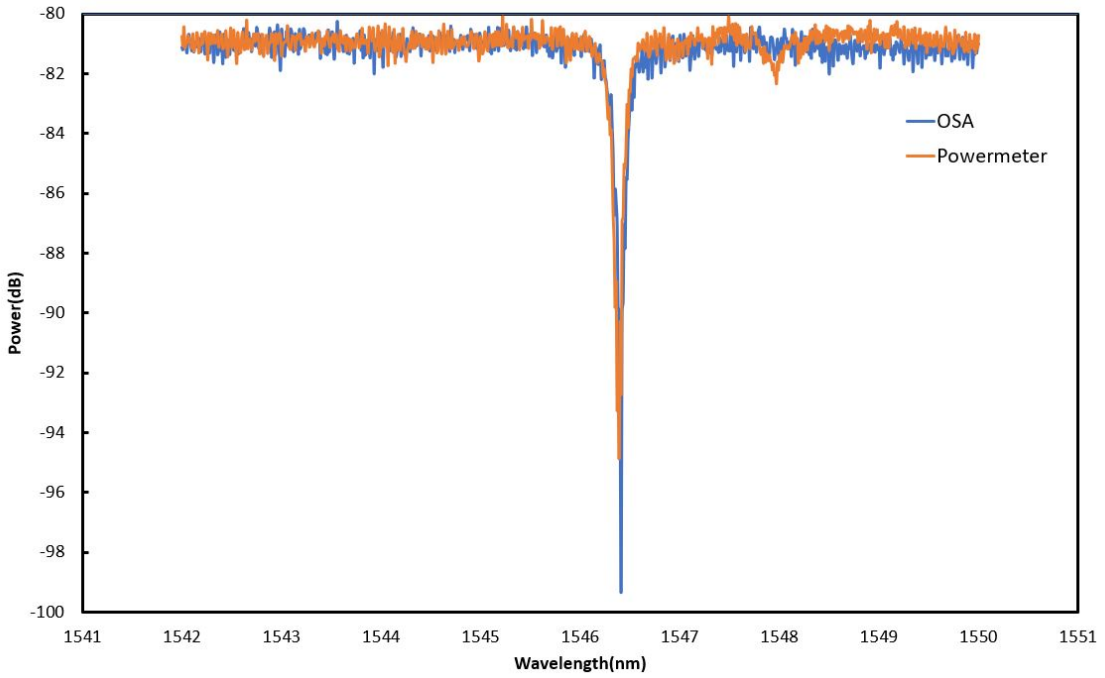

Figure 6.4: An example of the resonance wavelength for racetrack microring resonator by applying the real-time characterization system (blue curve) using SLED as the light source and output coupled to OSA for spectrum measurement, compared to the same resonator measured by optical characterization system as described in Chapter 5(Red Curve).

6.3 Multi-shot Laser Tuning Results

Silicon microring resonators are irradiated with 50 fs laser pulses, and the peak fluence of each pulse ranges from $0.0232 J/cm^2$ to $0.0502 J/cm^2$. The quasi-Gaussian beam of 13.4 um in radius at 800nm wavelength is located at the right side of the racetrack microring resonator structure, with a laser pointing uncertainty of 0.8 um for the initial alignment uncertainty and 1.8 um shot-to-shot variations due to laser beam pointing fluctuations using the same method as described in Chapter 5. The number of shots (N) at each irradiated location usually accumulates from 1 to a few hundred, and the resonance wavelength spectrum of the resonator is measured right after each shot.

The shot-to-shot resonance wavelength spectra for a silicon microring resonator irradiated by fs pulses with a fluence of $0.0232 J/cm^2$ are shown in Fig. 6.5. For the shot number N = 1 to 390, positive shifts for the resonance wavelength spectra are observed. For N = 1 to 40, the spectra are on top of each other, indicating no significant shift in the resonance peaks (blue curves in Fig. 6.5a) is observed. For N = 40 to 150, approximately constant positive shifts of the resonance peaks (purple curves in Fig. 6.5a) are observed. For N = 150 to 390, very small positive shifts of the resonance peaks (green curves in Fig. 6.5a) are observed. Negative shifts for the resonance wavelength spectra are observed for the shot number N = 390 to 790. For N = 390 to 600, approximately constant negative shifts of the resonance peaks (orange curves in Fig.6.5b) are observed. For N = 600 to 790, larger approximately constant negative shifts of the resonance peaks (red curves in Fig. 6.5b) are observed. In this negative shift regime, the resonance curves are slowly broadening, and the height of the resonance peaks are slowly diminishing, indicating that there is increased propagation loss in the waveguide of the microring resonator.

The tuning curves, i.e. the total resonance wavelength shifts versus the pulse number and the corresponding resonance wavelength shifts at $0.0232 J/cm^2$, is shown

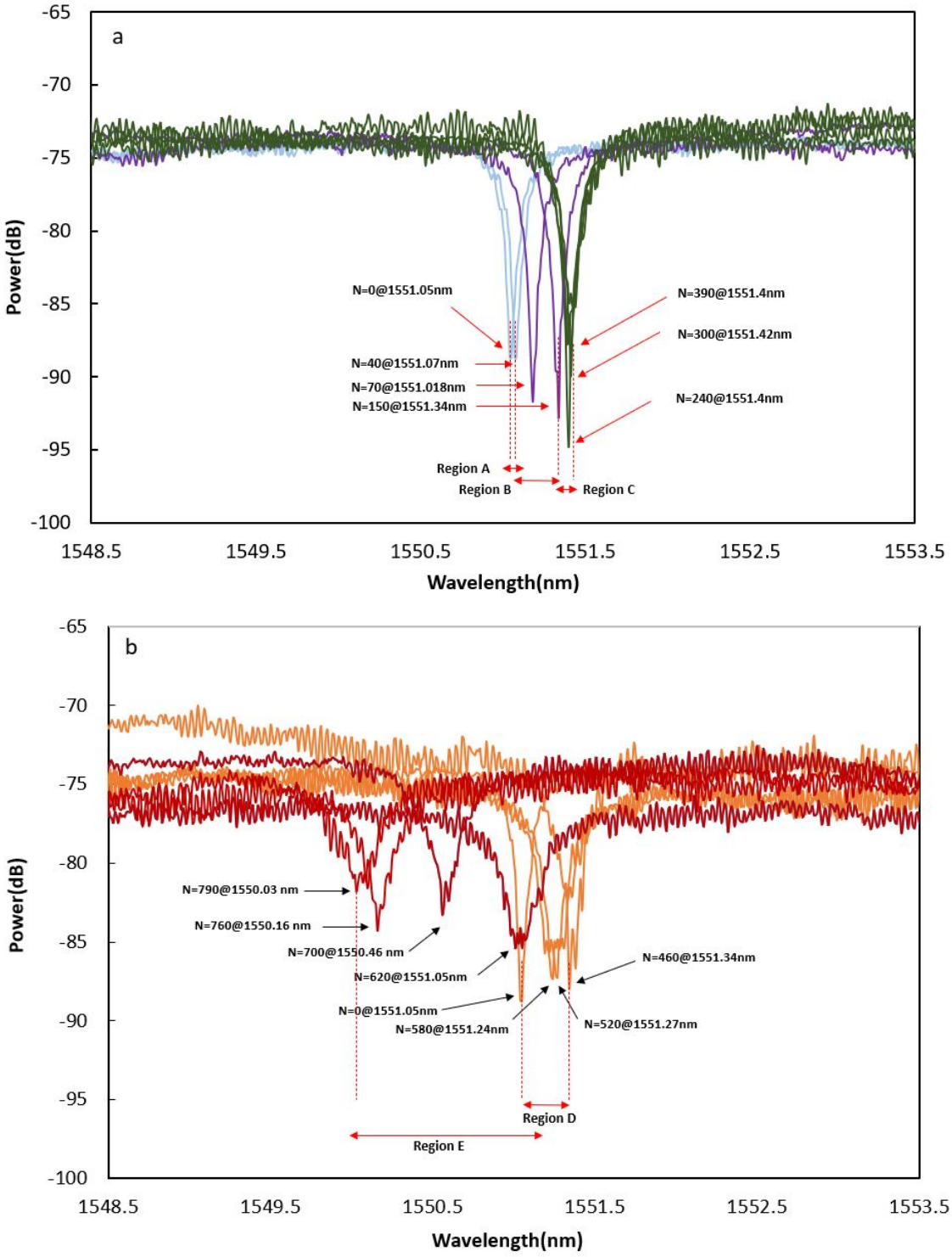

Figure 6.5: Spectrum of the accumulated resonance wavelength shifts corresponding to different pulse numbers at a fluence of $0.0232 J/cm^2$. (a) Pulse numbers range from N=0 to N=390. (b) Pulse Numbers range from N=390 to N=790.

in Fig.6.6. For N = 1 to 40 (Region A), no significant resonance wavelength shifts are observed. A value of approximately zero can be used to represent the shifts in region A. For N = 40 to 150 (Region B), constant positive shifts are observed and a linear relation with positive slope can be used to represent the shifts in this region. For N = 150 to 390 (Region C), very small constant positive shifts are observed, and a linear relation with a very small positive slope can be used to represent the shifts in this region. For N = 390 to 600 (Region D), constant negative shifts are observed, and a linear relation with a negative slope can be used to represent the shifts in this region. For N = 600 to 790 (Region E), larger constant negative shifts are observed, and a linear relation with a larger negative slope can be used to represent the shifts in this region. Equations representing the data for regions A to E are summarized in Table 6.1. The equations for regions B to E are given by the linear regression fit of the data. The tuning precision is given by the slope of the linear relation, and the uncertainty is given by the standard error of the linear regression fit of the data.

Table 6.1: Equations representing the data for regions A to E in Fig. 6.6

Region	**N**	**Equation** $\Delta\lambda$ is the induced resonance wavelength shift after irradiated by N shots	**Tuning Precision (pm/shot)**
A	1 - 40	$\Delta\lambda = 0$	
B	40 - 150	$\Delta\lambda = 0.002232N - 0.0627$	2.232 ± 0.152
C	150 - 390	$\Delta\lambda = 0.000137N - 0.244714$	0.137 ± 0.031
D	150 - 390	$\Delta\lambda = -0.00067N + 0.537224$	0.67 ± 0.06
E	600-760	$\Delta\lambda = -0.00495N + 3.038147$	4.95 ± 0.148

Measurement of the averaged roundtrip losses in the waveguide of the SiMRR after each shot is shown in Fig. 6.7. The total roundtrip losses are below 0.45 dB in posituve and negative shift regimes. The roundtrip losses increase slowly from 0.08

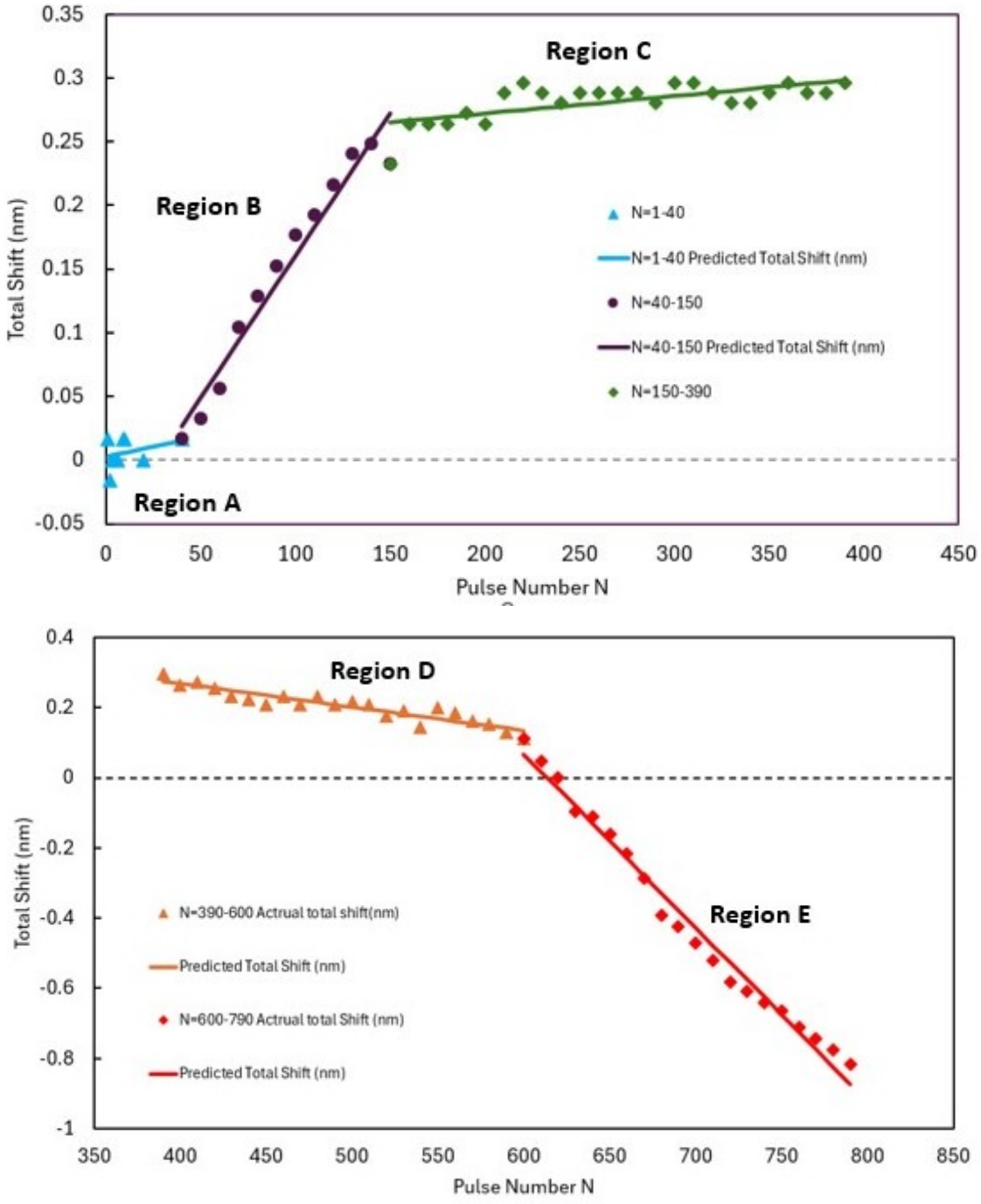

Figure 6.6: Example of the accumulated resonance wavelength shifts corresponding to different pulse numbers at a fluence of $0.0232 J/cm^2$. (a) The accumulated shift for N=1 to N=390.(b) The accumulated shift for N=390 to N=790.

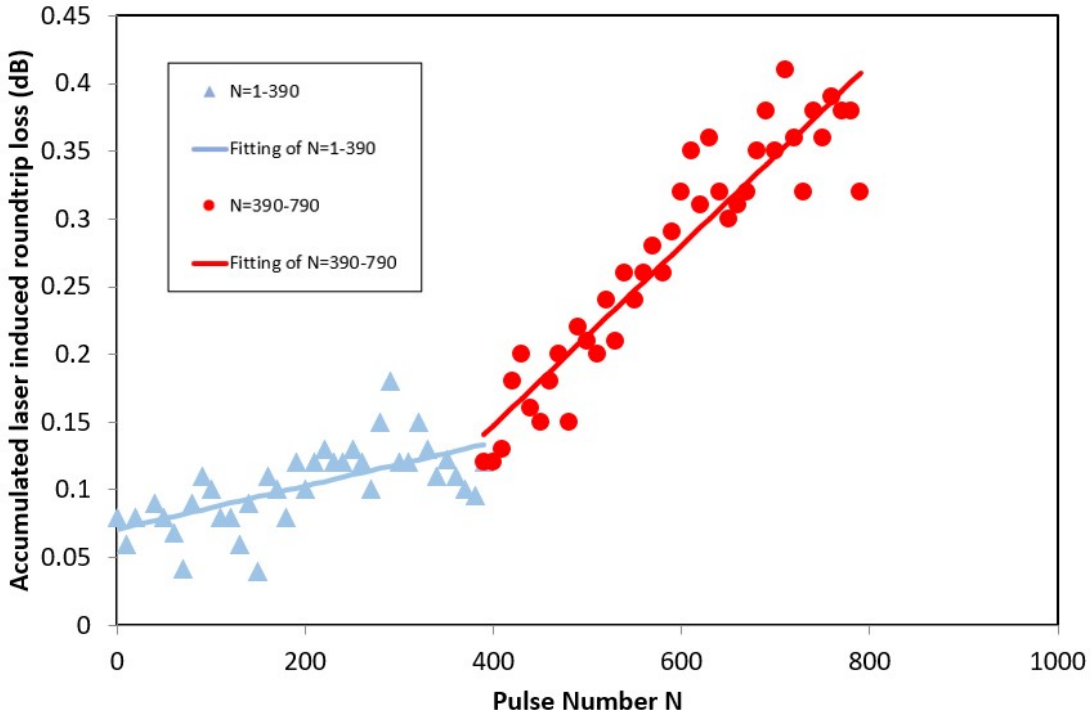

Figure 6.7: Induced roundtrip loss of microring resonators as a function of laser pulse number irradiated at a fluence of $0.0232 J/cm^2$.

dB to approximately 0.15 dB from N = 0 (unirradiated case) to N = 390, and a linear relation with a positive slope can represent the data. Beyond N = 390, the roundtrip losses increase rapidly to approximately 0.45 dB at N = 790. A linear relation with a larger positive slope can represent the data for N = 390 - 790. Equations representing the data for Fig. 6.7 are summarized in Table 6.2. The linear regression fit of the data gives the equations. The slope of the linear relation gives the induced loss per shot, and the standard error of the linear regression fit of the data gives the uncertainty.

Similar trends can be achieved at different energy fluences. As shown In Fig. 6.8, the chosen energy fluence ranges from $0.0232 J/cm^2$ to $0.0555 J/cm^2$, respectively. It clearly indicated that it is easier to achieve the desired positive shift value with smaller applied laser pulse numbers as the laser fluence increases. The maximum total accumulated resonance wavelength shift increases with increasing laser fluences. For instance, the maximum accumulated resonance wavelength shift is 1.2 nm at

Table 6.2: Equations representing the data for regions A to E in Fig. 6.7

Region	**N**	**Equation** RTL is the roundtrip loss after irradiated by N shots	**Induced roundtrip loss per shot**(dB)
A - C	1 - 390	RTL = 0.000161N + 0.070746	0.000161 ± 0.000032
D - E	390 - 790	RTL = 0.000667N – 0.11967	0.000667 ± 0.000040

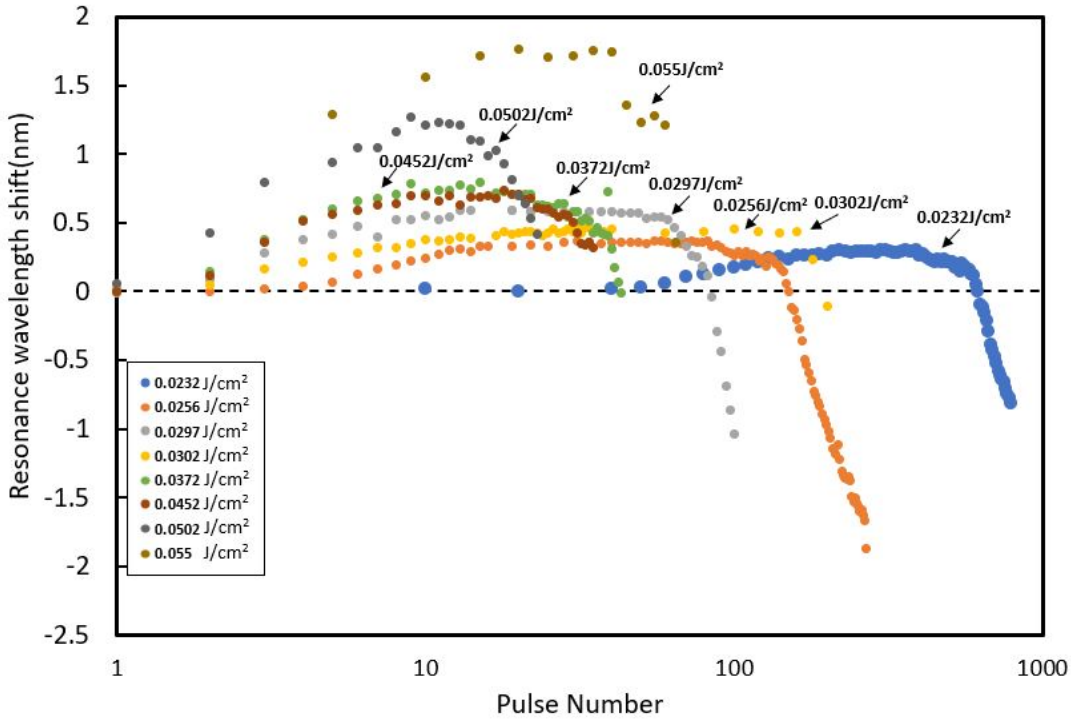

Figure 6.8: Resonance wavelength shifts of the resonators after each laser pulse irradiation at a fluence from $0.0232 J/cm^2$ to $0.0502 J/cm^2$.

$0.0502 J/cm^2$, which is 4 x larger than that of $0.0232 J/cm^2$ (Fig. 6.8). Higher fluences can obtain the desired value of the resonance wavelength shift by reducing the number of shots but sacrificing tuning resolution. By comparing the plots of accumulated shifts at similar fluences, it indicated that the tuning results can be varied. The repeatability of the tuning results is due to the different conditions during experiments including pulse to pulse energy fluctuation, accuracy of laser beam location on the resonator and so on. However, since the shot-to-shot tuning platform provides the capability of monitoring the resonant wavelength right after each laser shot, the precision of tuning can still be well maintained and eliminate the effect from various uncertainties. For example, in a real application case, if we aimed at getting specific resonant shift using a laser fluence of $0.03 J/cm^2$, the process can follow one of the three curves in Fig 6.8 with fluences of $0.0279 J/cm^2$, $0.0302 J/cm^2$ and $0.0308 J/cm^2$ and with shift per step of 36.09 $/pm$ 7.15 pm, 17.32 $/pm$ 2.19 pm, or 22.00 $/pm$ 4.20 pm, respectively. We are able to achieve the desired resonant wavelength shift with reasonable precision since the tuning precision will be governed by the shift per step of the curve it follows. . The induced roundtrip loss for a given induced resonance wavelength shift is not very sensitive to the fluence used. For example, to achieve a shift of 0.25 nm, if a laser fluence of $0.0232 J/cm^2$ is used, it will need N = 150 and will result in a roundtrip loss of 0.1 dB; but, if a laser fluence of $0.0502 J/cm^2$ is used, it will need N = 2 and will result in a similar roundtrip loss of 0.1 dB. More of the plots of the tuning curve and roundtrip loss and tables of coefficients for the linear fits of the tuning curve and roundtrip loss at different energy fluences are provided in Appendix B.

6.4 Conclusion

A laser tuning platform was developed to demonstrate precision permanent tuning of silicon photonic devices. The platform consists of an irradiation system utilizing NIR fs laser pulses, allowing the resonance wavelength of the Si photonic device to be

tuned to the desired value, a characterization system utilizing a super luminescence emitting diode (SLED), and an optical spectrum analyzer (OSA), allowing rapid characterization of the shot-to-shot tuning response of a silicon photonic device. Precision permanent tuning of SiMRR was demonstrated through a multi-shot approach using 50 fs laser pulses at 800 nm wavelength with sub-microjoule pulse energies. Positive and negative resonance wavelength shifts can be achieved with reasonable induced waveguide losses. Unprecedented fine-tuning of the microring resonance wavelength at a resolution of $\sim$ 2.2 pm per laser shot was achieved at a low laser fluence of $0.0232 J/cm^2$. The method also indicated pretty stable measurement, as measured performed on the same device over two months shows the almost same results($\pm$ 0.02nm). The tuning is stable. Measurments performed on the same tuned device over two monthes shows almost the same resonance frequency with an error bar within $\pm$ 0.02nm.

Chapter 7

Laser modification thresholds and dynamics of incubation effects

7.1 Introduction

As discussed in Chapter 2, the two key laser irradiation thresholds, melting and ablation, are defined as the energy fluences required to cause melting and material removal, respectively. Generally speaking, the different techniques for achieving the irradiation threshold can be cataloged into two main subjects: The ex-situ method, where the threshold is extracted from the measurement dimension of the melting or ablated area, and the in-situ technique for direct detection of signs of surface modifications.

The ex-situ method is the most commonly used for observing the material modification threshold, as it just requires a simple experimental setup and a straightforward measurement procedure. Two techniques are often applied: the diameter regression method by Liu et al.[33] called the Gaussian Beam Limiting Technique (GBLT), the D-square method or Liu's method, and the diagonal scan technique proposed by Samad et al. [79]. As already described in Chapter 2, in Liu's method, the beam radius of the laser spot can be determined by the curve fitting of the squared crater diameters versus the laser energy fluence, and the irradiation fluence can be obtained by extrapolating the same curve fitting to the zero limit of the crater diameter. In the diagonal scan technique, the sample is first placed above the focal point of the

incident laser beam. The sample is then translated simultaneously along the y and z directions and passes through the focal point of the beam path, leaving a feature of a" two slope shape" in the ablated region. The ablation threshold, F_{th}, is calculated from the measured dimension of the maximum radius on the ablation feature according to equation 7.1

$$F_{\text{th}} = \frac{E_0}{e\pi\rho_{\text{max}}^2} \tag{7.1}$$

where E_0 is the irradiated laser energy, ρ_{max} is the maximum damage radius typically measured in micrometer. Although the diagonal scan method is faster and easier and does not require parameters such as beam waist, Liu's method is more commonly used, as it usually provides a more consistent value between different reports in the literature.

In-situ methods allow for the direct determination of the modification threshold of sample material during the experiment without further measuring the morphology of the damaged area by external instruments. These methods include techniques such as collecting and detecting emitting ions or plasma [80], measuring index refraction changes on the irradiated surface using interference [81, 82], and measuring the corresponding resonance shift on photonic devices [5, 58], among others. Although some of these techniques offer high sensitivity for threshold measurement, they often require detectors with ultra-high detection capability. They may require experiments to be conducted in a vacuum chamber, which increases the complexity of the experimental setup.

The multiple-shot ablation thresholds are important parameters for studying the incubation effect. Most of the reported studies use the ex-situ method, where the fluence applied is higher than the single-shot ablation threshold, and the multishot thresholds are determined similarly to the single-shot cases. Only limited research has been carried out in the regime with fluences significantly below the single-shot ablation threshold regime

There is no clear consensus on the exact definition of modification thresholds, melting, damage, and ablation, one of them would be used in the literature when visual damage is observed. Additionally, there are various methods of measurement, each with different detection limits. Experimental setups, laser beams, and material parameters like chemical composition and surface state vary extensively. As a result, there is a significant variability in threshold values, making it challenging to compare experimental results. The precise and reliable determination of material thresholds is crucial for fundamental and application breakthroughs.

The previous study[2, 4] on using SiMRR to study modification thresholds in silicon by femtosecond laser pulses with 400 nm and 800 nm shows that SiMRR is a powerful tool for such investigation. The SiMRR method takes advantage of the device's ability to sense very small refractive index changes. The SiMRR method can detect refractive index change when there is no detectable visual change in the material, making it an ideal tool for studying the evolution of incubation effects. This chapter will investigate the modification threshold and incubation effect for femtosecond laser pulses at 800nm wavelength. We will also discuss the differences between 400 nm and 800nm wavelengths in the incubation phenomenon.

7.2 Modification thresholds

According to the behaviour of resonance wavelength shift on SiMRR, we can classify thresholds into two regions: positive resonance wavelength shift threshold (shortened as positive-threshold) and negative resonance wavelength shift threshold (shortened as negative-threshold). In previous studies, the negative threshold is often referred to as the ablation threshold, signifying surface material removal. The positive threshold is regarded as the threshold for melting, amorphization or re-crystallization, crystalline modifications such as defect formation, lattice distortion and dislocation, etc.

Here, we first summarize irradiation threshold values from previous literature and

compare them to our results. One data group is the set of measurements of single-shot ablation thresholds with Liu's diameter regression method and laser fluences above the single-shot ablation threshold. An amorphization threshold of 0.16-0.22J/cm^2 and an ablation threshold of 0.18-0.4J/cm^2 are commonly observed in the literature. In Chapter 4, we applied Liu's method on bulk silicon samples and found an ablation threshold of ($0.34J/cm^2$) consistent with values reported in the literature. The average value for ablation thresholds determined by Liu's method for pulse durations in the range between 100 – 200 fs is $0.33J/cm^2$ from the literature reported in Table 2.1 of Chapter 2. For the 250 nm silicon thin film on the SOI sample, we found a lower ablation threshold of $0.19J/cm^2$. The dependency of thin film thickness on damage thresholds has been reported in the literature [83, 84].

Modification thresholds are measured using in-situ measurement methods. For single shot thresholds at the irradiation laser wavelength of 800nm, Bachman et al.[3] reported a threshold of $0.18J/cm^2$ for a negative shift where ablation starts to occur and a threshold of $0.054J/cm^2$ for a positive shift. The results in the experiments reported in Chapter 6 observed a positive shift of 0.2nm at a fluence of $0.052J/cm^2$, which agrees well with the reported value by Bachman et al. [3]. In both studies, visual damage was not observed, and no sign of amorphization of the silicon layer can be detected using SEM or Raman spectroscopy within the irradiated region. The threshold value is several times below the reported amorphization process, which is not responsible for the observed refractive index changes threshold.

In the study of the incubation effect of silicon due to multiple femtosecond pulses, no study carried out with fluences significant below the single-shot ablation threshold was found.

For NIR irradiation, the literature and our experimental results clearly show a lowering of modification thresholds with increased pulse numbers (see Fig.7.1). Bonse et al.[7] and Nathala et al.[31] reported a similar incubation coefficient of 0.82 for bulk silicon samples. However, the thresholds they measured varied from each other,

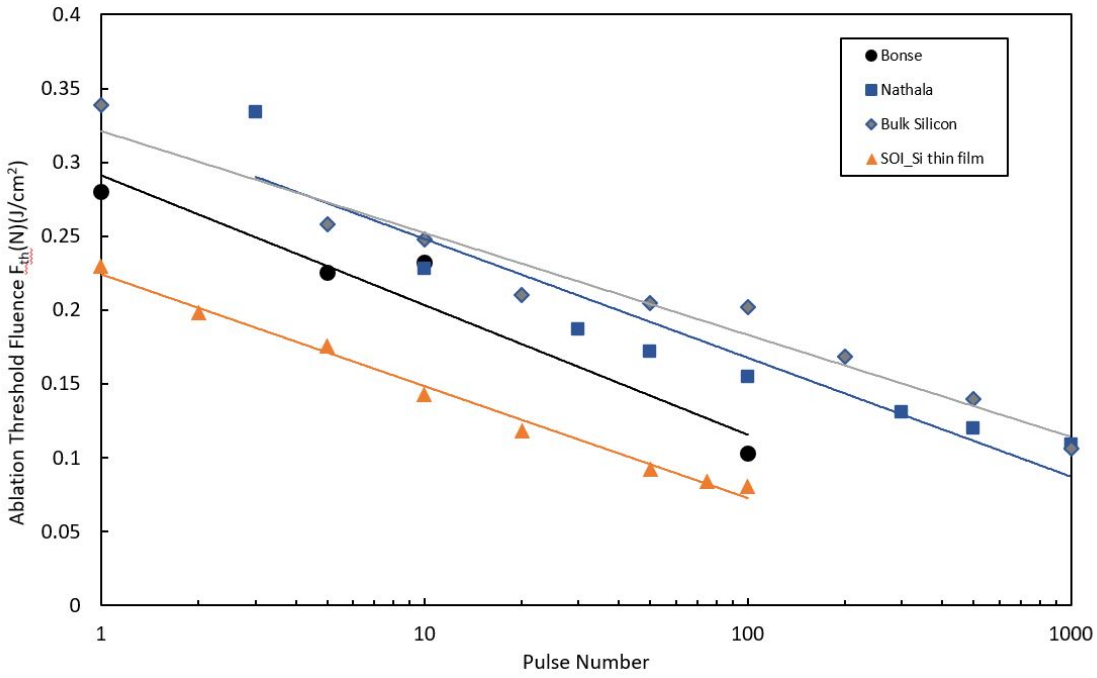

Figure 7.1: Measured ablation thresholds at different pulse numbers and the incubation effect for bulk silicon. The data include those extracted from Bonse et al. [7], and Nathala et al. [31], and our own results reported in Chapter 4. The fitting method is the basic incubation model presented in Chapter 4 as Eq. 7.1.

which may be due to the different conditions of the experiments conducted in air and vacuum, respectively. We have measured an incubation coefficient of 0.84 for bulk Si and thin-film Si (see Chapter 4), consistent with the reported values (0.82-0.84) in the literature. No study using visible fs laser pulses to study the incubation effect in Si was found. Our study (see Chapter 4) using 400 nm fs pulses discovered the incubation effect in Si is very weak, with a measured incubation coefficient of 0.94.

7.3 Study of the dynamics of incubation effects using SiMRR

We have used laser fluence significantly below the single-shot ablation threshold with energy fluence ranging from 0.0133-0.06J/cm^2 to study the dynamics of the incubation effects by using the SiMRR as a characterization tool. The SiMRR's resonance wavelength shift, $\Delta\lambda$, can be related to the refractive index change, Δn, by using the equation below:

$$\Delta \mathrm{n} = (\Delta\lambda/\lambda_0)\,(2\pi \mathrm{R}/\mathrm{l})\mathrm{n_g} \tag{7.2}$$

where λ_o is the unirradiated resonance wavelength (typically around 1552 nm) of the SiMRR, R is the radius of SiMRR (15 um), l is the length of the section of the waveguide being irradiated ($\sim$ 22 um length of damage region on the waveguided measured according to the SEM images), and n_g is the refractive index of the waveguide (2.3 for crystalline silicon). The accumulated refractive index change after irradiating the number of shots at various fluences is shown in Fig. 7.2. The curves show a similar profile consisting of a fast-rising front edge, a slow-rising region close to a constant plateau, a very slow-falling region and finally, a fast-falling rear edge. The accumulated refractive index change after the irradiation of each shot at a fluence of 0.0232J/cm^2 fluences is shown in Fig. 7.3. The various regions of the profile are labelled as A, B, C, D, and E (the labels used here are consistent with those used in

Chapter 6).

Region A (N = 1 - 40): no significant refractive index change was observed.

Region B ("fast-rising region," N = 40 - 150): The refractive index change versus N can be described by a linear relation with a slope of 1.13 x 10^5. In this region, we speculate that the amount of laser-induced dislocations and lattice distortions grows with increasing shot number, leading to an increase in the induced refraction index. However, no modifications of the surface can be detected by SEM.

Region C ("slow rising region", N = 150 - 390): the induced refractive index changes are approximately constant. The near-saturated induced refractive index change may be due to the generated dislocations and defects that completely fill the light absorption region. SEM still shows no evidence of surface modification.

Region D ("slow falling region, 390 - 600): the induced refractive index change is slowly decreasing with increasing shot number. A slight decrease in the induced refractive index may result from the removal of a small amount of silicon, i.e. nanomilling of the silicon. For the decrease of refractive index, the amount of Si removed is estimated to be 0.3 fg per pulse. The SEM image in Fig. 7.4 (a-c) indicated that at N = 500, the surface is slightly modified, with a channel with a width of $\sim$ 100 nm at the center of the irradiated waveguide. There are also a small number of $\sim$ 50 nm diameter "molten" droplets on the surface of the channel.

Region E ("fast falling region, 600 - 790): the induced refractive index change is rapidly decreasing with increasing shot number. The amount of Si removed is estimated to be 1.3 fg per pulse. The SEM image in Fig. 7.4(d-f) clearly indicates that at N = 790, a groove with a width of $\sim$ 100 nm is formed at the surface. The depth of the groove appears to be significant, and there are structures on the groove that are likely due to the ablation. At N = 790, the total amount of Si removed can be estimated at 310 fg. If we assume an ablation area of 0.1 um x 26 um, the depth of the grove can be estimated to be about 50 nm.

Both the channel at N = 500 and the groove at N = 790 are formed along

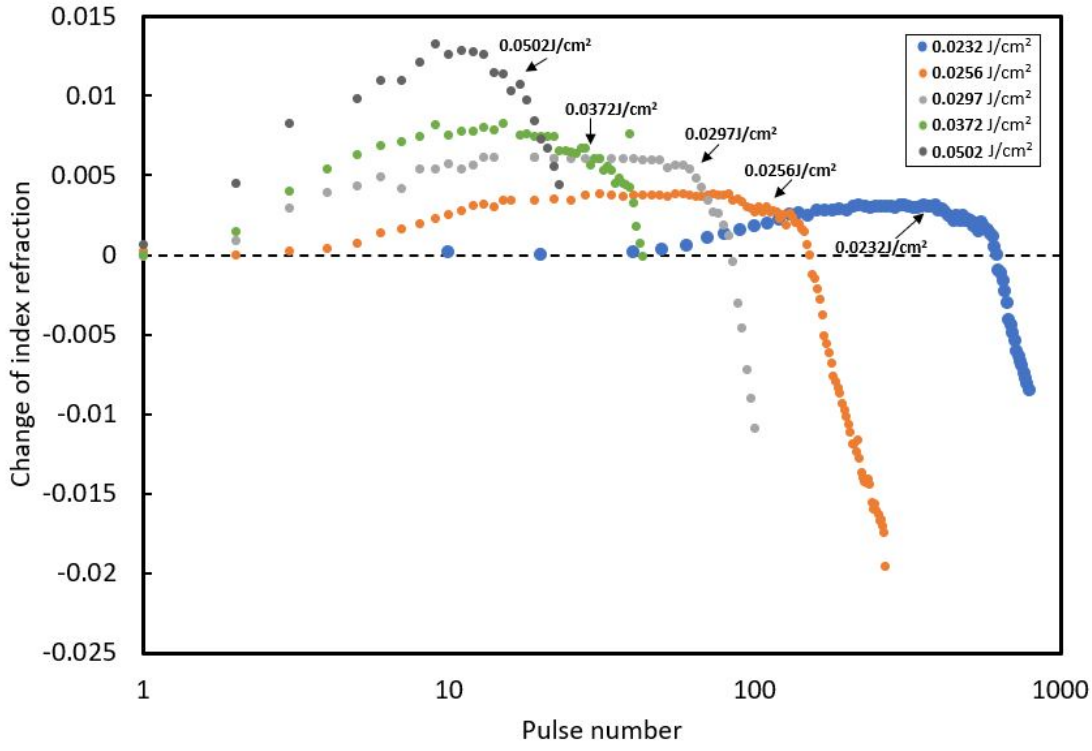

Figure 7.2: Accumulated change of the index refraction of the resonators after each laser pulse irradiation at a fluence from $0.0232 J/cm^2$ to $0.0502 J/cm^2$.

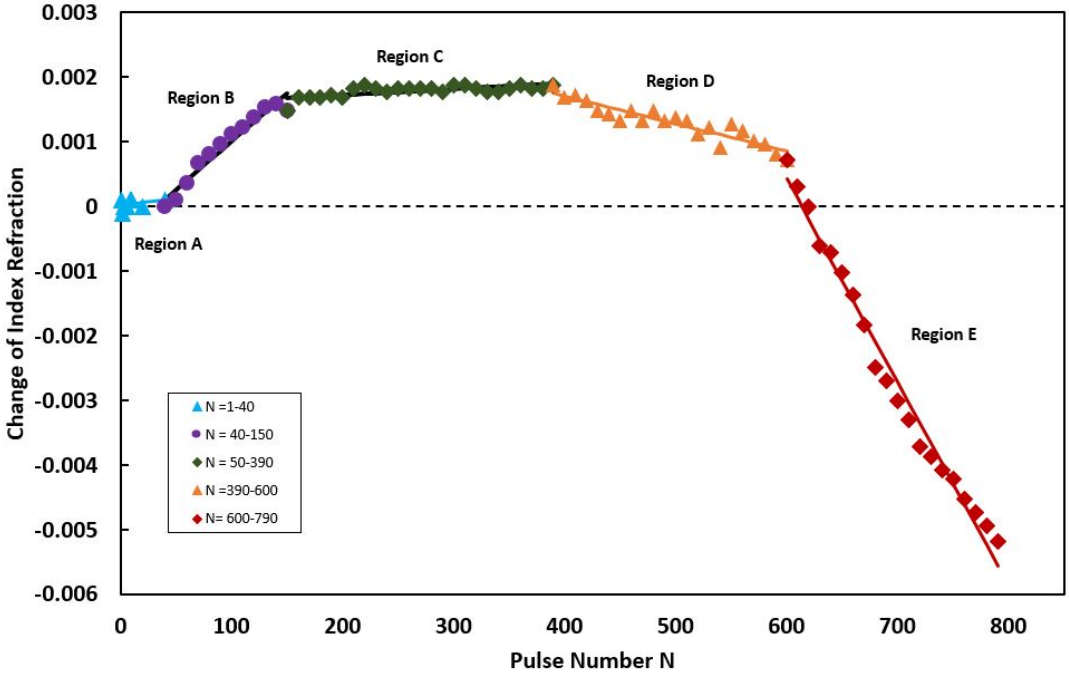

Figure 7.3: The accumulated laser-induced index refraction changes of the resonators after irradiation with each of the laser pulse irradiation at a fluence of $0.0232 J/cm^2$.

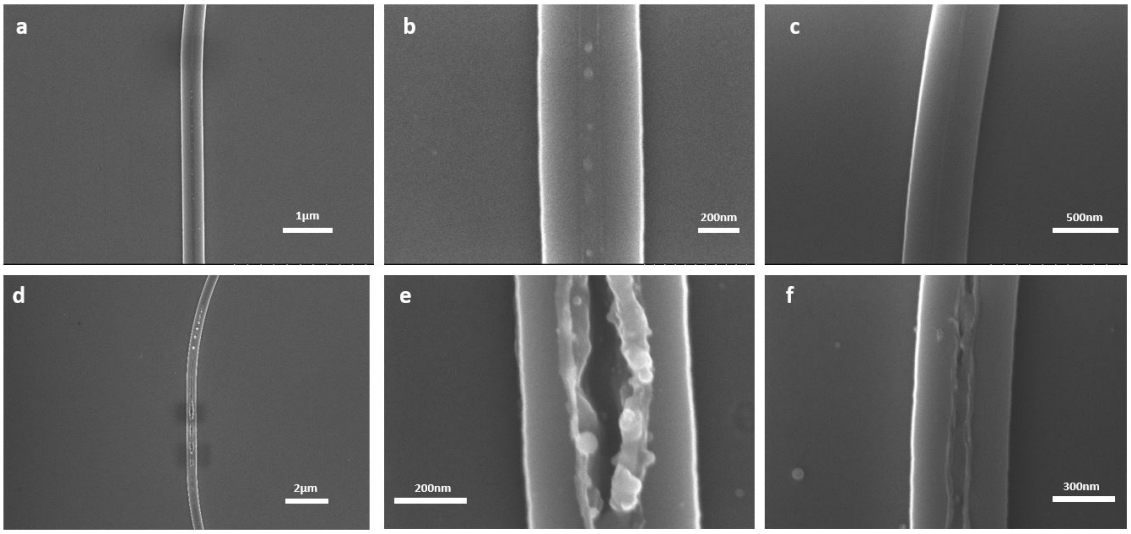

Figure 7.4: SEM image of the irradiated area with a fluence of $0.0232 J/cm^2$ at different pulse numbers. (a)N = 500. (b) and (c) are enlarged details of the irradiated region of N = 500. (d) N = 790. (e) and (f) are enlarged details of the irradiated region at N =790.

the center line of the waveguide, even at the curved corners. Note that the beam radius is 13.4 um while the waveguide is only 500 nm. When the center of the laser beam is aligned to the waveguide, the energy deposition on the waveguide should be almost constant. However, as seen in Fig.7.4, only the center part of the waveguide is modified, and the area on two sides of the waveguide appears unmodified. The observation may be a result of Fresnel diffraction., where the electric field is strongly enhanced at the center of the waveguide and may lead to the accumulation of defect and inner stress. However, the detailed mechanism is still unknown and requires further investigation.

Various pulse dependence thresholds at a given irradiated fluence can be defined by examining Fig. 7.2. They include: (i) the start of the positive refractive index change (or beginning of region B) at N = 40 that can be called "Defect Generation Threshold" or $F_{th}(40)_{DG} = 0.023J/cm2$, (ii) the start of negative refractive index change (or beginning of region D) at N = 390 that can be called "Nanomilling Threshold" or $F_{th}(390)_{NM} = 0.023J/cm^2$ and (iii) the start of large negative refractive index change (or beginning of region E) at N = 600 that can be called "Ablation Threshold" or $F_{th}(600)_{AB} = 0.023J/cm^2$. Various thresholds for different irradiated fluences can be extracted from the data presented in Fig.7.2 and are shown in Fig.7.5. In Fig. 7.6, the SiMRR "Ablation threshold" is compared to mult-shot ablation thresholds estimated using the Liu's and binary method in Chapter 4. The single shot ablation threshold of $0.17J/cm2$ from 250nm SOI result from Chapter 4 is used as the F_1 Value for negative-shift plot for SiMRR. The thresholds for the binary method using a bulk Si wafer sample are higher than the SiMRR thresholds. Still, the trend is consistent, giving a weaker incubation effect than the data obtained by applying laser pulses with fluences above the single shot ablation threshold.

The multi-shot ablation threshold curve obtained by fluences measured using Liu's method with fluences above the single-shot ablation threshold resulted in a stronger incubation effect than those obtained by fluences significantly below the

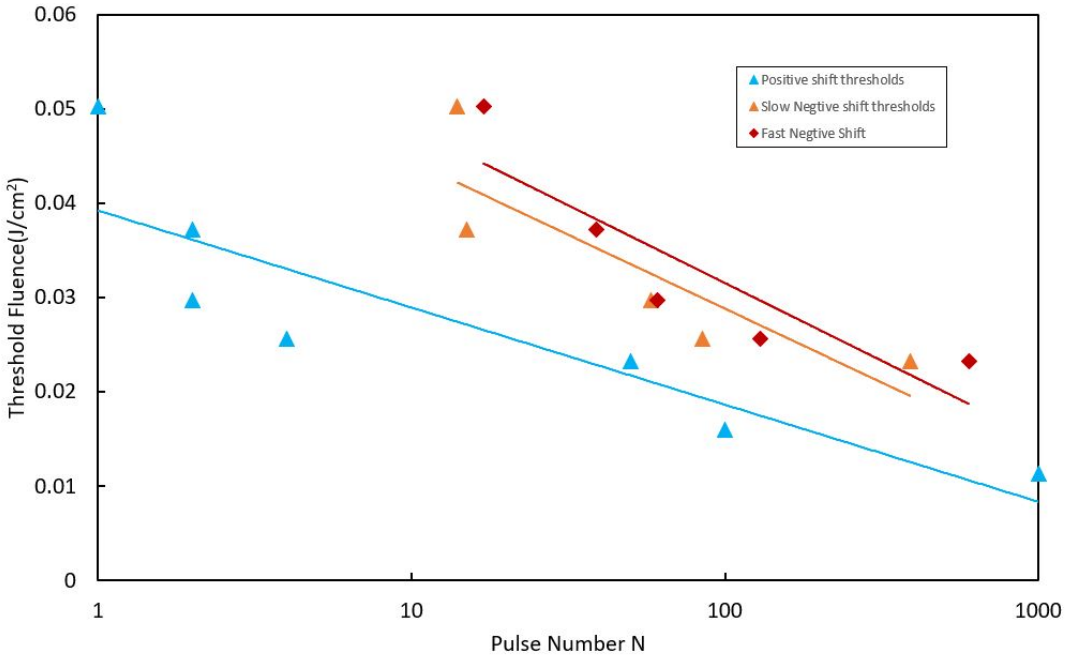

Figure 7.5: Different threshold fluences extracted from the accumulated change of the index refraction of the resonators after each laser pulse irradiation at a fluence from $0.0232 J/cm^2$ to $0.0502 J/cm^2$

single-shot ablation threshold such as the binary method (see Chapter 4) and the SiMRR technique. In the literature [7, 31], it was pointed out that the major contribution of the incubation effect measured above the single-shot threshold may be from the formation of surface features such as laser-induced Periodic Surface Structures (LIPSS), microholes, or melting regions. These features may cause non-uniform distribution of laser energy, diffraction, or absorption coefficient change at localized regions. In our case, these phenomena would not contribute to the observed incubation effect because of the much lower fluences used. Thus, our approach truly measures the incubation effect in the sub-single shot damage regime.

7.3.1 Comparison of incubation effect behaviour for 400 nm and 800 nm irradiation

A previous study [58] has measured the single-shot refractive index change threshold (positive threshold) for SiMRR irradiated by femtosecond laser pulses with wave-

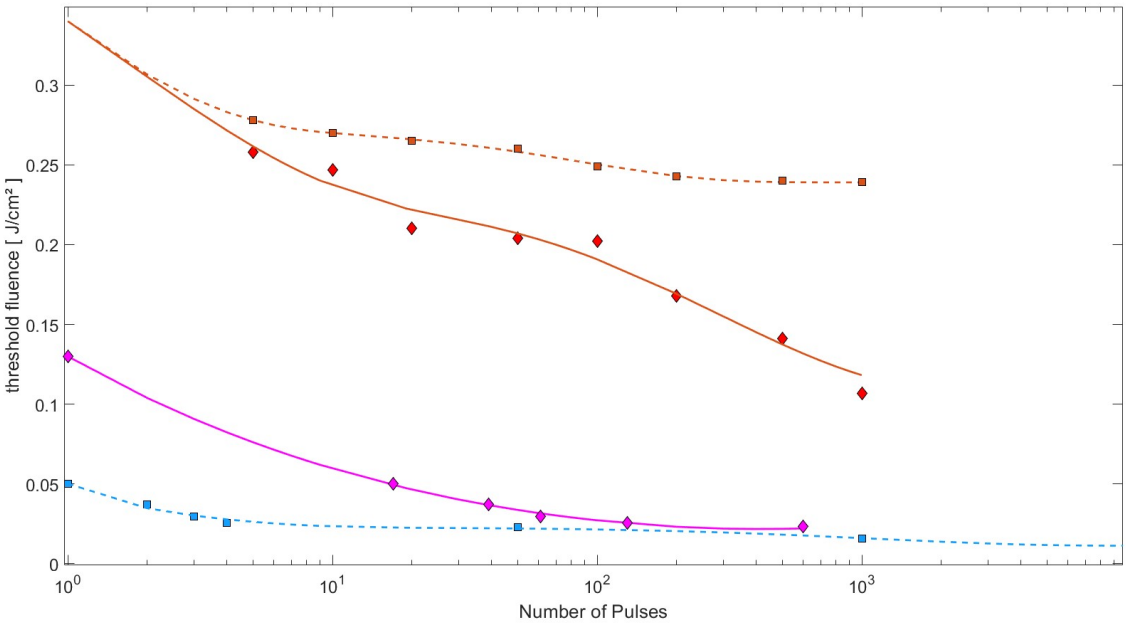

Figure 7.6: Ablation thresholds, $F_{th}(N)$, as a function of N for bulk silicon sample (in red) and SiMRR thresholds (in blue). The red squares and dashed lines represent extracted ablation thresholds and fittings from squared crater diameter to fluence, and the red rhombus and solid lines represent the data from the sub-threshold binary method. The blue squares and dashed lines show the positive-shift threshold extracted from the SiMRR and its fitting using generic incubation model, while the blue rhombus and solid lines represent the data for the negative-shift threshold and its fitting using generic incubation model from the SiMRR, respectively.

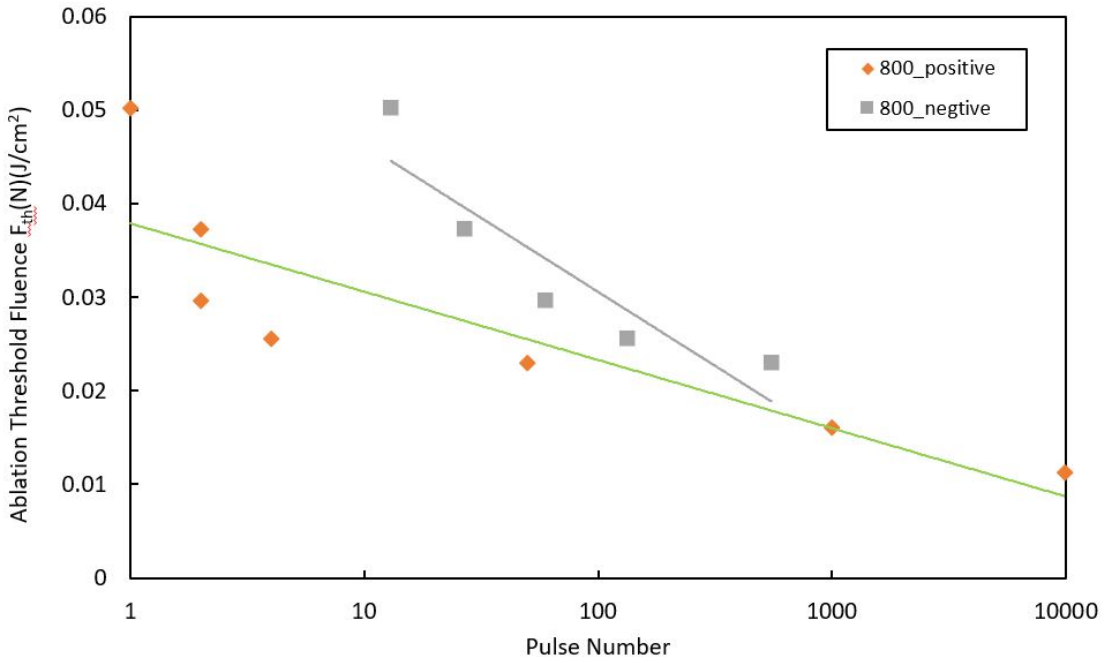

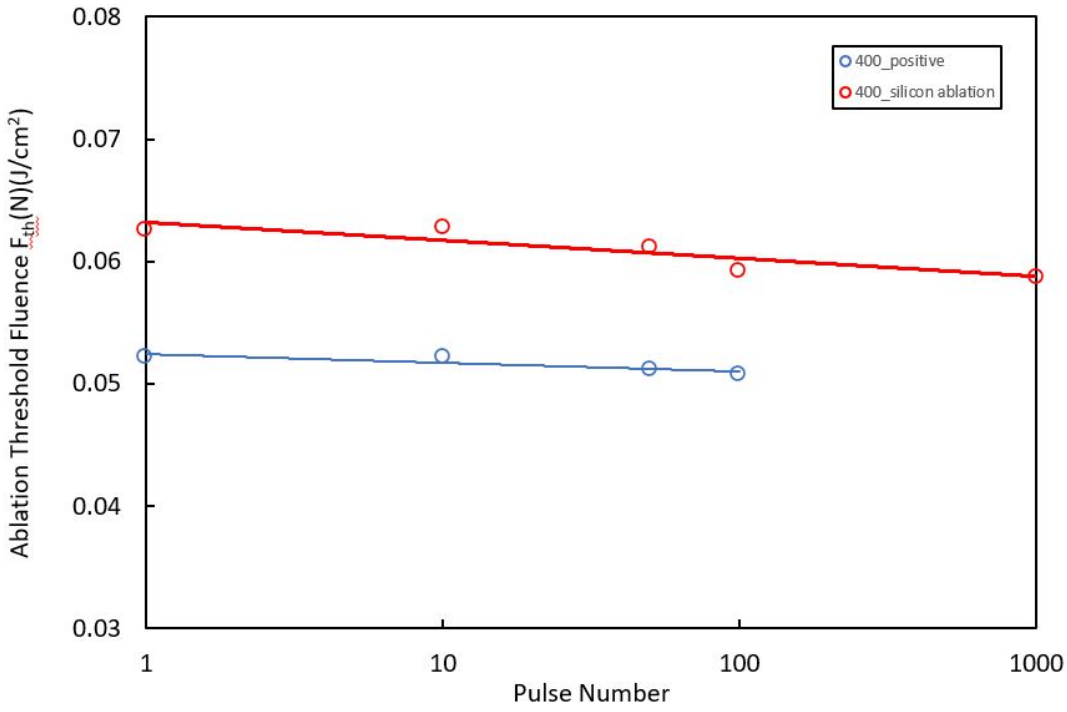

Figure 7.7: Threshold and incubation effect for 400 nm and 800 nm cases measured from SiMRR.(a) Measurement of 800 nm wavelengths for the positive-shift threshold(red) and negative-shift threshold(blue), respectively. (b) Measurement of 400 nm wavelengths for the positive-shift threshold(blue) and ablation threshold extracted from above threshold laser irradiation experiments using bulk Si as described in Chapter 4, Section 3.2.2 (red), respectively.

lengths of 400 nm or 800 nm, respectively. A resonance wavelength shift of 0.2 nm on SiMRR was measured when irradiated by a single femtosecond laser pulse with a wavelength of 400 nm at a fluence of $0.053 \pm 0.007 J/cm^2$. Thus, the fluence value is the single-shot refractive index change for 400 nm wavelength. This was accompanied by a visible change in the reflectivity of the irradiated area at the surface because of the difference in refractive index between crystalline and amorphous silicon. The value agreed with the other reported values for the melting threshold of $0.06 J/cm^2$[85]. The single-shot positive threshold for the irradiation wavelength of 800 nm was observed at 0.044 ± 0.005 J/cm^2, which is almost 5 x smaller than the other reported values ($0.2 J/cm^2$-$0.27 J/cm^2$) for damage threshold. For 800 nm laser pulse irradiation, the refractive index change threshold occurs at a fluence far below the melting threshold. We have discovered there is a significant difference in the behaviour of the incubation effect between irradiation wavelengths of 400 nm and 800 nm. As discussed before, a significant strong incubation effect with an incubation coefficient of 0.84 was observed for 800 nm irradiation; however, the incubation effect for 400 nm irradiation was observed to be weak.

As described in Chapter 4, section 3.2, for 400 nm pulses at a fluence slightly below the melting threshold at $0.528 J/cm^2$, no change of colour on the silicon surface can be detected when irradiated with 100 pulses. The measured single-shot ablation threshold and incubation coefficient were determined to be $0.0656 J/cm^2$ and 0.94, respectively. The close to unity of the incubation coefficient indicates a weak incubation effect for 400 nm wavelength laser irradiation. The measurement of resonance wavelength tuning on our real-time characterization system indicated a similar trend for 400 nm laser irradiation (see Fig.7.7). The first positive shift by single shot was observed for 0.1 nm at 0.0522 J/cm^2, while for N =100, the first positive shift was achieved at $0.0508 J/cm^2$, showing a weak incubation effect.

The large difference in the incubation effect for 400 nm and 800 nm may result from different absorption mechanisms of the two cases: linear absorption for 400 nm

and two-photon absorption dominated for 800 nm.

7.4 Conclusion

The SiMRR is an effective tool for detecting refractive index change in a material even when there is no visible change, making it an ideal tool for studying the shot-to-shot evolution of incubation effects. The newly defined mult-shot defect generation, nano-milling and ablation thresholds were estimated from the SiMRR data. The SiMRR results also confirm that the incubation effect is weak for the Si under 400 nm irradiation. The investigation revealed that the conventional approach of using fluences above the single-shot ablation threshold to study the incubation effect could not be used to describe the behaviour of the incubation effect for Si with irradiation fluences significantly below the single-shot melting threshold.

Chapter 8

Summary and Future Work

8.1 Key contributions in the thesis

8.1.1 Multi-pulse ablation threshold and Incubation effect in sub-threshold region (chapter 4)

The multi-shot ablation thresholds for polycrystalline copper and single crystalline silicon wafer with irradiation fluences above ($F > F_1$) and below ($F < F_1$) the single shot threshold (F_1) were investigated. A near-infrared femtosecond laser, with a wavelength of 800 nm and pulse duration of 130 fs, was used in the experiments. A comparison of the results for fitting two existing incubation models is performed to better understand the incubation effects. The first one (model 1) is the widely used simple power law, and the second one (model 2) includes the effects of absorption change and critical minimum fluence, F_∞. The key findings are:

(a) Copper:

$F_1 = 0.87 \pm 0.018 J/cm^2$ ($F > F_1$ case)

$F_\infty = 0.18 \pm 0.02 J/cm^2$ ($F < F_1$ case)

The coefficients for models 1 & 2 can be found in Table 4.1 of Chapter 4.

The coefficients for both models determining in the two fluence cases are consistent with each other.

(b) Silicon:

$F_1 = 0.34 \pm 0.043 J/cm^2$ ($F > F_1$ case)

$F_\infty = 0.21 \pm 0.026 J/cm^2$ ($F < F_1$ case)

The critical fluences, F_∞, for Cu and Si are new results.

The coefficients for models 1 & 2 can be found in Table 4.2 of Chapter 4.

Model 1 is not a good model to describe the low fluence ($F < F_1$ case) data. The coefficients for model 2 determined in the two fluence cases are significantly different from each other. The results indicate the need for further improvements of the incubation models by other effects, such as multi-photon absorption and silicon defect physics.

The multi-shot ablation thresholds for 250 nm Si thin film (commercial SOI or PECVD Si on Si wafer) were investigated with irradiation fluences above ($F > F_1$). A 130 femtosecond laser, with its fundamental wavelength of 800nm or its second harmonic wavelength of 400 nm, was used in the experiments. For 800 nm irradiation, the 250 nm Si thin film has a lower F_1 of $0.18 J/cm^2$. Its simple power law (model 1) incubation coefficient S is 0.84, which is the same as the bulk Si. For 400 nm irradiation, F_1 is determined to be 0.0656 J/cm^2, and S is 0.94. The closer to 1 incubation coefficient indicates that the incubation effects are weak.

The significant difference in behaviour of the incubation effect for Si between 800 nm and 400 nm irradiation is reported for the first time.

8.1.2 Demonstration of multi-shot femtosecond laser tuning (Chapter 5)

Based on the incubation effect, the multi-shot femtosecond laser surface modification method as a permanent tuning technique for obtaining the desired resonance wavelengths for silicon microring resonators was demonstrated. In this multi-shot tuning approach, each microring resonator was irradiated with 10 or 100 laser pulses in the same location of the waveguide with selected laser fluence. The laser beam has 800 nm wavelength, 130 fs pulse duration, a quasi-Gaussian spatial profile with a beam waist radius of 13.4 µm, and pulse energies of 12 nJ to 186 nJ to generate the

applied range of laser fluences. The silicon microring resonators used in the study have a diameter of 15 µm and are coupled to a waveguide of 500 nm in width with a gap of 260 nm. The result was that multi-shot tuning curves (resonance wavelength shifts as a function of laser fluences) do not monotonically increase with laser fluences: they first increase, then plateau, and finally decrease. Because of the incubation effects, the laser energies required for the multi-shot case to obtain the onset of crystalline modifications and ablation are several times below the single-shot case. Positive and negative resonance wavelength shifts were demonstrated with acceptable induced roundtrip waveguide losses.

The multi-shot tuning approach is new, and it allows low-cost compact low energy laser systems to be used.

8.1.3 Demonstration of precision tuning of silicon microring resonators (Chapter 6)

An online characterization platform consisting of two sub-systems, (i) a femtosecond laser irradiation system and (ii) an improved fast optical characterization system for measuring resonance spectrum from a silicon photonic device, was developed. The platform can be used to achieve high-precision tuning. The femtosecond laser system used has a wavelength of 800 nm and a pulse duration of 50 fs. Applying the multi-shot tuning approach to tune SiMRR by using a fluence of $0.0232 J/cm^2$, an ultra-fine tuning resolution of 2.2 pm per shot with a relatively low accumulated roundtrip loss at about 0.1 dB was observed.

The ultrafine tuning resolution demonstrated is a new record for permanent tuning by fs laser techniques.

8.1.4 Laser modification thresholds and dynamics of incubation effect evolution (chapter 7)

The SiMRR is an effective tool for detecting refractive index change in a material even when there is no visible change, making it an ideal tool for studying the shot-

to-shot evolution of incubation effects. The multi-shot defect generation, nanomilling and ablation thresholds were estimated from the SiMRR data. The investigation revealed that the conventional approach of using fluences above the single-shot ablation threshold to study the incubation effect could not be used to describe the behaviour of the incubation effect for Si with irradiation fluences significantly below the single-shot melting threshold.

The study of the dynamics of the incubation effect of Si due to NIR and Violet laser pulses with fluences significantly below the single shot ablation threshold was not reported previously.

8.2 Proposed future work

In the thesis, a precision tuning platform consisting of an irradiation system and a characterization system was developed. The platform allows detailed shot-to-shot response to the tuning laser pulse from a silicon photonic device. An ultrafine resolution of a few pm per shot and a relatively low round trip loss was demonstrated based on a multi-shot approach using sub-microjoule 50 fs and 800 nm pulses. The platform was also used to study the incubation effect dynamics of multi-shot irradiation of silicon at low fluences well below thresholds where material modifications can be detected by common surface characterization methods. Several research and development tasks can be conducted to improve the platform further.

1. Research in better understand the wavelength and pulse duration scaling for the multi-shot tuning approach. These scaling are important for optimizing the approach and its further development as a potential commercial product. A low-cost, compact fibre fs laser system can be used to reduce the cost and improve the compactness of the laser tuning platform. The wavelengths of current fiber laser systems typically have wavelengths of longer than 1 um and pulse duration of several 100 fs, generating an output laser pulse energy level of tens of uJ.

2. Investgate methods to make the tuning performing-user-friendly for its further

development as a potential commercial product. Currently, highly skilled operators are needed to operate the platform. The mounting, alignment, and coupling of the lensed fibres to the edge coupler of the silicon waveguide are done manually. Improvement in the automation of the motion stages with fully controllable and programmable ones and use of ML/AL methods of fully automatic tuning.

3. Due to the local fluctuations in the microchip's environment, silicon PICs' thermal tuning may be unavoidable even with permanent tuning. Therefore, research efforts may be needed to develop a hybrid approach based on a laser tuning system in conjunction with thermal tuning.

4. Nanosecond laser pulses can be added to the platform to recrystallize Si by reversing the defect or amorphous state induced by the fs laser pulses [86, 87]. This may lead to a new technique that allows back-and-forth tuning of the resonance wavelengths of a Si photonic device.

5. Fluorescence microscopy can be added to the platform. The fluorescence spectrum can be used for the identification of types of Si defects pulses [86] in laser irradiation region. This will provide additional information for a better understanding of the incubation effect of laser-irradiated silicon.

6. The incubation effect dynamic characterization method can potentially be extended to other materials. SiN, GaN, fused silica, etc. [88] which are used for making microring resonators. For example, the study of the evolution of damage mechanisms in fused silica is important for many high-intensity laser applications, including inertial fusion energy [89].

Bibliography

[1] S. Kirkwood, M. Taschuk, Y. Tsui, and R Fedosejevs, "Nanomilling surfaces using near-threshold femtosecond laser pulses," in *Journal of Physics: Conference Series*, IOP Publishing, vol. 59, 2007, p. 126.

[2] D. Bachman, Z. Chen, R. Fedosejevs, Y. Y. Tsui, and V. Van, "Permanent fine tuning of silicon microring devices by femtosecond laser surface amorphization and ablation," *Optics express*, vol. 21, no. 9, pp. 11 048–11 056, 2013.

[3] D. Bachman *et al.*, "Permanent phase correction in a polarization diversity si pic by femtosecond laser pulses," *IEEE Photonics Technology Letters*, vol. 27, no. 17, pp. 1880–1883, 2015.

[4] D. Bachman, Z. Chen, R. Fedosejevs, Y. Tsui, and V. Van, "Very fine refractive index tuning of silicon by single femtosecond laser pulses below melting threshold," in *CLEO: Science and Innovations*, Optica Publishing Group, 2017, STh4J–5.

[5] D. Bachman, Z. Chen, C. Wang, R. Fedosejevs, Y. Y. Tsui, and V. Van, "Post-fabrication phase error correction of silicon photonic circuits by single femtosecond laser pulses," *Journal of Lightwave Technology*, vol. 35, no. 4, pp. 588–595, 2017.

[6] J. Bonse, K.-W. Brzezinka, and A. Meixner, "Modifying single-crystalline silicon by femtosecond laser pulses: An analysis by micro raman spectroscopy, scanning laser microscopy and atomic force microscopy," *Applied surface science*, vol. 221, no. 1-4, pp. 215–230, 2004.

[7] J. Bonse, S. Baudach, J. Krüger, W. Kautek, and M. Lenzner, "Femtosecond laser ablation of silicon–modification thresholds and morphology," *Applied Physics A*, vol. 74, pp. 19–25, 2002.

[8] A. Rousse *et al.*, "Non-thermal melting in semiconductors measured at femtosecond resolution," *Nature*, vol. 410, no. 6824, pp. 65–68, 2001.

[9] D. Korfiatis, K. T. Thoma, and J. Vardaxoglou, "Conditions for femtosecond laser melting of silicon," *Journal of Physics D: Applied Physics*, vol. 40, no. 21, p. 6803, 2007.

[10] J Bonse, "All-optical characterization of single femtosecond laser-pulse-induced amorphization in silicon," *Applied Physics A*, vol. 84, pp. 63–66, 2006.

[11] M. Fujita, Y. Izawa, M. Hashida, Y. Setsuhara, Y. Izawa, and C. Yamanaka, "Ultrafast phase transition of si by femtosecond laser pulse irradiation," vol. 6346, pp. 1044–1050, 2007.

[12] D. Wan, J. Wang, and P. Mathew, "Energy deposition and non-thermal ablation in femtosecond laser grooving of silicon," *Machining science and technology*, vol. 15, no. 3, pp. 263–283, 2011.

[13] H. Vaghasiya, S. Krause, and P.-T. Miclea, "Thermal and non-thermal ablation mechanisms in crystalline silicon by femtosecond laser pulses: Classical approach of the carrier density two temperature model," *Journal of Physics D: Applied Physics*, vol. 55, no. 17, p. 175 109, 2022.

[14] A Borowiec, M Mackenzie, G. Weatherly, and H. Haugen, "Transmission and scanning electron microscopy studies of single femtosecond-laser-pulse ablation of silicon," *Applied Physics A*, vol. 76, pp. 201–207, 2003.

[15] D. J. Hwang, C. P. Grigoropoulos, and T. Y. Choi, "Efficiency of silicon micromachining by femtosecond laser pulses in ambient air," *Journal of applied physics*, vol. 99, no. 8, 2006.

[16] S. Lee, D. Yang, and S. Nikumb, "Femtosecond laser micromilling of si wafers," *Applied Surface Science*, vol. 254, no. 10, pp. 2996–3005, 2008.

[17] H. Li and H. Ki, "Effect of ionization on femtosecond laser pulse interaction with silicon," *Journal of applied physics*, vol. 100, no. 10, 2006.

[18] D. Korfiatis, K.-A. T. Thoma, and J. Vardaxoglou, "Numerical modeling of ultrashort-pulse laser ablation of silicon," *Applied Surface Science*, vol. 255, no. 17, pp. 7605–7609, 2009.

[19] S Guizard, A Semerok, J Gaudin, M Hashida, P Martin, and F Quéré, "Femtosecond laser ablation of transparent dielectrics: Measurement and modelisation of crater profiles," *Applied surface science*, vol. 186, no. 1-4, pp. 364–368, 2002.

[20] M. De Dood, A Polman, T Zijlstra, and E. Van der Drift, "Amorphous silicon waveguides for microphotonics," *Journal of applied physics*, vol. 92, no. 2, pp. 649–653, 2002.

[21] H. O. Jeschke, M. E. Garcia, M. Lenzner, J. Bonse, J. Krüger, and W. Kautek, "Laser ablation thresholds of silicon for different pulse durations: Theory and experiment," *Applied surface science*, vol. 197, pp. 839–844, 2002.

[22] D. Gómez and I. Goenaga, "On the incubation effect on two thermoplastics when irradiated with ultrashort laser pulses: Broadening effects when machining microchannels," *Applied Surface Science*, vol. 253, no. 4, pp. 2230–2236, 2006.

[23] S. Amoruso *et al.*, "Study of the plasma plume generated during near ir femtosecond laser irradiation of silicon targets," *Applied Physics A*, vol. 79, pp. 1377–1380, 2004.

[24] P. Pronko *et al.*, "Avalanche ionization and dielectric breakdown in silicon with ultrafast laser pulses," *Physical Review B*, vol. 58, no. 5, p. 2387, 1998.

[25] M. Meunier, B. Fisette, A. Houle, A. V. Kabashin, S. V. Broude, and P. Miller, "Processing of metals and semiconductors by a femtosecond laser-based microfabrication system," in *Commercial and Biomedical Applications of Ultrafast Lasers III*, SPIE, vol. 4978, 2003, pp. 169–179.

[26] F Costache, S. Kouteva-Arguirova, and J. Reif, "Sub–damage–threshold femtosecond laser ablation from crystalline si: Surface nanostructures and phase transformation," *Applied Physics A*, vol. 79, pp. 1429–1432, 2004.

[27] D. Tran, H. Zheng, Y. Lam, V. Murukeshan, J. Chai, and D. E. Hardt, "Femtosecond laser-induced damage morphologies of crystalline silicon by sub-threshold pulses," *Optics and Lasers in engineering*, vol. 43, no. 9, pp. 977–986, 2005.

[28] O. Armbruster, A. Naghilou, M. Kitzler, and W. Kautek, "Spot size and pulse number dependence of femtosecond laser ablation thresholds of silicon and stainless steel," *Applied Surface Science*, vol. 396, pp. 1736–1740, 2017.

[29] R. Goodarzi and F. Hajiesmaeilbaigi, "Circular ripple formation on the silicon wafer surface after interaction with linearly polarized femtosecond laser pulses in air and water environments," *Optical and Quantum Electronics*, vol. 50, pp. 1–17, 2018.

[30] L. Gallais *et al.*, "Wavelength dependence of femtosecond laser-induced damage threshold of optical materials," *Journal of Applied Physics*, vol. 117, no. 22, 2015.

[31] C. S. Nathala *et al.*, "Ultrashort laser pulse ablation of copper, silicon and gelatin: Effect of the pulse duration on the ablation thresholds and the incubation coefficients," *Applied Physics A*, vol. 122, no. 2, pp. 1–8, 2016.

[32] Y. Cai, Z.-l. Ma, Z. Zhang, G.-h. Cheng, X.-s. Ye, and D.-y. Cheng, "Experimental study of the damage of silicon photoelectric detector materials induced by repetitively pulsed femtosecond laser," in *2nd International Symposium on Laser Interaction with Matter (LIMIS 2012)*, SPIE, vol. 8796, 2013, pp. 115–120.

[33] J. Liu, "Simple technique for measurements of pulsed gaussian-beam spot sizes," *Optics letters*, vol. 7, no. 5, pp. 196–198, 1982.

[34] A. Naghilou, O. Armbruster, M. Kitzler, and W. Kautek, "Merging spot size and pulse number dependence of femtosecond laser ablation thresholds: Modeling and demonstration with high impact polystyrene," *The Journal of Physical Chemistry C*, vol. 119, no. 40, pp. 22 992–22 998, 2015.

[35] G. F. B. d. Almeida *et al.*, "Incubation effect during laser micromachining of gan films with femtosecond pulses," *Journal of Materials Science: materials in electronics*, vol. 30, no. 18, pp. 16 821–16 826, 2019.

[36] D Ashkenasi, M Lorenz, R Stoian, and A Rosenfeld, "Surface damage threshold and structuring of dielectrics using femtosecond laser pulses: The role of incubation," *Applied Surface Science*, vol. 150, no. 1-4, pp. 101–106, 1999.

[37] R. N. Oosterbeek, C. Corazza, S. Ashforth, and M. C. Simpson, "Effects of dopant type and concentration on the femtosecond laser ablation threshold and incubation behaviour of silicon," *Applied Physics A*, vol. 122, no. 4, pp. 1–10, 2016.

[38] Y. Jee, M. F. Becker, and R. M. Walser, "Laser-induced damage on single-crystal metal surfaces," *JOSA B*, vol. 5, no. 3, pp. 648–659, 1988.

[39] Z. Sun, M. Lenzner, and W. Rudolph, "Generic incubation law for laser damage and ablation thresholds," *Journal of Applied Physics*, vol. 117, no. 7, p. 073 102, 2015.

[40] F. Di Niso, C. Gaudiuso, T. Sibillano, F. P. Mezzapesa, A. Ancona, and P. M. Lugarà, "Role of heat accumulation on the incubation effect in multi-shot laser ablation of stainless steel at high repetition rates," *Optics express*, vol. 22, no. 10, pp. 12 200–12 210, 2014.

[41] J. Byskov-Nielsen, J.-M. Savolainen, M. S. Christensen, and P. Balling, "Ultra-short pulse laser ablation of metals: Threshold fluence, incubation coefficient and ablation rates," *Applied Physics A*, vol. 101, no. 1, pp. 97–101, 2010.

[42] C. Gaudiuso, G. Giannuzzi, A. Volpe, P. M. Lugarà, I. Choquet, and A. Ancona, "Incubation during laser ablation with bursts of femtosecond pulses with picosecond delays," *Optics Express*, vol. 26, no. 4, pp. 3801–3813, 2018.

[43] H Mustafa, R Pohl, T. Bor, B Pathiraj, D. Matthews, and G. Römer, "Picosecond-pulsed laser ablation of zinc: Crater morphology and comparison of methods to determine ablation threshold," *Optics express*, vol. 26, no. 14, pp. 18 664–18 683, 2018.

[44] M. J. Smith, M.-J. Sher, B. Franta, Y.-T. Lin, E. Mazur, and S. Gradečak, "The origins of pressure-induced phase transformations during the surface texturing of silicon using femtosecond laser irradiation," *Journal of Applied Physics*, vol. 112, no. 8, 2012.

[45] Y. Liu, Y. Ding, J. Xie, L. Xu, I. W. Jeong, and L. Yang, "One-step femtosecond laser irradiation of single-crystal silicon: Evolution of micro-nano structures and damage investigation," *Materials & Design*, vol. 225, p. 111 443, 2023.

[46] V. Van, *Optical microring resonators: theory, techniques, and applications*. CRC Press, 2016.

[47] B. S. Ahluwalia, Ø. I. Helle, and O. G. Hellesø, "Rib waveguides for trapping and transport of particles," *Optics express*, vol. 24, no. 5, pp. 4477–4487, 2016.

[48] A. V. Krishnamoorthy *et al.*, "Exploiting cmos manufacturing to reduce tuning requirements for resonant optical devices," *IEEE Photonics Journal*, vol. 3, no. 3, pp. 567–579, 2011.

[49] W. A. Zortman, D. C. Trotter, and M. R. Watts, "Silicon photonics manufacturing," *Optics express*, vol. 18, no. 23, pp. 23 598–23 607, 2010.

[50] M. M. Milosevic *et al.*, "Ion implantation in silicon for trimming the operating wavelength of ring resonators," *IEEE Journal of Selected Topics in Quantum Electronics*, vol. 24, no. 4, pp. 1–7, 2018.

[51] J. Schrauwen, D. V. Thourhout, and R. Baets, "Trimming of silicon ring resonator by electron beam induced compaction and strain," *Optics express*, vol. 16, no. 6, pp. 3738–3743, 2008.

[52] A. H. Atabaki, M. Askari, A. A. Eftekhar, and A. Adibi, "Accurate post-fabrication trimming of silicon resonators," in *The 9th International Conference on Group IV Photonics (GFP)*, IEEE, 2012, pp. 42–44.

[53] T. Lipka, M. Kiepsch, H. K. Trieu, and J. Müller, "Hydrogenated amorphous silicon photonic device trimming by uv-irradiation," *Optics express*, vol. 22, no. 10, pp. 12 122–12 132, 2014.

[54] V. Biryukova, G. J. Sharp, C. Klitis, and M. Sorel, "Trimming of silicon-on-insulator ring-resonators via localized laser annealing," *Optics Express*, vol. 28, no. 8, pp. 11 156–11 164, 2020.

[55] S. Prorok, A. Y. Petrov, M. Eich, J. Luo, and A. K.-Y. Jen, "Trimming of high-q-factor silicon ring resonators by electron beam bleaching," *Optics letters*, vol. 37, no. 15, pp. 3114–3116, 2012.

[56] J. Wang, Y. Yan, Z. Li, and Y. Geng, "Towards understanding the machining mechanism of the atomic force microscopy tip-based nanomilling process," *International Journal of Machine Tools and Manufacture*, vol. 162, p. 103 701, 2021.

[57] J. Wang, Y. Yan, C. Li, and Y. Geng, "Material removal mechanism and subsurface characteristics of silicon 3d nanomilling," *International Journal of Mechanical Sciences*, vol. 242, p. 108 020, 2023.

[58] D Bachman, Z Chen, R Fedosejevs, Y. Tsui, and V Van, "Threshold for permanent refractive index change in crystalline silicon by femtosecond laser irradiation," *Applied Physics Letters*, vol. 109, no. 9, p. 091 901, 2016.

[59] D. Bachman, Z. Chen, A. M. Prabhu, R. Fedosejevs, Y. Tsui, and V. Van, "Post-fabrication tuning of silicon microring resonators by femtosecond laser modification," in *Integrated Photonics Research, Silicon and Nanophotonics*, Optical Society of America, 2011, IME2.

[60] A. Garg, A. Kapoor, and K. Tripathi, "Laser-induced damage studies in gaas," *Optics and Laser Technology*, vol. 35, no. 1, pp. 21–24, 2003.

[61] P. Mannion, J Magee, E Coyne, G. O'connor, and T. Glynn, "The effect of damage accumulation behaviour on ablation thresholds and damage morphology in ultrafast laser micro-machining of common metals in air," *Applied surface science*, vol. 233, no. 1-4, pp. 275–287, 2004.

[62] A Rosenfeld, M Lorenz, R Stoian, and D Ashkenasi, "Ultrashort-laser-pulse damage threshold of transparent materials and the role of incubation," *Applied Physics A*, vol. 69, no. 1, S373–S376, 1999.

[63] B. Neuenschwander *et al.*, "Factors controlling the incubation in the application of ps laser pulses on copper and iron surfaces," in *Laser Applications in Microelectronic and Optoelectronic Manufacturing (LAMOM) XVIII*, International Society for Optics and Photonics, vol. 8607, 2013, p. 86070D.

[64] G. Raciukaitis, M. Brikas, P. Gecys, and M. Gedvilas, "Accumulation effects in laser ablation of metals with high-repetition-rate lasers," in *High-Power Laser Ablation VII*, International Society for Optics and Photonics, vol. 7005, 2008, p. 70052L.

[65] J. Krüger *et al.*, "Femto-and nanosecond laser treatment of doped polymethylmethacrylate," *Applied surface science*, vol. 247, no. 1-4, pp. 406–411, 2005.

[66] R. N. Oosterbeek, T. Ward, S. Ashforth, O. Bodley, A. E. Rodda, and M. C. Simpson, "Fast femtosecond laser ablation for efficient cutting of sintered alumina substrates," *Optics and Lasers in Engineering*, vol. 84, pp. 105–110, 2016.

[67] R. Streubel, S. Barcikowski, and B. Gökce, "Continuous multigram nanoparticle synthesis by high-power, high-repetition-rate ultrafast laser ablation in liquids," *Optics letters*, vol. 41, no. 7, pp. 1486–1489, 2016.

[68] R. Streubel, G. Bendt, and B. Gökce, "Pilot-scale synthesis of metal nanoparticles by high-speed pulsed laser ablation in liquids," *Nanotechnology*, vol. 27, no. 20, p. 205 602, 2016.

[69] S. v. Kirkwood, A. Van Popta, Y. Tsui, and R Fedosejevs, "Single and multiple shot near-infrared femtosecond laser pulse ablation thresholds of copper," *Applied Physics A*, vol. 81, no. 4, pp. 729–735, 2005.

[70] J. Bonse, A. Rosenfeld, and J. Krüger, "On the role of surface plasmon polaritons in the formation of laser-induced periodic surface structures upon irradiation of silicon by femtosecond-laser pulses," *Journal of Applied Physics*, vol. 106, no. 10, p. 104 910, 2009.

[71] Y. Painchaud, M. Poulin, J.-F. Gagné, and C. Paquet, "Ultra-compact si-photonic dqpsk demodulator," in *Optical Fiber Communication Conference*, Optica Publishing Group, 2012, OM3J–3.

[72] D. Bachman, Z. Chen, A. M. Prabhu, R. Fedosejevs, Y. Y. Tsui, and V. Van, "Femtosecond laser tuning of silicon microring resonators," *Optics letters*, vol. 36, no. 23, pp. 4695–4697, 2011.

[73] B. Jalali and S. Fathpour, "Silicon photonics," *Journal of lightwave technology*, vol. 24, no. 12, pp. 4600–4615, 2006.

[74] W. Bogaerts *et al.*, "Silicon microring resonators," *Laser & Photonics Reviews*, vol. 6, no. 1, pp. 47–73, 2012.

[75] M. Á. Guillén-Torres *et al.*, "Effects of backscattering in high-q, large-area silicon-on-insulator ring resonators," *Optics Letters*, vol. 41, no. 7, pp. 1538–1541, 2016.

[76] R. Zhang, A. McDowell, F. Hegmann, R. Fedosejevs, and Y. Y. Tsui, "A study of incubation effects in femtosecond laser irradiation of silicon and copper," *Applied Physics A*, vol. 129, no. 2, p. 131, 2023.

[77] A. Stalmashonak, N. Zhavoronkov, I. V. Hertel, S. Vetrov, and K. Schmid, "Spatial control of femtosecond laser system output with submicroradian accuracy," *Applied optics*, vol. 45, no. 6, pp. 1271–1274, 2006.

[78] G. Ballesteros, J. Matres, J. Martí, and C. Oton, "Characterizing and modeling backscattering in silicon microring resonators," *Optics express*, vol. 19, no. 25, pp. 24 980–24 985, 2011.

[79] R. E. Samad, S. L. Baldochi, and N. D. Vieira Jr, "Diagonal scan measurement of cr: Lisaf 20 ps ablation threshold," *Applied optics*, vol. 47, no. 7, pp. 920–924, 2008.

[80] S. Amoruso *et al.*, "Thermal and nonthermal ion emission during high-fluence femtosecond laser ablation of metallic targets," *Applied Physics Letters*, vol. 77, no. 23, pp. 3728–3730, 2000.

[81] Y. Hayasaki, M. Isaka, and A. Takita, "Time-resolved interference observation of femtosecond-laser induced phenomena in glass," in *AIP Conference Proceedings*, American Institute of Physics, vol. 1236, 2010, pp. 454–458.

[82] M Lancry, B Poumellec, A Chahid-Erraji, M. Beresna, and P. Kazansky, "Dependence of the femtosecond laser refractive index change thresholds on the chemical composition of doped-silica glasses," *Optical Materials Express*, vol. 1, no. 4, pp. 711–723, 2011.

[83] J. Bonse and J. Krüger, "Structuring of thin films by ultrashort laser pulses," *Applied physics A*, vol. 129, no. 1, p. 14, 2023.

[84] P. Venkat and T. Otobe, "Thickness dependence of laser damage in silicon thin films.," *Journal of Laser Micro/Nanoengineering*, vol. 18, no. 3, 2023.

[85] Y. Izawa, M Fujita, Y Setsuhara, M Hashida, and Y Izawa, "Surface modification of crystalline si irradiated by femtosecond laser pulses," in *CLEO/Europe. 2005 Conference on Lasers and Electro-Optics Europe, 2005.*, IEEE, 2005, pp. 663–663.

[86] Z. Sun and M. C. Gupta, "A study of laser-induced surface defects in silicon and impact on electrical properties," *Journal of Applied Physics*, vol. 124, no. 22, 2018.

[87] Z. Sun and M. C. Gupta, "Laser processing of silicon for photovoltaics and structural phase transformation," *Applied Surface Science*, vol. 456, pp. 342–350, 2018.

[88] T. M. Benson, S. V. Boriskina, P. Sewell, A. Vukovic, S. C. Greedy, and A. I. Nosich, "Micro-optical resonators for microlasers and integrated optoelectronics," in *Frontiers in Planar Lightwave Circuit Technology: Design, Simulation, and Fabrication*, Springer, 2006, pp. 39–70.

[89] Y. Han *et al.*, "Evolution mechanism of subsurface damage during laser machining process of fused silica," *Optics Express*, vol. 32, no. 9, pp. 16 273–16 291, 2024.

Appendix A: Shot-to-Shot femtosecond tuning and optical characterization system

A diagram of the online characterization platform is shown in Fig.A.1. The laser-irradiation subsystem and optical characterization subsystem share the same sample holder and imaging system, where the laser beam comes perpendicular to the silicon resonator sample surface. The lensed fibers are installed parallel to the sample surface for waveguide edge-coupling.

A.1 Optical characterization subsystem setup

Two of the key components, Superluminescent LEDs (SLED) and an Optical Spectral analyzer (OSA), are applied in our system for resonant wavelength measurement with high accuracy and efficiency.

A.1.1 light source

The SLED equipment is applied as the input light source in the characterization system, which can provide a constant and similar output power level within the 150 nm range of wavelengths from 1450 - 1600nm. Simultaneously, the output signal from the waveguide is analyzed using an OSA instead of the power meter, which displays the full resonance wavelength spectrum instantaneously.

The SLED applied in our experiment is a multi-SLD module Modeled SN00081 from LUXMUX. Such a model combines various SLEDs in a single module called the

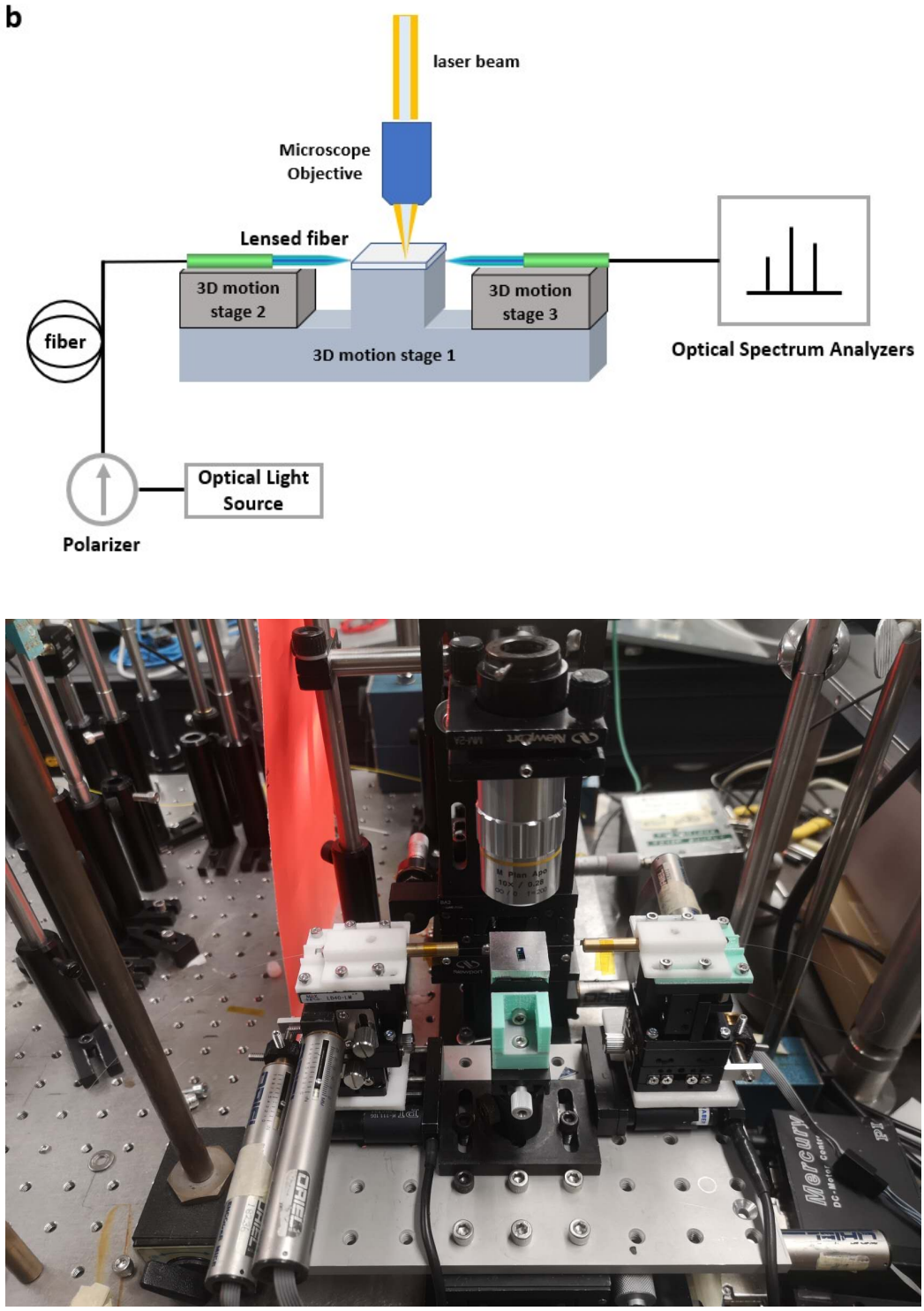

Figure A.1: (a) Scheme of the experimental setup of the optical characterization subsystem. Two lensed fibres are installed parallel to the sample surface on each side. The fiber-coupled optical light source goes through the fiber polarizer first and connects to the lensed fibre on the input side, and the output fibre is connected to an optical spectrum analyzer for signal processing. (b)Picture of the online characterization system when the fiber and sample chip are loaded.

"OSE module.", as shown in Fig.A.2a The machine is packaged into an integrated-spectral-bench (ISB)-system, including an OSE module, power supply, cooling, and isolator. The comprehensive software makes it an easy-to-use turn-key solution. These 32-PIN-butterfly packages emit between 1265 nm - 1725 nm, with spectral widths of up to 460 nm and 40 mW output power..The single SLEDs can be operated individually. In our experiment we just applied the range from 1405 nm - 1610 nm.

A.1.2 Optical signal Analyser

An Optical spectrum analyzers (OSA) from YOKOGAWA modelled AQ6370B is used in the experiment measuring optical spectra(Fig. A.2b). Some typical applications include characterizing light sources like lasers and LEDs, testing optical systems (such as wavelength division multiplexing systems in optical fiber communications networks, where one may need to test the optical powers of different wavelength channels and measure signal-to-noise ratios), measuring the wavelength-dependent transmissivity or reflectivity of optical systems or devices by comparing spectra with and without the device, and characterizing fiber amplifiers (e.g., telecom erbium-doped fiber amplifiers) in terms of wavelength-dependent gain and noise figure.

Theoretically, an optical spectrum should show the power spectral density (PSD) as a function of wavelength or optical frequency. However, the display of a spectral analyzer often shows an optical power on the vertical axis rather than PSD. One can obtain PSD by dividing that power through the chosen detection bandwidth. However, similar to electronic spectrum analyzers, these power spectral densities may not be accurate. Calibration is often done for quasi-monochromatic light. If the bandwidth is defined via its full width at half maximum (FWHM), it depends on the filter shape how well the power divided by the bandwidth agrees with the power spectral density. An example of the full spectrum of our SLED from the wavelength range of 1200 nm to 1700 nm measured by our OSA is shown in Fig. A.3. The relatively constant output power from 1450-1600nm was used in the characterization

Figure A.2: Picture of the SLED multi-SLD module Modeled SN00081 from LUXMUX.

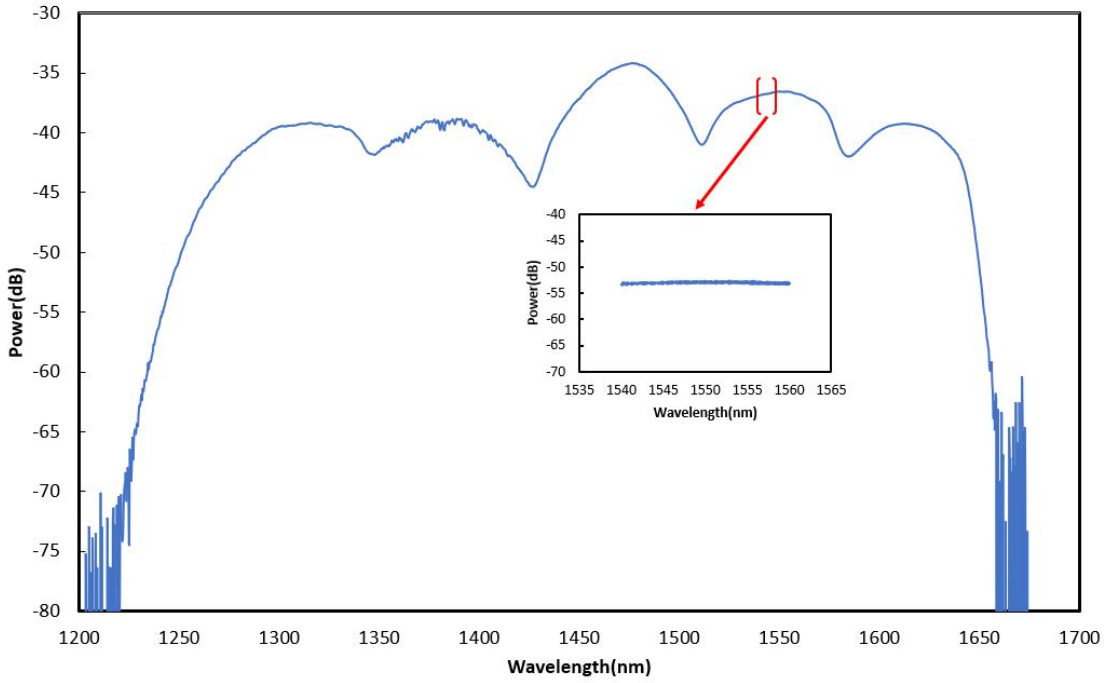

Figure A.3: Example of SLED spectrum extracted on OSA with wavelength range from 1200nm to 1700nm. The figure insert presents the narrower bandwidth of the spectrum from 1540nm-1560nm.

study of the unirradiated and irradiated SiMRRs. Most measurements used the flat spectra range of 1540 nm to 1560 nm which is shown in the insert.of Fig.A.3.

A.1.3 Fiber edge coupling subystem

The fiber edge coupling subsystems are installed on two sides of the primary sample holder, where the laser-irradiation subsystem and optical characterization subsystem share the same sample holder and imaging system, and the laser beam comes perpendicular to the silicon resonator sample surface, as shown in Fig/A.1b. To make the system more cost-efficient, instead of using the expensive commercial motion stages, all the 3D motion stages we applied in our system are rebuilt from manual motion stages. All the conjunction part fittings for the electric actuators are replaced with parts printed using PETG from an FDM 3D printer in our lab(Fig.A.4a). Two different models of electric motion actuators are used in the system: The Motor Mike

Oriel Linear Actuator (Fig.A.5) and the PI motion stage(Fig.A.6). The 3 axes of the main motion stage and the Y, and Z direction axis of the fibre coupling alignment motion stages are controlled with the motor Mike Oriel linear Actuator, which can provide a resolution of $\sim$ 100um and a motion range of 20 cm when controlled by two sets of 18805 Mike Controller. The PI motion stage is used for the X direction of the alignment motion stage. It can give the smallest step size of 10nm when controlled by computer, providing a best precision of the motion and avoid cracking between the lensed fibre and the waveguide edge coupler. The lensed fibers are installed parallel to the sample surface for waveguide edge-coupling.

A.1.4 Procedures of sample loading to optical characterization subsystem

Here is a detailed procedure for tuning experiment on the online optical:

1. A tunable laser(Fig.**??**) set at a specific wavelength and power (e.g., 1 mW output power at 1550 nm wavelength) is used as the input light source to make monitoring the intensity change on the OSA easier because of its much narrower bandwidth spectrum(¡ 1.5nm).

2. The alignment of the lensed fiber on both sides is usually performed alternatively by adjusting the lensed fiber using all the 3-axes-motion stages in small steps until the best coupling efficiency of the laser is obtained. Monitoring the position of the lensed fibre relative to the waveguide output coupler is essential to avoid a collision.

3. Upon adjusting the lensed fibre on all 3 axes of motion stages, the output fibre signal to the OSA should start to present a significant increase in the laser peak power. In our case, the laser peak shows with $\sim$ several picowatts and significantly increases when the axis is moved in the correct direction. When coupled well on both sides, the signal level will be at least $\sim$ 200-300 nanowatts(Fig.A.8).

5. After the alignment process is completed, the lensed fiber is usually placed

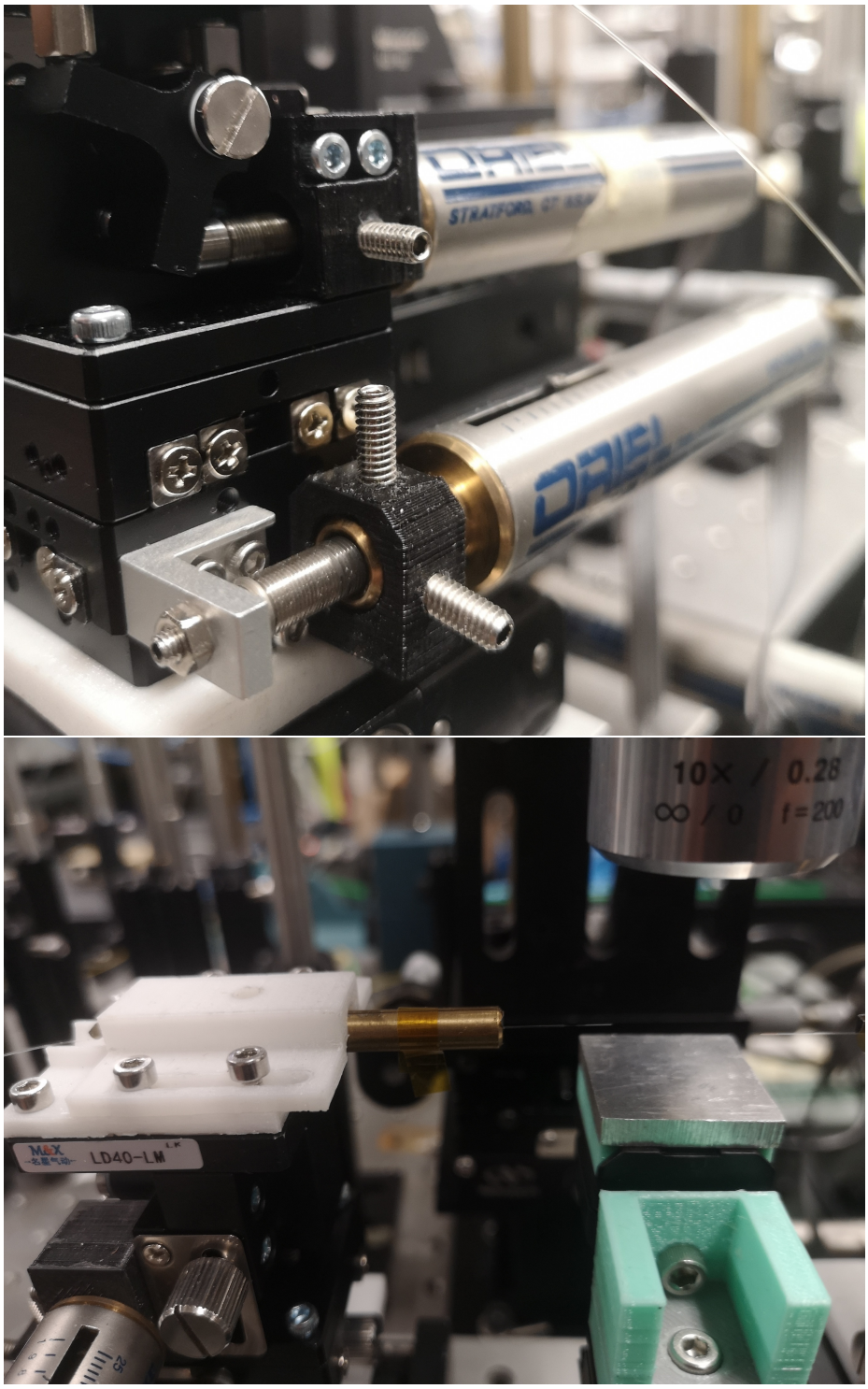

Figure A.4: (a)An example of the 3D printed conjunction Part for revising the manual motion stage into electrically driven stages. (b) 3D printed fiber holder

Figure A.5: Linear motion actuator and the controller. (a) The Oriel Linear Encoder Actuator. (b) The corresponding encoder Controller Mike

Figure A.6: The PI motion stage.

Figure A.7: The tunable laser System used in the experiment.

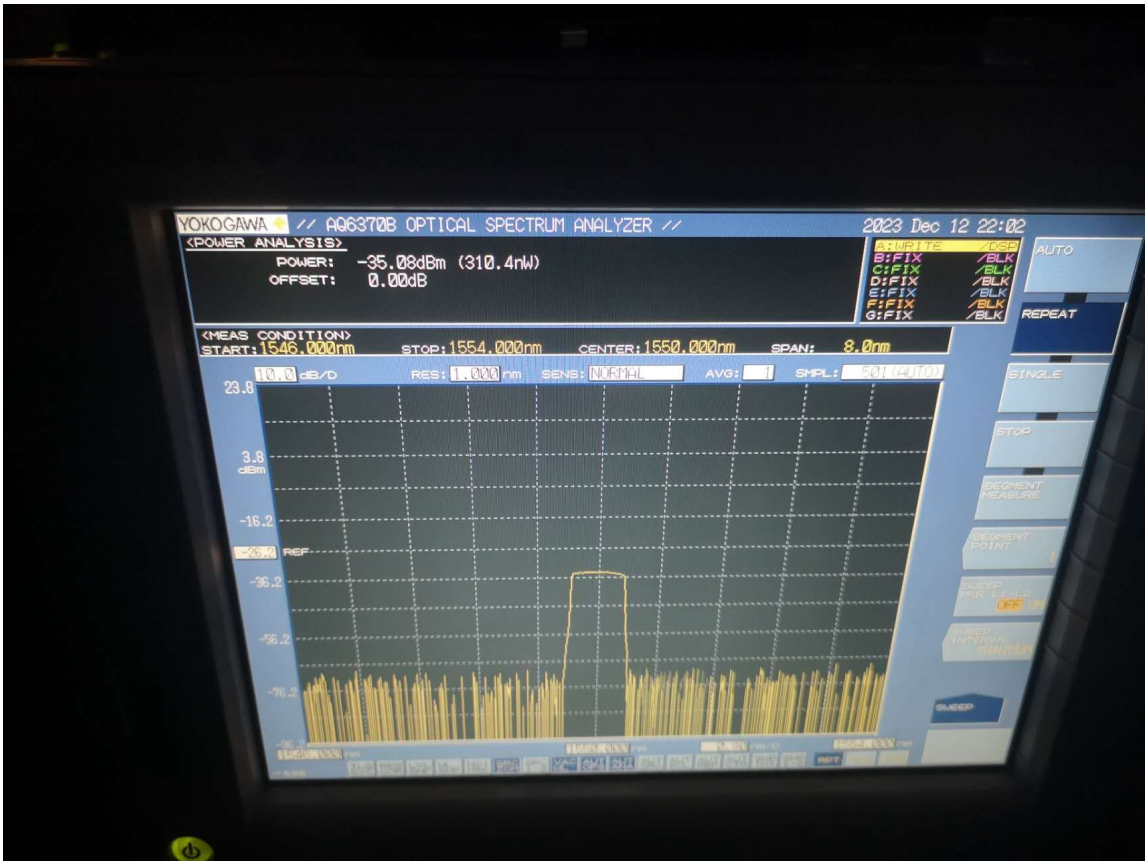

Figure A.8: An example of the signal from a tunable laser system shown on OSA is when the fibers on two sides of the edge coupler are well aligned to the best position.

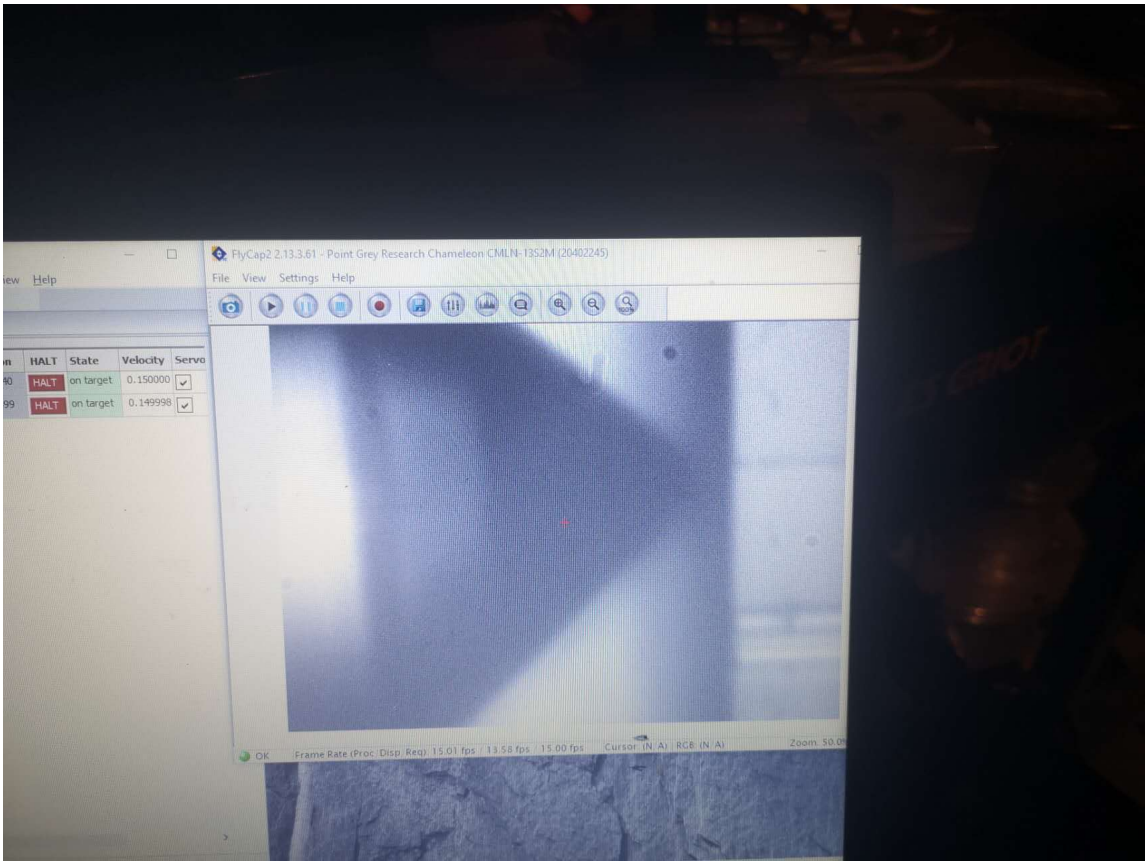

Figure A.9: An example of how the lensed fiber is shown on the monitor at the well-aligned position.

roughly 5 µm away from the edge of the waveguide coupler. An example of how the lensed fiber is shown on the monitor at the well-aligned position is as shown in Fig.A.9.

6. Gentlly tune the fiber polarizor until the maxium signal is shown on the OSA, where the correct polarization of mode can be obtained.

7. Move the sample holder motion stage until the resonator is shown at the center of the imaging system. Adjust the z axis until a sharp and clear image of the waveguide structures is shown on the screen.

8. The Imaging system and laser irradiation focusing system is preset to be at the same focal plane. Therefore, a clear image of the waveguide structure often indicates that it is not far away from the best focus.

9. After completing the alignment of the lensed fibers, the input light source is switched to SLED, and the full resonance wavelength spectrum should appear on the OSA display(Fig.A.10).. Final optimization of the OSA settings, such as scanning resolution and number of sampling points, is conducted. The SiMRR is successfully loaded onto the optical characterization subsystem and is ready for further irradiation experiments

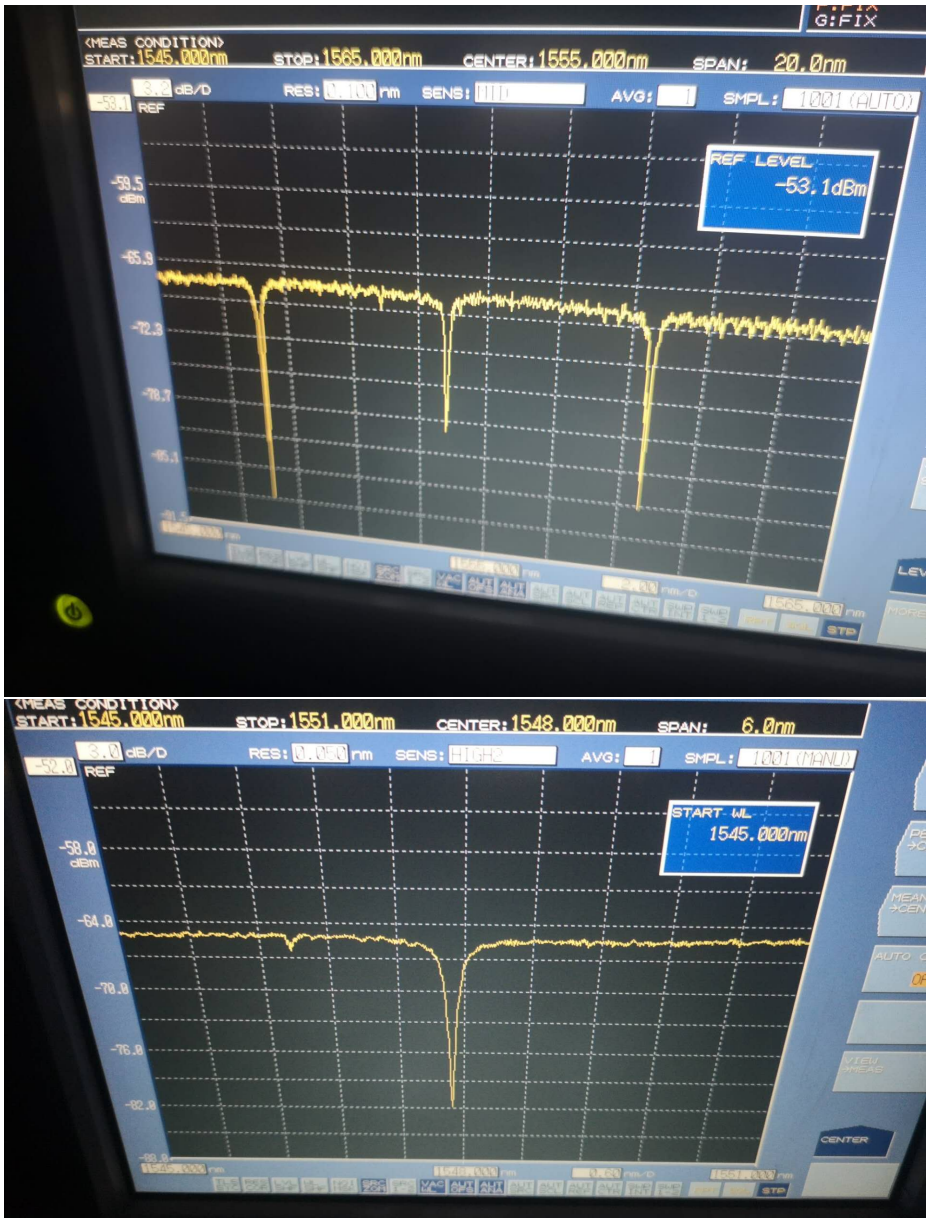

Figure A.10: An example of the resonance wavelength for racetrack microring resonator by applying the real-time characterization system using SLED as the light source and output coupled to OSA for spectrum measurement. (a) The spectrum with more than 2 FSR of the resonance. (b) The spectrum with better resolution within 1 FSR of the resonance.

Appendix B: Supplementary results for shot-to-shot characterization of SiMRR with multi-shot tuning technique

In appendix B, supplementary results for the shot-to-shot characterization of the SiMRR using multi-shot tuning technique are shown with fluences ranging from $0.0232 J/cm^2$ to $0.055 J/cm^2$ respectively. The accumulated resonance wavelength shifts corresponding to different pulse numbers, the spectrum of the accumulated resonance wavelength shifts corresponding to different pulse numbers and some analysis of induced roundtrip loss are provided in this appendix.

F = $0.0256 J/cm^2$: F = $0.0297 J/cm^2$: F = $0.0302 J/cm^2$: F = $0.0308 J/cm^2$: F = $0.0372 J/cm^2$: F = $0.0428 J/cm^2$: F = $0.0431 J/cm^2$: F = $0.0452 J/cm^2$: F = $0.0453 J/cm^2$: F = $0.0502 J/cm^2$: F = $0.055 J/cm^2$:

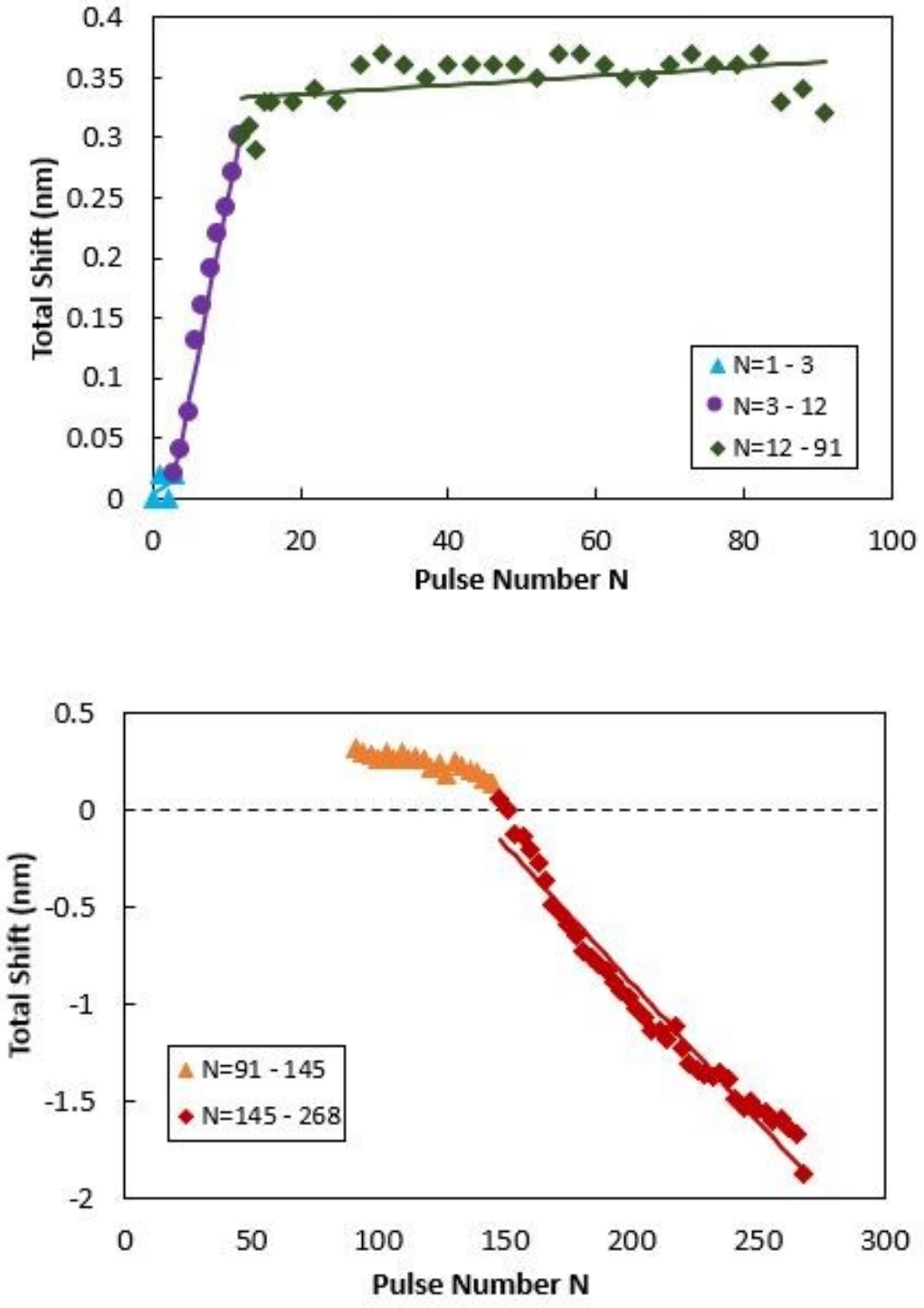

Figure B.1: The accumulated resonance wavelength shifts corresponding to different pulse numbers at a fluence of $0.0256 J/cm^2$.

Table B.1: Equations representing the data for regions A to E in Fig. B.1

Region	**N**	**Equation** $\Delta\lambda$ is the induced resonance wavelength shift after irradiated by N shots	**Tuning Precision (pm/shot)**
A	1 - 3	$\Delta\lambda = 0$	
B	4 - 12	$\Delta\lambda = 0.032N - 0.076$	3.2 ± 0.1206
C	12 - 91	$\Delta\lambda = 0.000378N - 0.328478$	0.378 ± 0.144
D	91 - 145	$\Delta\lambda = -0.00258N + 0.545895$	2.58 ± 0.313
E	145 - 268	$\Delta\lambda = -0.01419N + 1.946723$	14.19 ± 0.436

Table B.2: Equations representing the data for regions A to E in Fig. B.2

Region	**N**	**Equation** $\Delta\lambda$ is the induced resonance wavelength shift after irradiated by N shots	**Tuning Precision (pm/shot)**
A	1 - 2	$\Delta\lambda = 0$	
B	2 - 12	$\Delta\lambda = 0.036N - 0.1737$	36.091 ± 7.147
C	13 - 49	$\Delta\lambda = 0.00054N - 0.596627$	0.54 ± 0.08
D	50 - 82	$\Delta\lambda = -0.01518N - 1.393545$	15.18 ± 1.239
E	82 - 100	$\Delta\lambda = -0.06571N + 5.517143$	65.71 ± 1.572

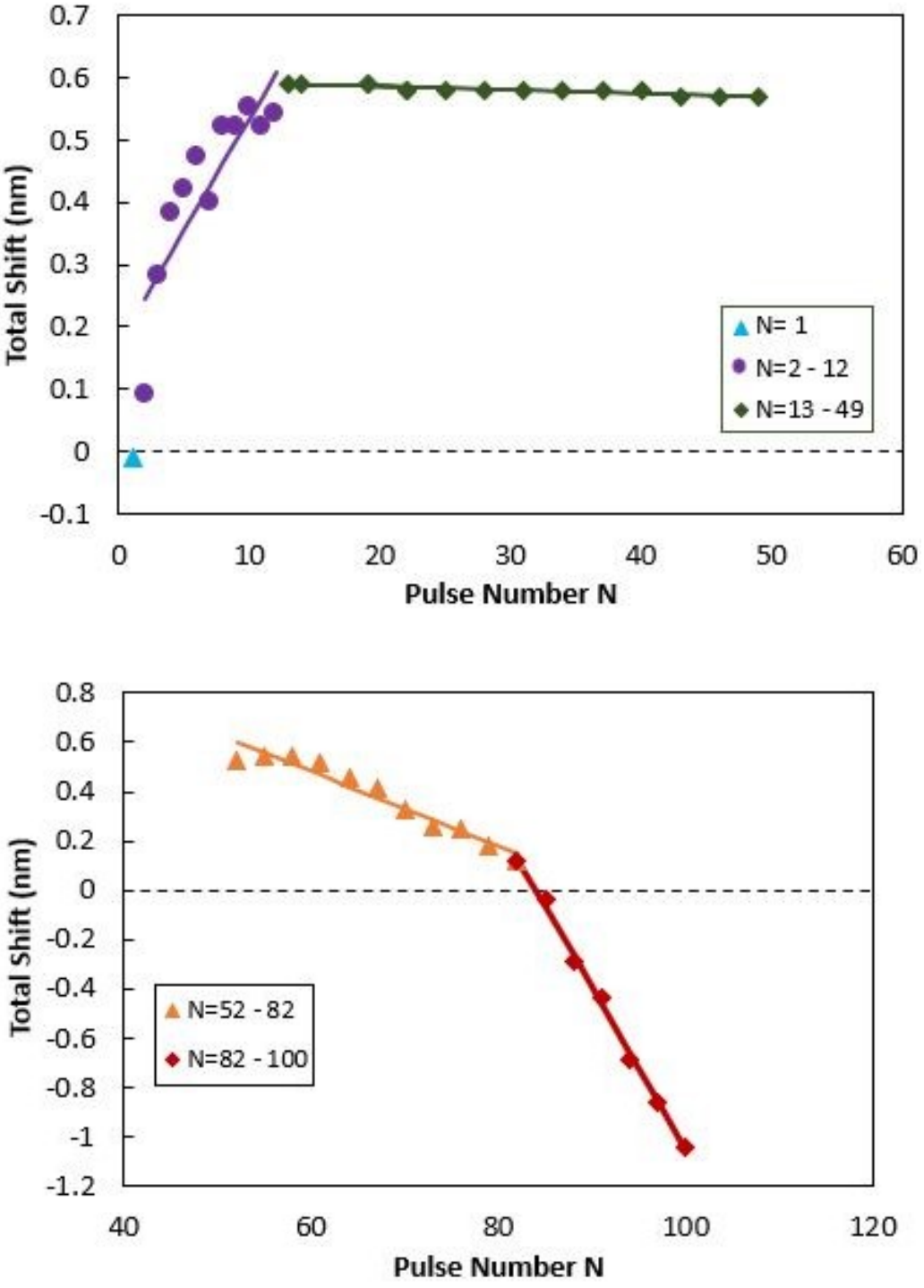

Figure B.2: The accumulated resonance wavelength shifts corresponding to different pulse numbers at a fluence of $0.0297 J/cm^2$.

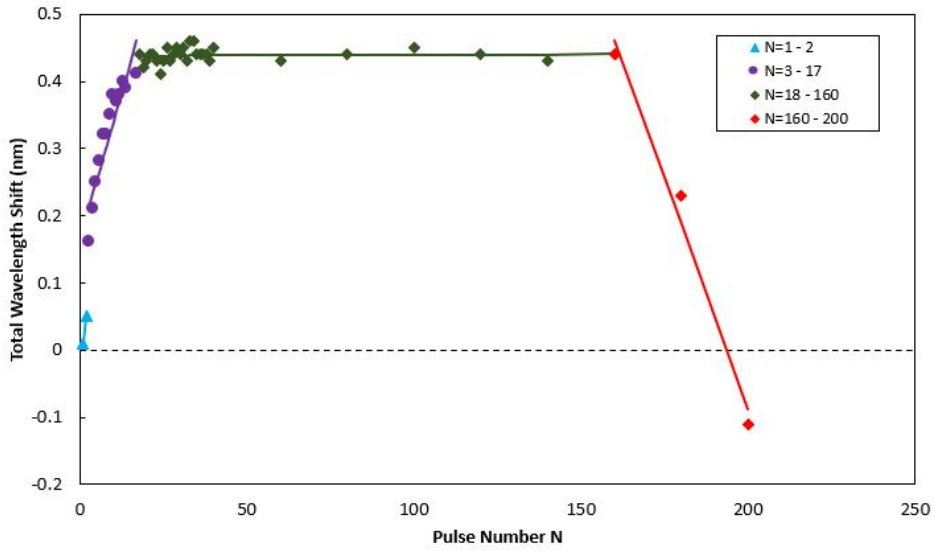

Figure B.3: The accumulated resonance wavelength shifts corresponding to different pulse numbers at a fluence of $0.0302 J/cm^2$.

Table B.3: Equations representing the data for regions A to D in Fig. B.3

Region	**N**	**Equation** $\Delta\lambda$ is the induced resonance wavelength shift after irradiated by N shots	**Tuning Precision (pm/shot)**
A	1 - 2	$\Delta\lambda = 0$	
B	3 - 17	$\Delta\lambda = 0.017315N - 0.166119$	17.315 ± 2.189
C	18 - 160	$\Delta\lambda = 0.0000171N - 0.437839$	0.0171 ± 0.0561
D	160 - 200	$\Delta\lambda = -0.01375N + 2.661667$	13.75 ± 1.876

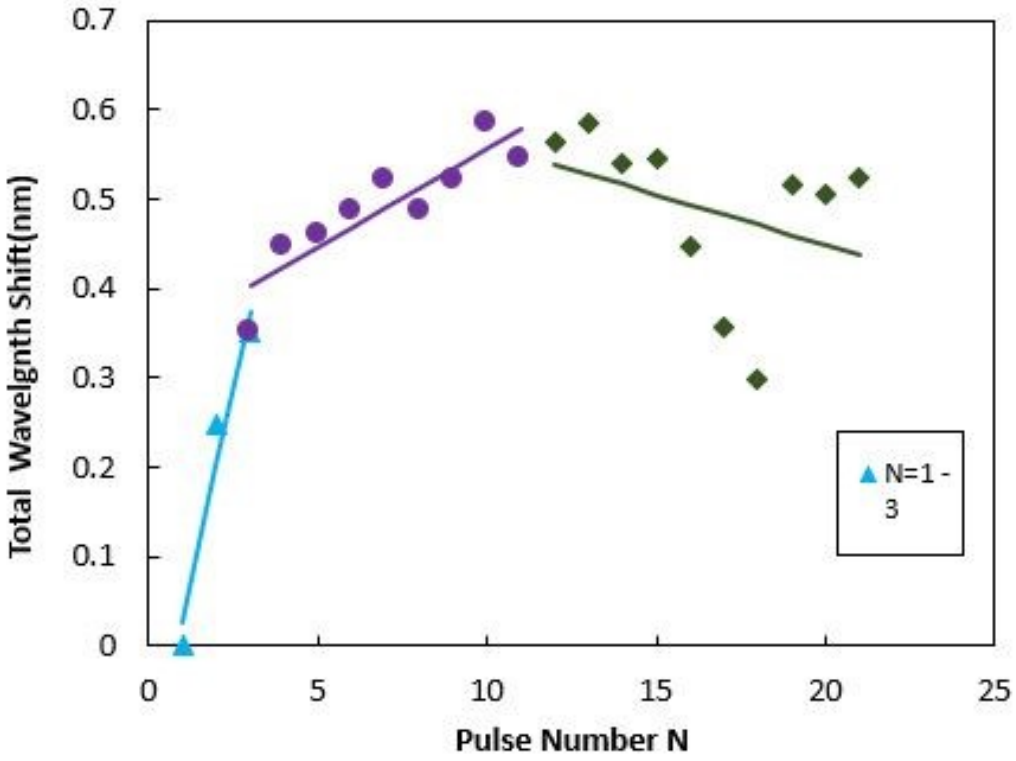

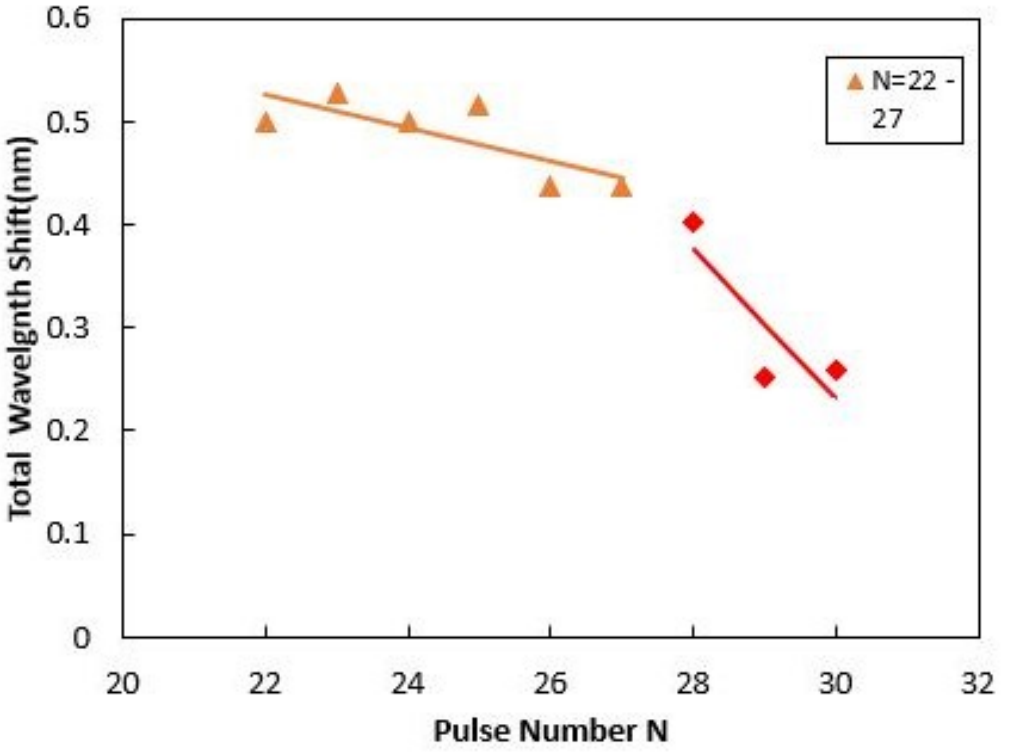

Figure B.4: The accumulated resonance wavelength shifts corresponding to different pulse numbers at a fluence of $0.0308 J/cm^2$.

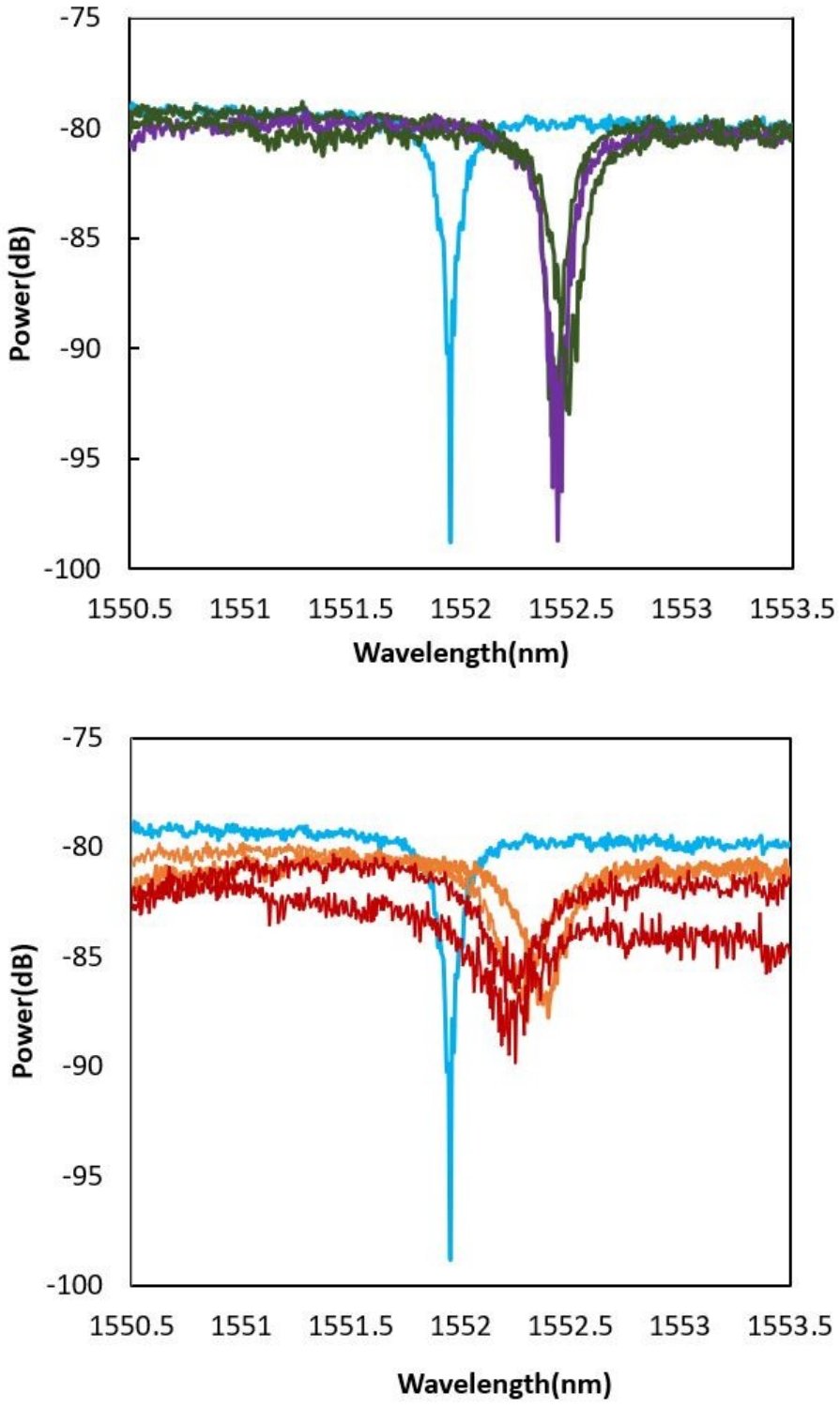

Figure B.5: Example of the spectrum of the accumulated resonance wavelength shifts corresponding to different pulse numbers at a fluence of $0.0308 J/cm^2$. The different colours of the resonance plot represented corresponded to the different regions described in Chapter 6: Region A: Blue; Region B: purple; Region C: Green; Region D: orange; Region E: Red.

Table B.4: Equations representing the data for regions A to E in Fig. B.4

Region	**N**	**Equation** $\Delta\lambda$ is the induced resonance wavelength shift after irradiated by N shots	**Tuning Precision (pm/shot)**
A	1 - 2	$\Delta\lambda = 0$	
B	3 - 11	$\Delta\lambda$ = 0.022007N - 0.335753	22 ± 4.203
C	12 - 21	$\Delta\lambda$ = -0.01127N – 0.67388	11.27 ± 10.104
D	22 - 27	$\Delta\lambda$ = -0.1634N - 0.886127	16.34 ± 6.855
E	28 - 30	$\Delta\lambda$ = -0.0715N - 2.378133	71.5 ± 44.6

Table B.5: Equations representing the data for regions A to E in Fig. B.6

Region	**N**	**Equation** $\Delta\lambda$ is the induced resonance wavelength shift after irradiated by N shots	**Tuning Precision (pm/shot)**
A	1	$\Delta\lambda = 0$	
B	2 - 10	$\Delta\lambda$ = 0.047976N - 0.319405	47.97 ± 8.732
C	11 - 22	$\Delta\lambda$ = -0.00138N – 0.76004	1.38 ± 1.125
D	23 - 39	$\Delta\lambda$ = -0.01668N - 1.059059	16.68 ± 1.535
E	39 - 43	$\Delta\lambda$ = -0.106N - 4.534	106 ± 9.59

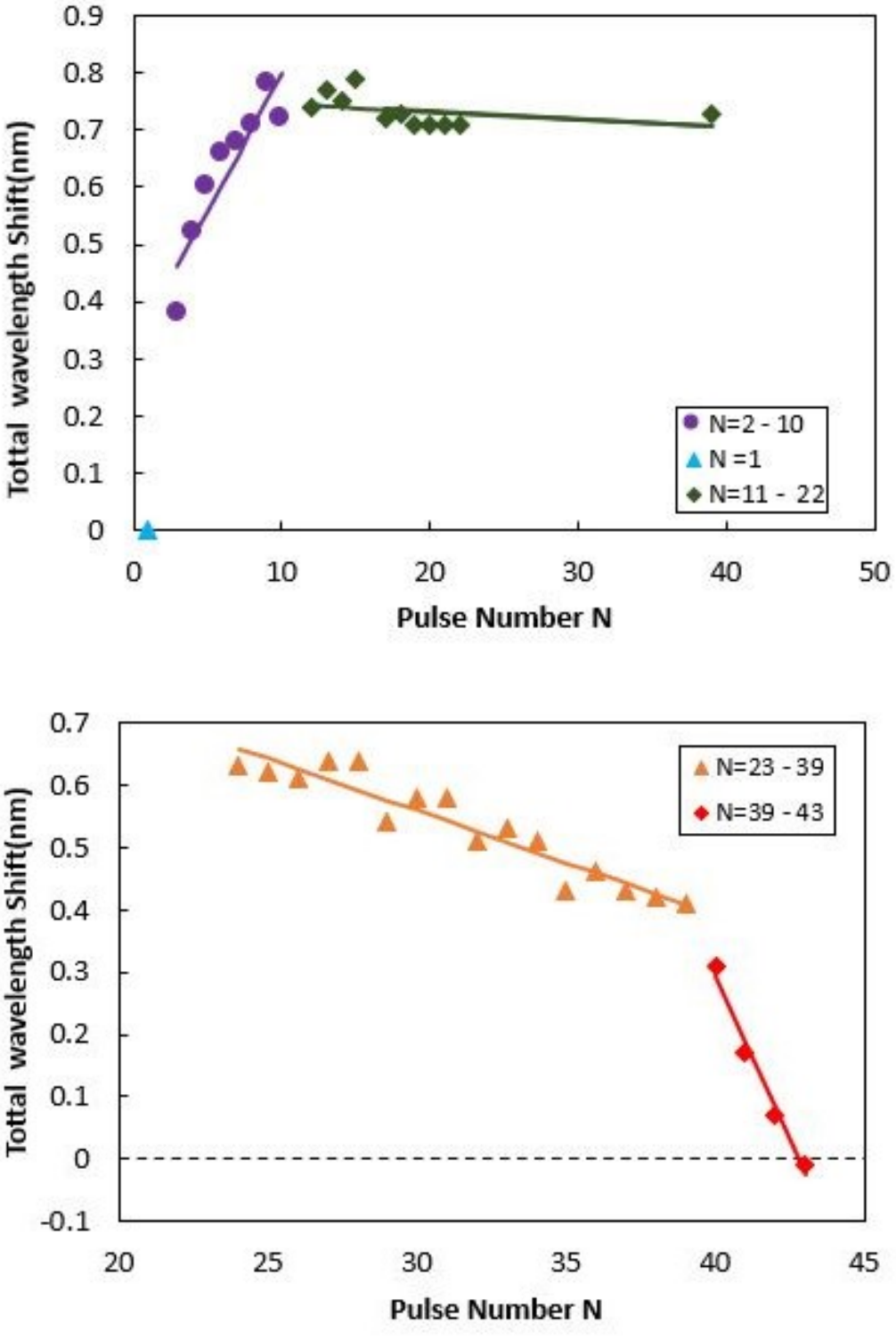

Figure B.6: The accumulated resonance wavelength shifts corresponding to different pulse numbers at a fluence of $0.0372 J/cm^2$.

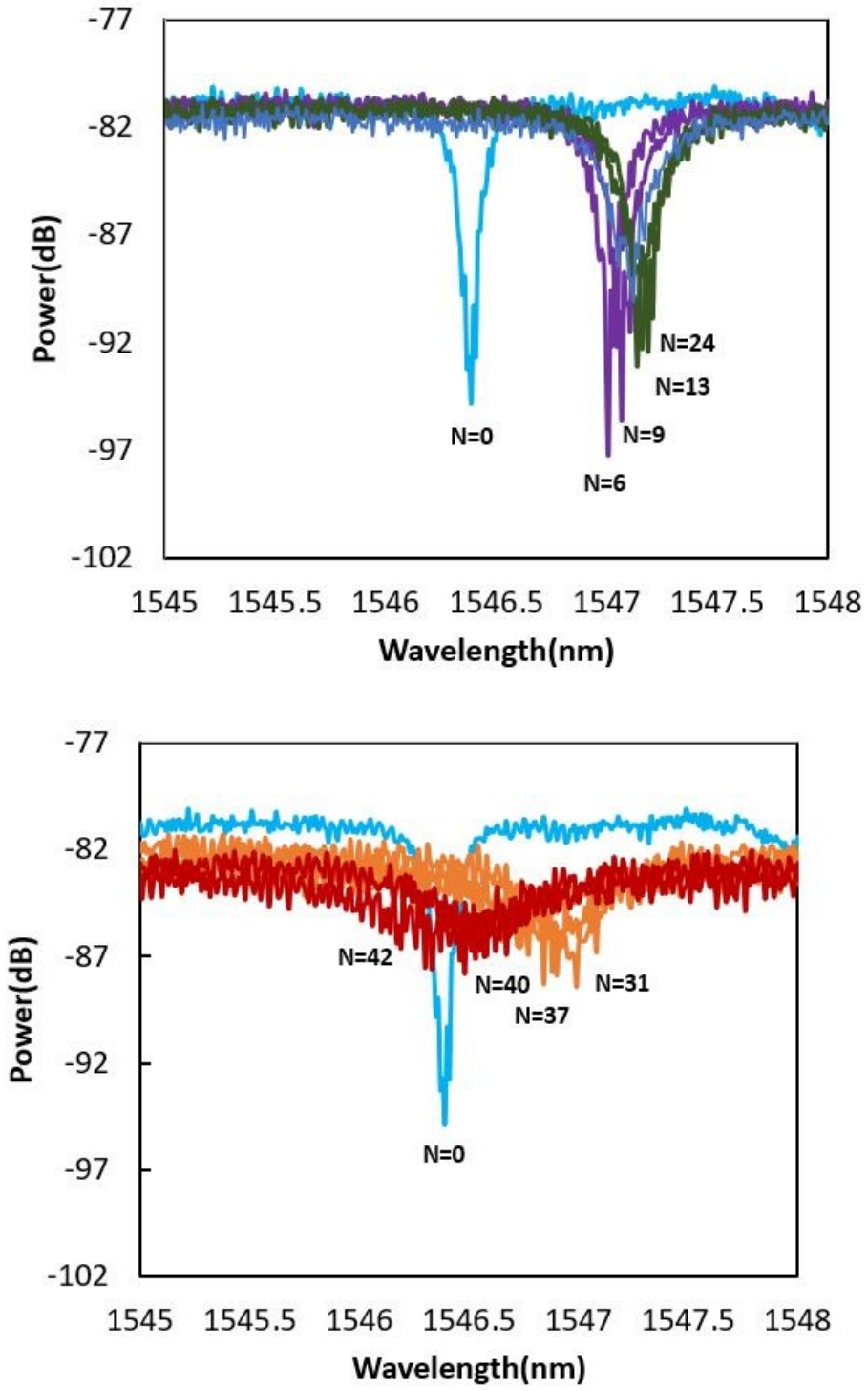

Figure B.7: Example of the spectrum of the accumulated resonance wavelength shifts corresponding to different pulse numbers at a fluence of $0.0372 J/cm^2$. The different colours of the resonance plot represented corresponded to the different regions described in Chapter 6: Region A: Blue; Region B: purple; Region C: Green; Region D: orange; Region E: Red.

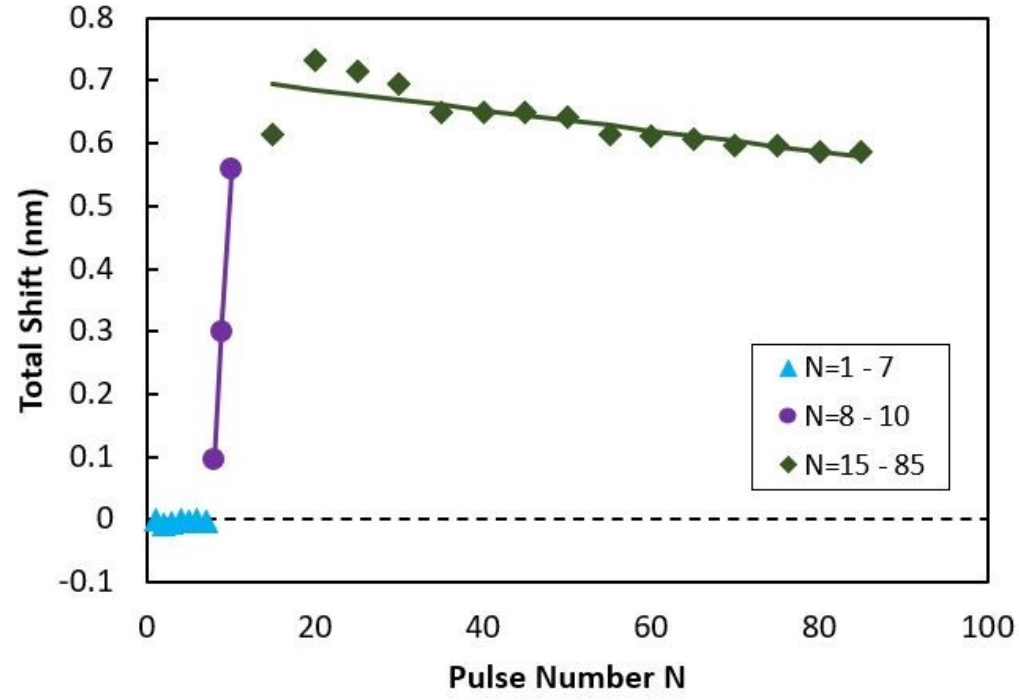

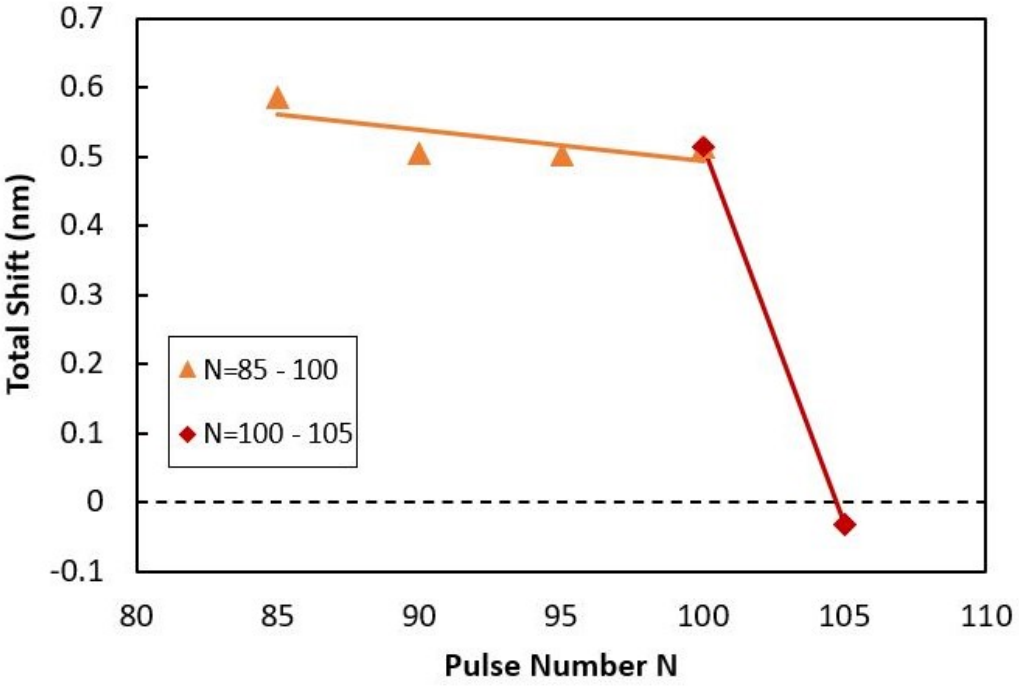

Figure B.8: The accumulated resonance wavelength shifts corresponding to different pulse numbers at a fluence of $0.0428 J/cm^2$.

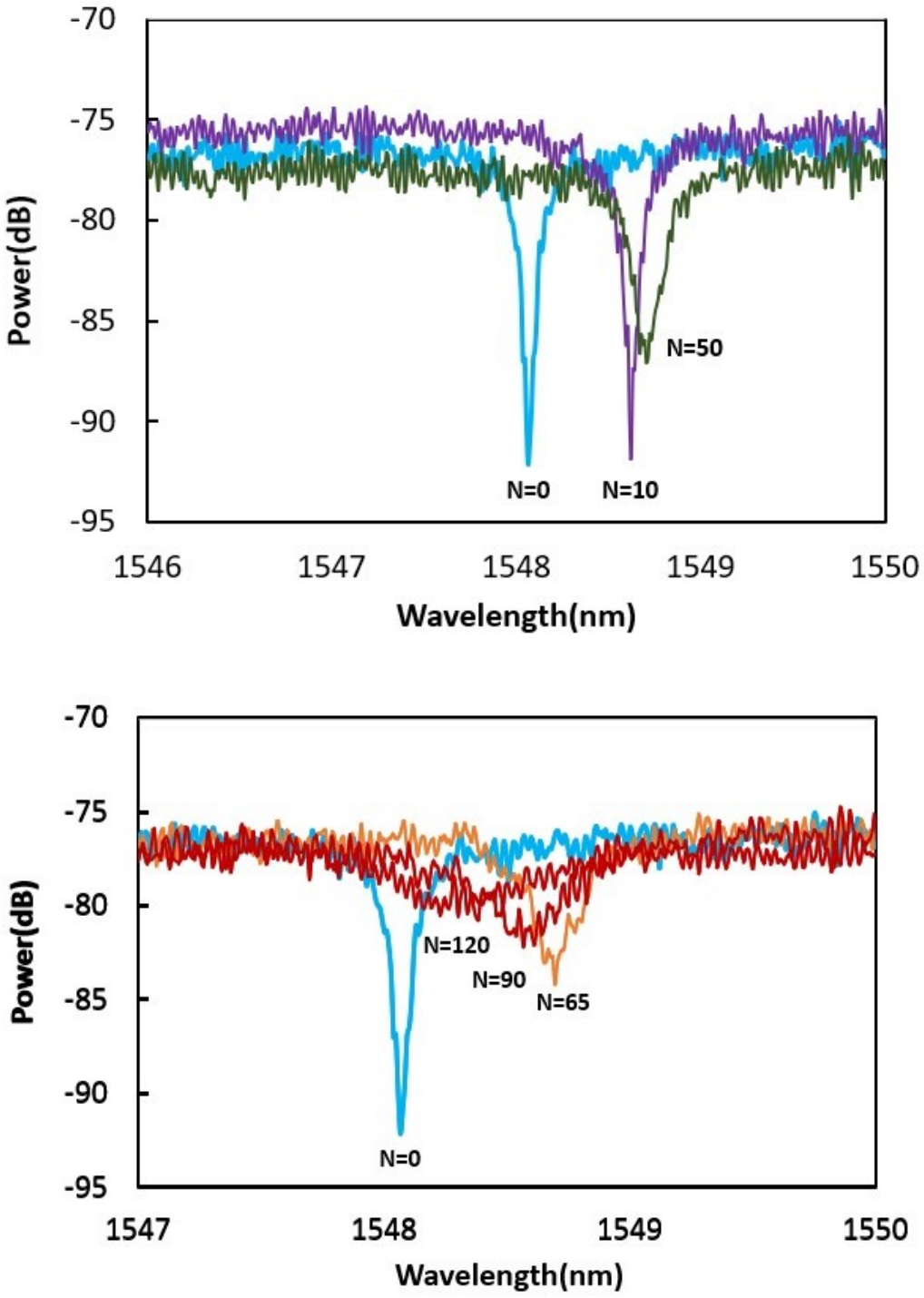

Figure B.9: Example of the spectrum of the accumulated resonance wavelength shifts corresponding to different pulse numbers at a fluence of $0.0428 J/cm^2$. The different colours of the resonance plot represented corresponded to the different regions described in Chapter 6: Region A: Blue; Region B: purple; Region C: Green; Region D: orange; Region E: Red.

Table B.6: Equations representing the data for regions A to E in Fig. B.8

Region	**N**	**Equation** $\Delta\lambda$ is the induced resonance wavelength shift after irradiated by N shots	**Tuning Precision (pm/shot)**
A	1 - 7	$\Delta\lambda$ = 0.000271N - 0.00386	0.271 ± 0.45
B	8 - 10	$\Delta\lambda$ = 0.23165N + 1.76695	231.65 ± 15.502
C	15 - 85	$\Delta\lambda$ = -0.00165N – 0.718673	1.65 ± 0.352
D	85 - 100	$\Delta\lambda$ = -0.00442N - 0.93534	4.42 ± 3.036
E	100 - 105	$\Delta\lambda$ = -0.1091N - 11.4227	109.1 ± 0

Table B.7: Equations representing the data for regions A to E in Fig. B.10

Region	**N**	**Equation** $\Delta\lambda$ is the induced resonance wavelength shift after irradiated by N shots	**Tuning Precision (pm/shot)**
A	1	$\Delta\lambda$ = 0	
B	2 - 4	$\Delta\lambda$ = 0.28N + 0.17	280 ± 34.64
C	4 - 18	$\Delta\lambda$ = -0.006714N – 0.933476	6.71 ± 2.39
D	18 - 23	$\Delta\lambda$ = 0.015143N - 0.801238	15.143 ± 6.177
E	23 - 28	$\Delta\lambda$ = -0.164N - 4.908667	164 ± 8.663

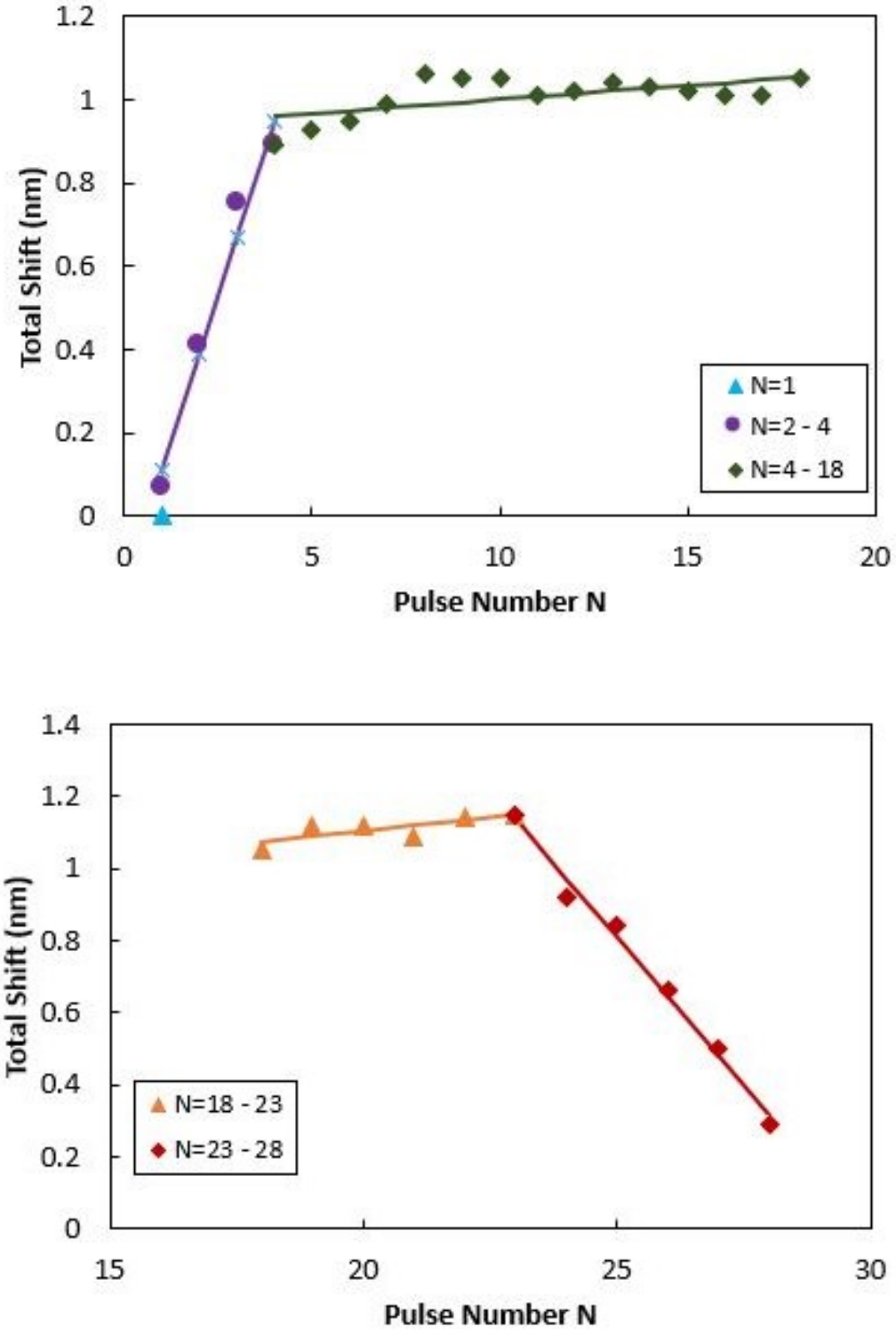

Figure B.10: The accumulated resonance wavelength shifts corresponding to different pulse numbers at a fluence of $0.0431 J/cm^2$.

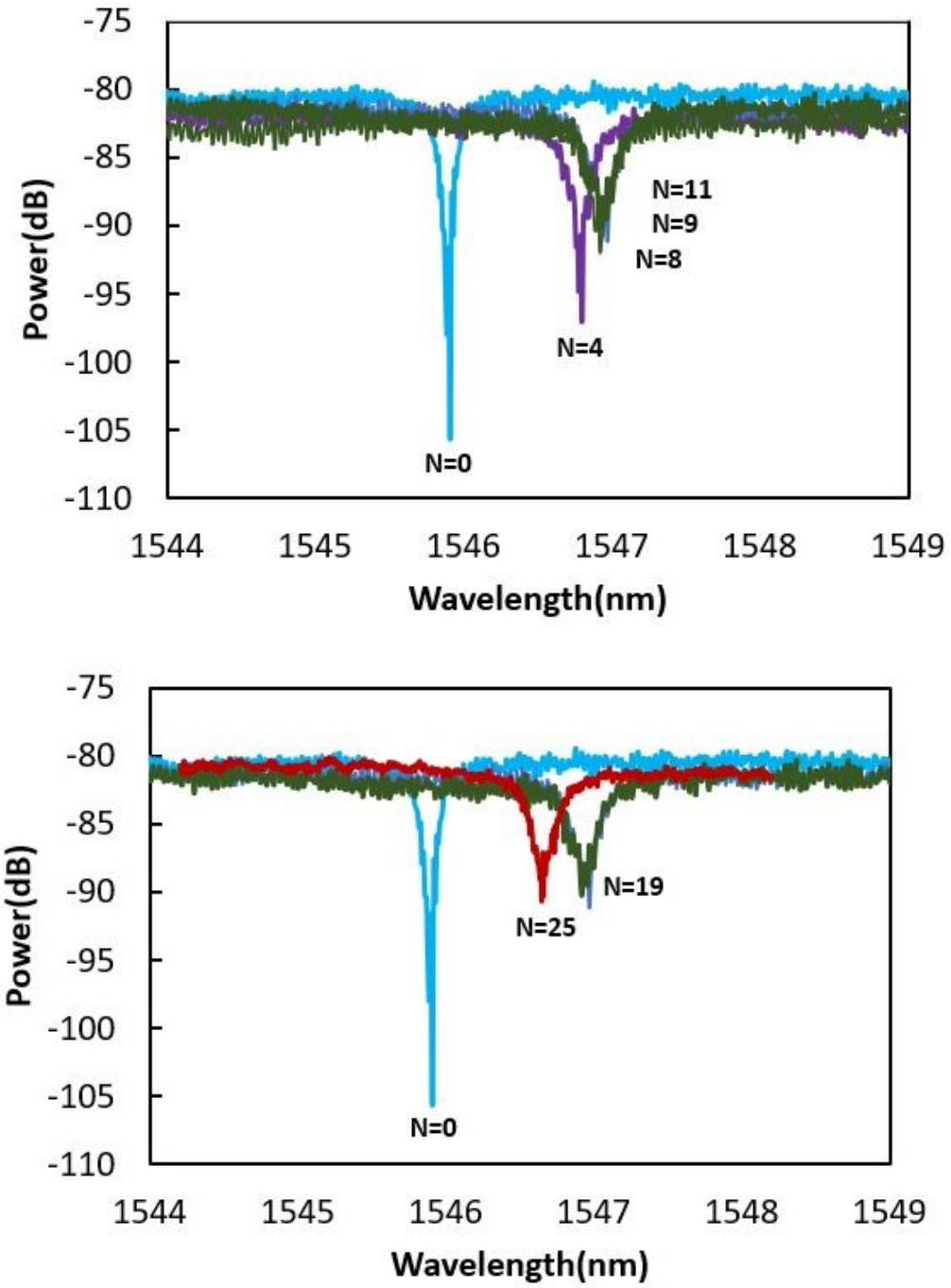

Figure B.11: Example of the spectrum of the accumulated resonance wavelength shifts corresponding to different pulse numbers at a fluence of $0.0431 J/cm^2$. The different colours of the resonance plot represented corresponded to the different regions described in Chapter 6: Region A: Blue; Region B: purple; Region C: Green; Region D: orange; Region E: Red.

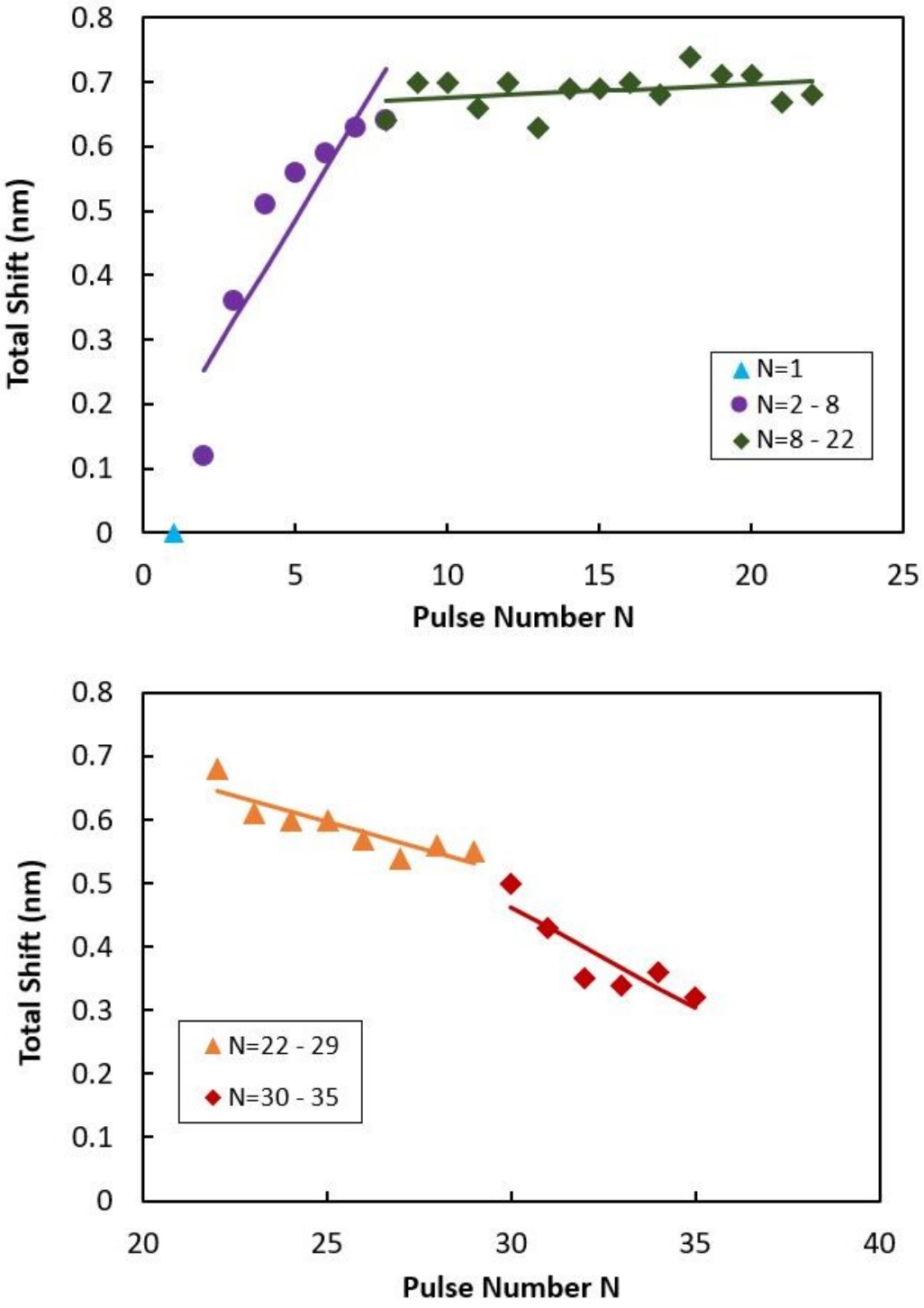

Figure B.12: The accumulated resonance wavelength shifts corresponding to different pulse numbers at a fluence of $0.0452 J/cm^2$.

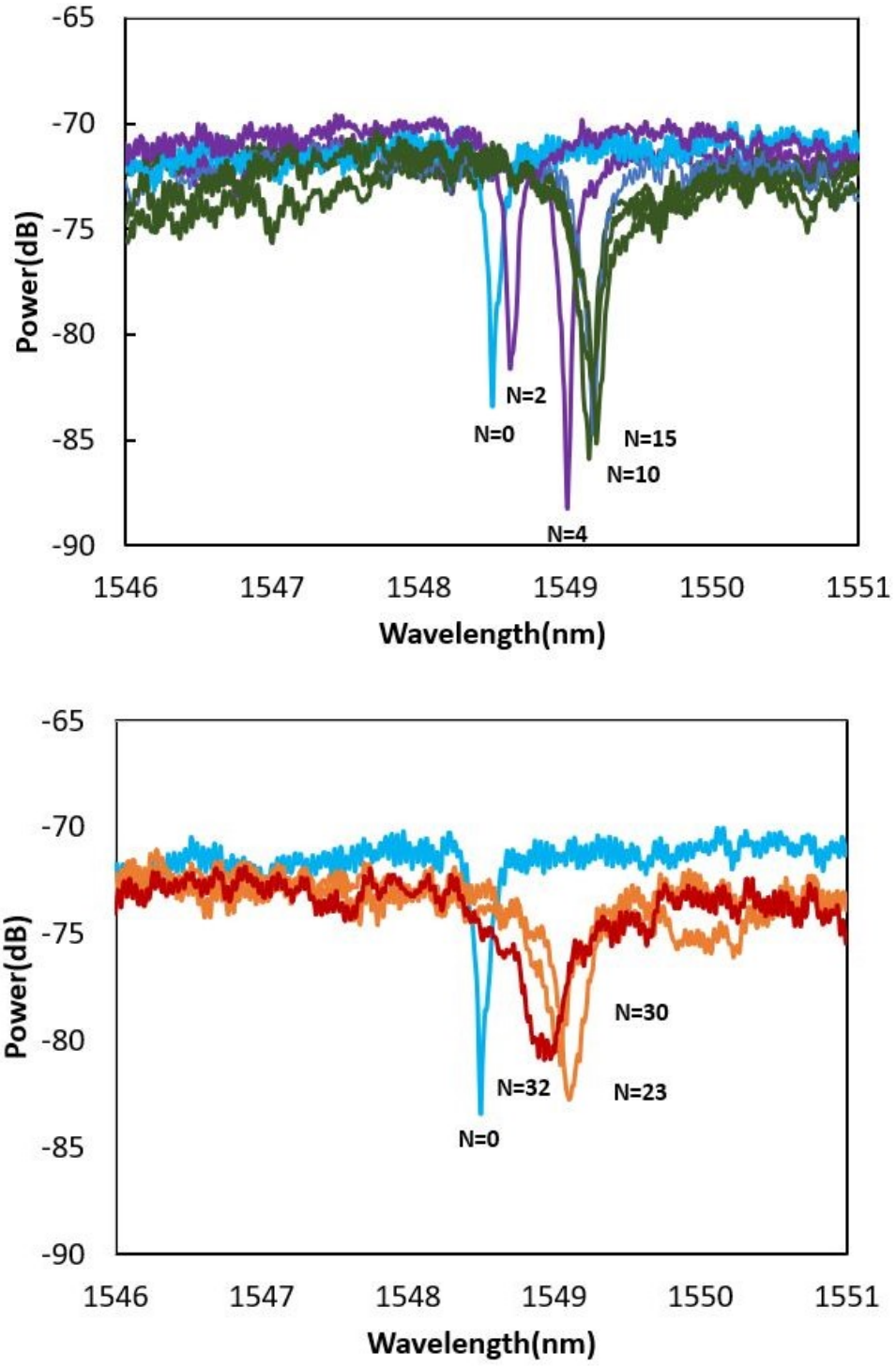

Figure B.13: Example of the spectrum of the accumulated resonance wavelength shifts corresponding to different pulse numbers at a fluence of $0.0452 J/cm^2$. The different colours of the resonance plot represented corresponded to the different regions described in Chapter 6: Region A: Blue; Region B: purple; Region C: Green; Region D: orange; Region E: Red.

Table B.8: Equations representing the data for regions A to E in Fig. B.12

Region	**N**	**Equation** $\Delta\lambda$ is the induced resonance wavelength shift after irradiated by N shots	**Tuning Precision (pm/shot)**
A	1	$\Delta\lambda = 0$	
B	2 - 8	$\Delta\lambda = 0.077857N - 0.097857$	77.8 ± 17.19
C	8 - 22	$\Delta\lambda = 0.002071N - 0.6555$	2.071 ± 1.652
D	22 - 29	$\Delta\lambda = -0.01631N - 1.004643$	16.31 ± 3.401
E	30 - 35	$\Delta\lambda = -0.032N - 1.423333$	32 ± 8.794

Table B.9: Equations representing the data for regions A to E in Fig. B.14

Region	**N**	**Equation** $\Delta\lambda$ is the induced resonance wavelength shift after irradiated by N shots	**Tuning Precision (pm/shot)**
A	1 - 9	$\Delta\lambda = 0$	
B	10 - 19	$\Delta\lambda = 0.053083N + 0.31908$	53.03 ± 2.324
C	20 - 40	$\Delta\lambda = 0.00088N - 0.7136$	0.88 ± 5.2
D	40 - 85	$\Delta\lambda = -0.01993N - 1.514109$	19.93 ± 1.282
E	90 - 100	$\Delta\lambda = -0.046N - 3.686$	46 ± 24.249

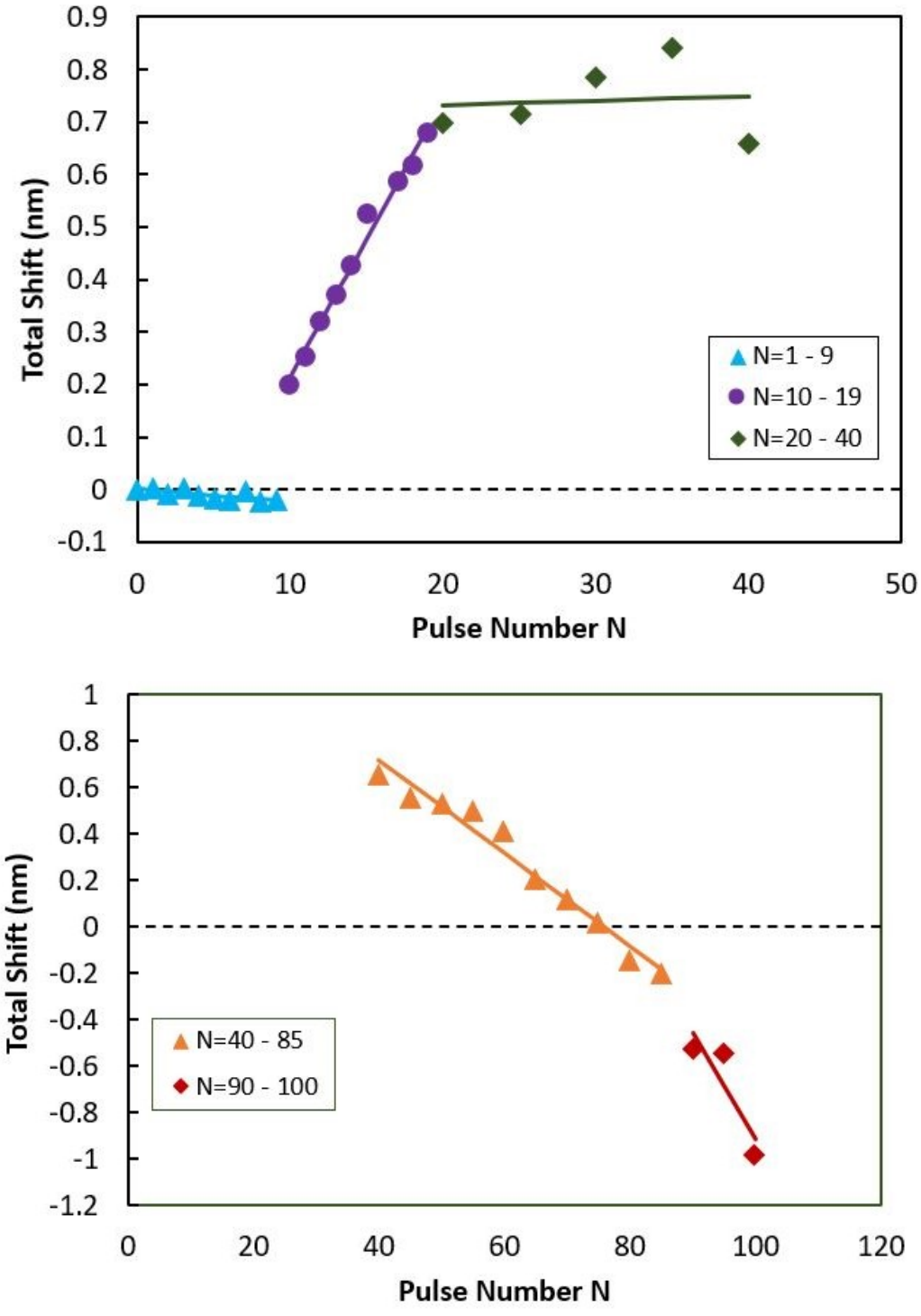

Figure B.14: The accumulated resonance wavelength shifts corresponding to different pulse numbers at a fluence of $0.0453 J/cm^2$.

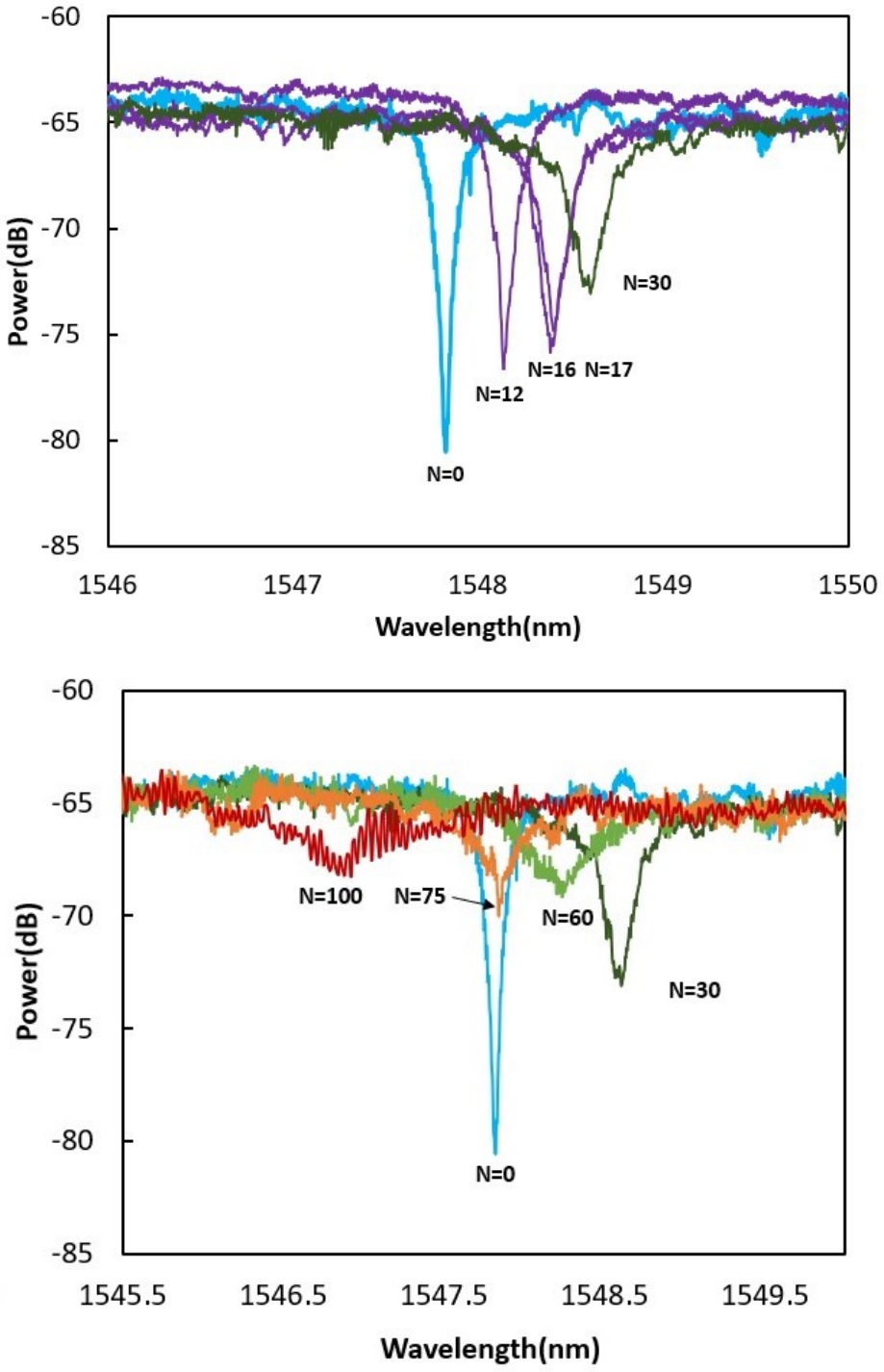

Figure B.15: Example of the spectrum of the accumulated resonance wavelength shifts corresponding to different pulse numbers at a fluence of $0.0453 J/cm^2$. The different colours of the resonance plot represented corresponded to the different regions described in Chapter 6: Region A: Blue; Region B: purple; Region C: Green; Region D: orange; Region E: Red.

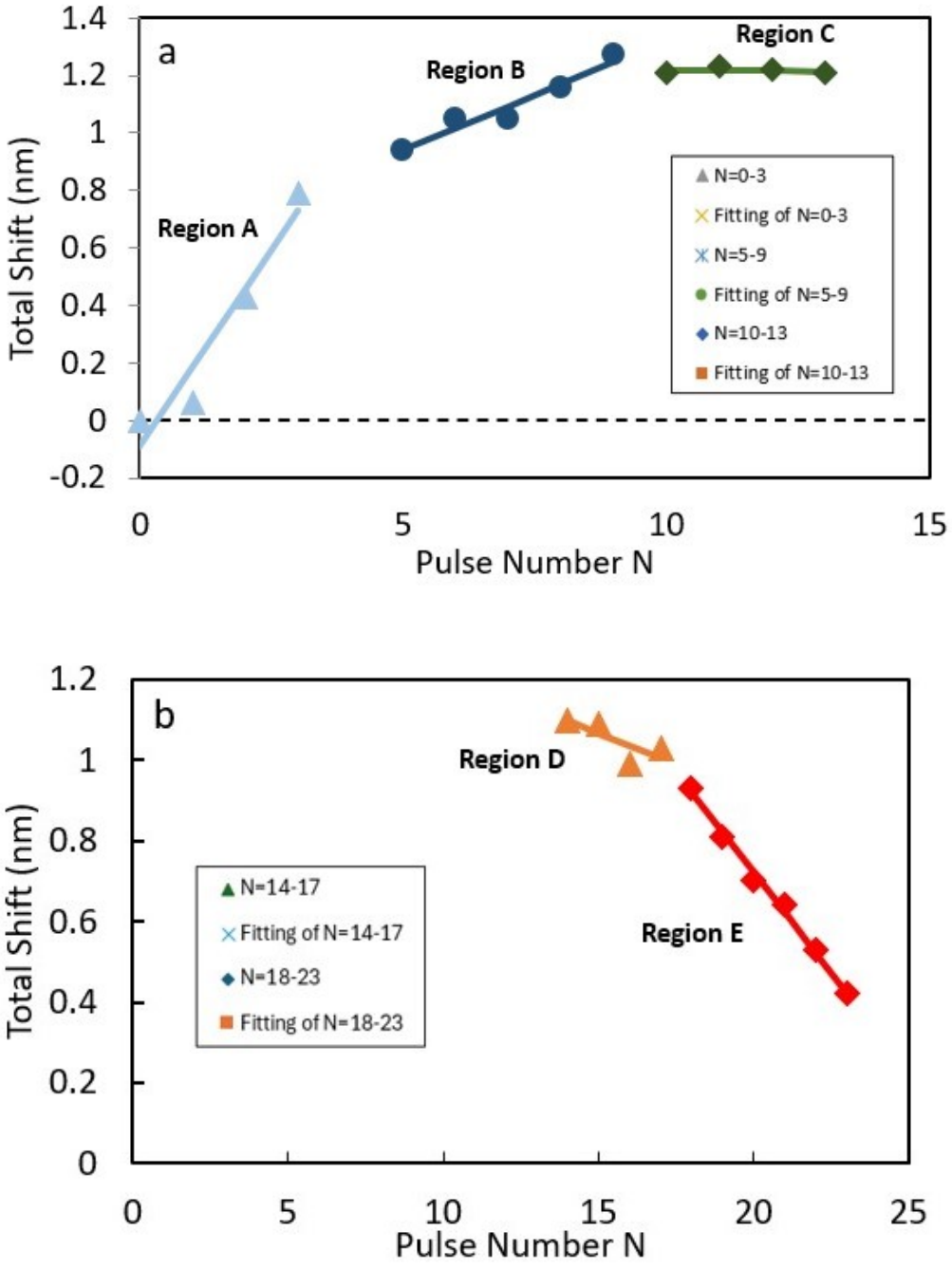

Figure B.16: The accumulated resonance wavelength shifts corresponding to different pulse numbers at a fluence of $0.0502 J/cm^2$.

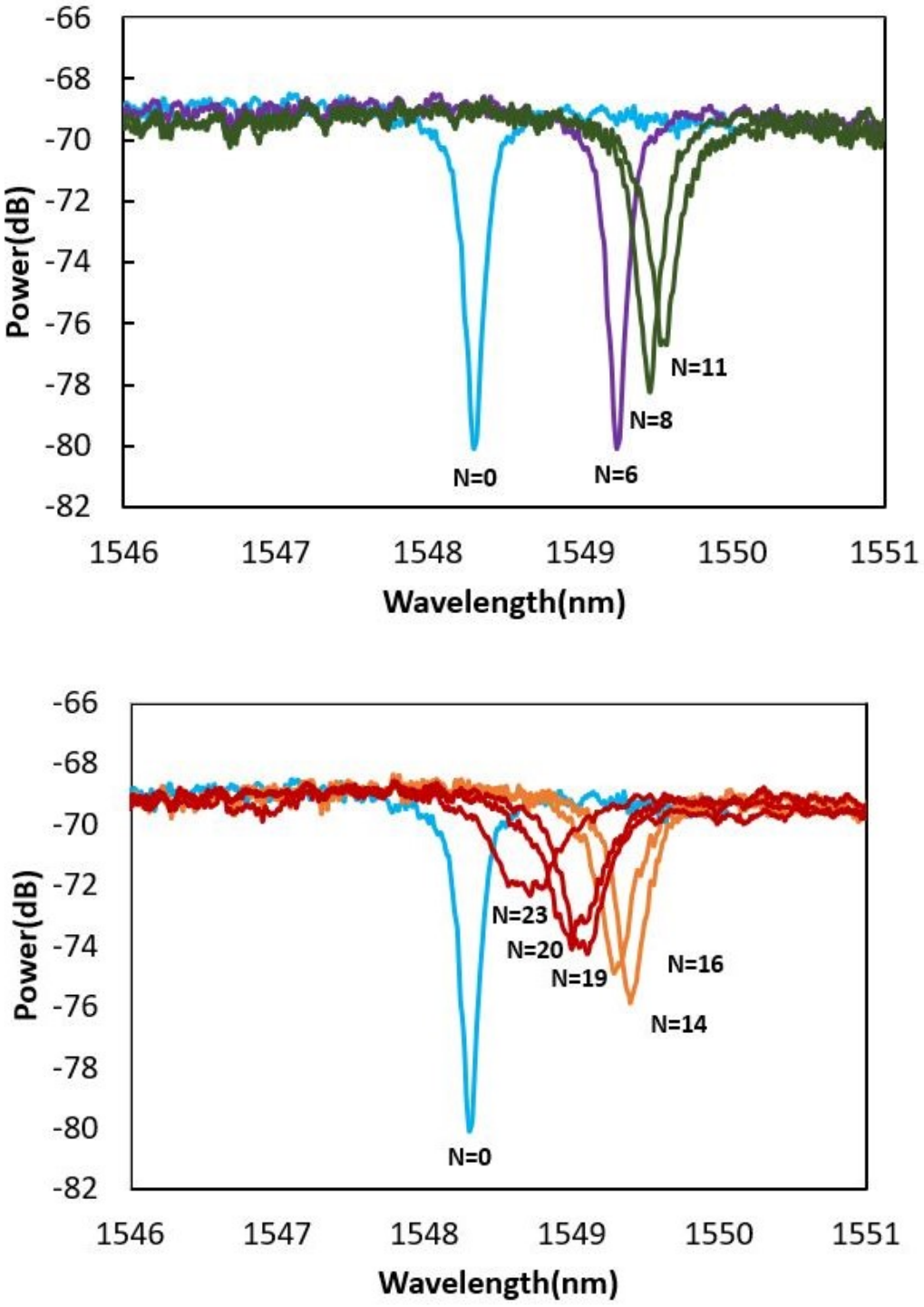

Figure B.17: Example of the spectrum of the accumulated resonance wavelength shifts corresponding to different pulse numbers at a fluence of $0.0502 J/cm^2$. The different colours of the resonance plot represented corresponded to the different regions described in Chapter 6: Region A: Blue; Region B: purple; Region C: Green; Region D: orange; Region E: Red.

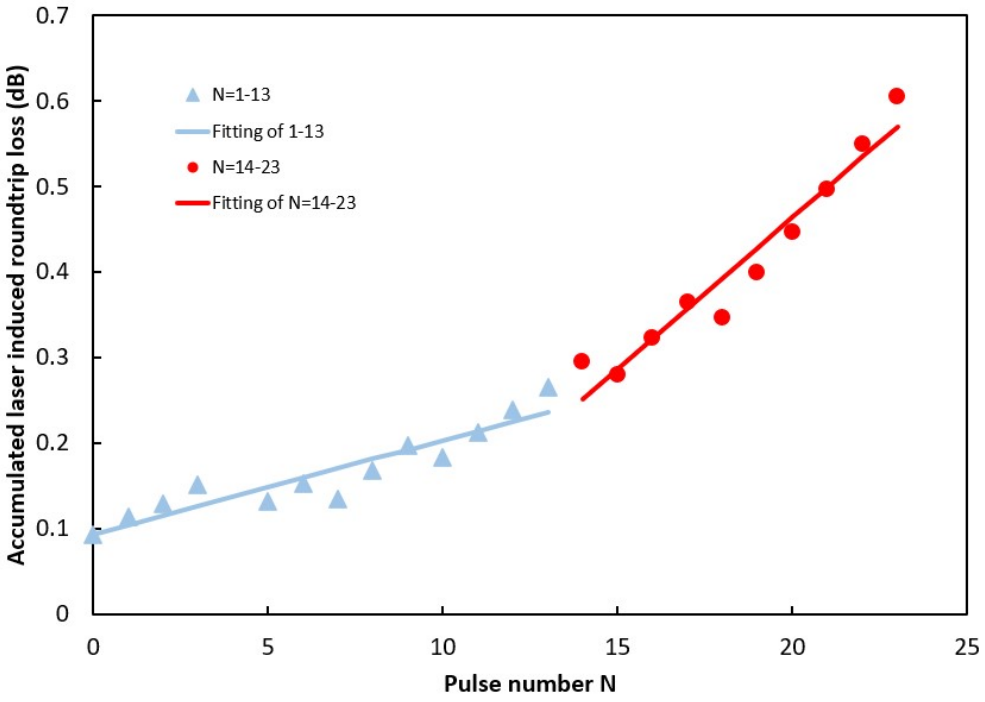

Figure B.18: Induced roundtrip loss of microring resonators as a function of laser pulse number irradiated at a fluence of $0.0502 J/cm^2$.

Table B.10: Equations representing the data for regions A to E in Fig. B.16

Region	**N**	**Equation** $\Delta\lambda$ is the induced resonance wavelength shift after irradiated by N shots	**Tuning Precision (pm/shot)**
A	1 - 3	$\Delta\lambda$ = 0.274N + 0.091	274 ± 52.5
B	5 - 9	$\Delta\lambda$ = 0.077N - 0.555	77 ± 11
C	10 - 13	$\Delta\lambda$ = -0.001N – 1.229	1 ± 5.196
D	14 - 17	$\Delta\lambda$ = -0.031N - 1.533	31 ± 18
E	18 - 23	$\Delta\lambda$ = -0.09857N - 2.6923	98.5 ± 3.869

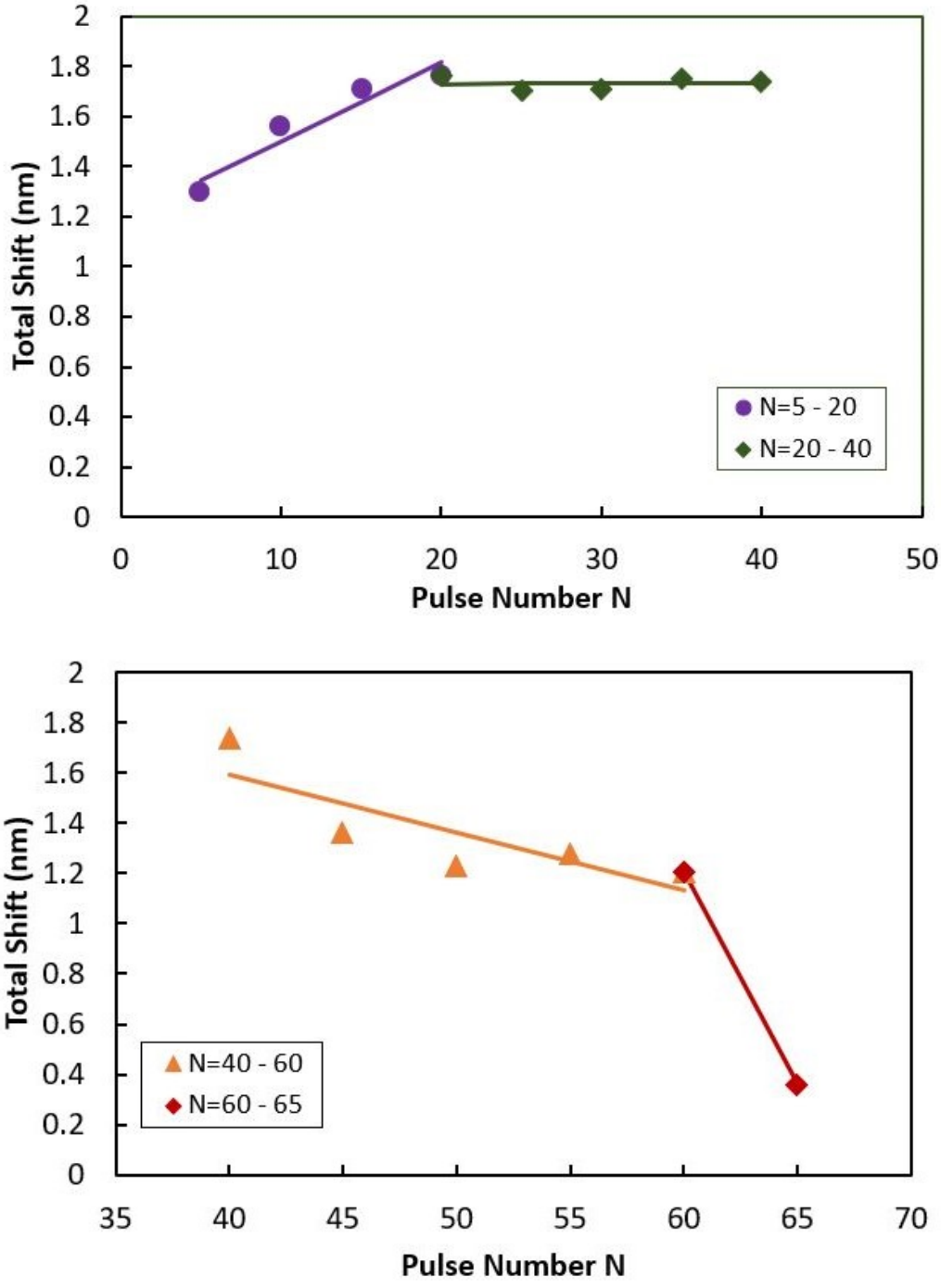

Figure B.19: The accumulated resonance wavelength shifts corresponding to different pulse numbers at a fluence of $0.055 J/cm^2$.

Table B.11: Equations representing the data for regions A to D in Fig. B.19

Region	**N**	**Equation** $\Delta\lambda$ is the induced resonance wavelength shift after irradiated by N shots	**Tuning Precision (pm/shot)**
A	1 - 4	$\Delta\lambda = 0$	
B	5 - 20	$\Delta\lambda$ = 0.0312N - 1.19	31.2 ± 6.963
C	20 - 40	$\Delta\lambda$ = -0.0002N – 1.726	0.2 ± 1.887
D	40 - 60	$\Delta\lambda$ = -0.02288N - 2.5076	22.88 ± 8.934
E	60 - 65	$\Delta\lambda$ = -0.1704N - 11.432	170 ± 0

Appendix C: Supplementary results for shot-to-shot characterization of SiMRR with multi-shot tuning technique with Top-hat Beam profile

In appendix C, supplementary results for the shot-to-shot characterization of the SiMRR using multi-shot tuning technique with top-hat beam profile are shown with fluences ranging from $0.0294 J/cm^2$ to $0.0402 J/cm^2$ respectively. The accumulated resonance wavelength shifts corresponding to different pulse numbers, the spectrum of the accumulated resonance wavelength shifts corresponding to different pulse numbers are provided in this appendix.

F = $0.0294 J/cm^2$: F = $0.0402 J/cm^2$:

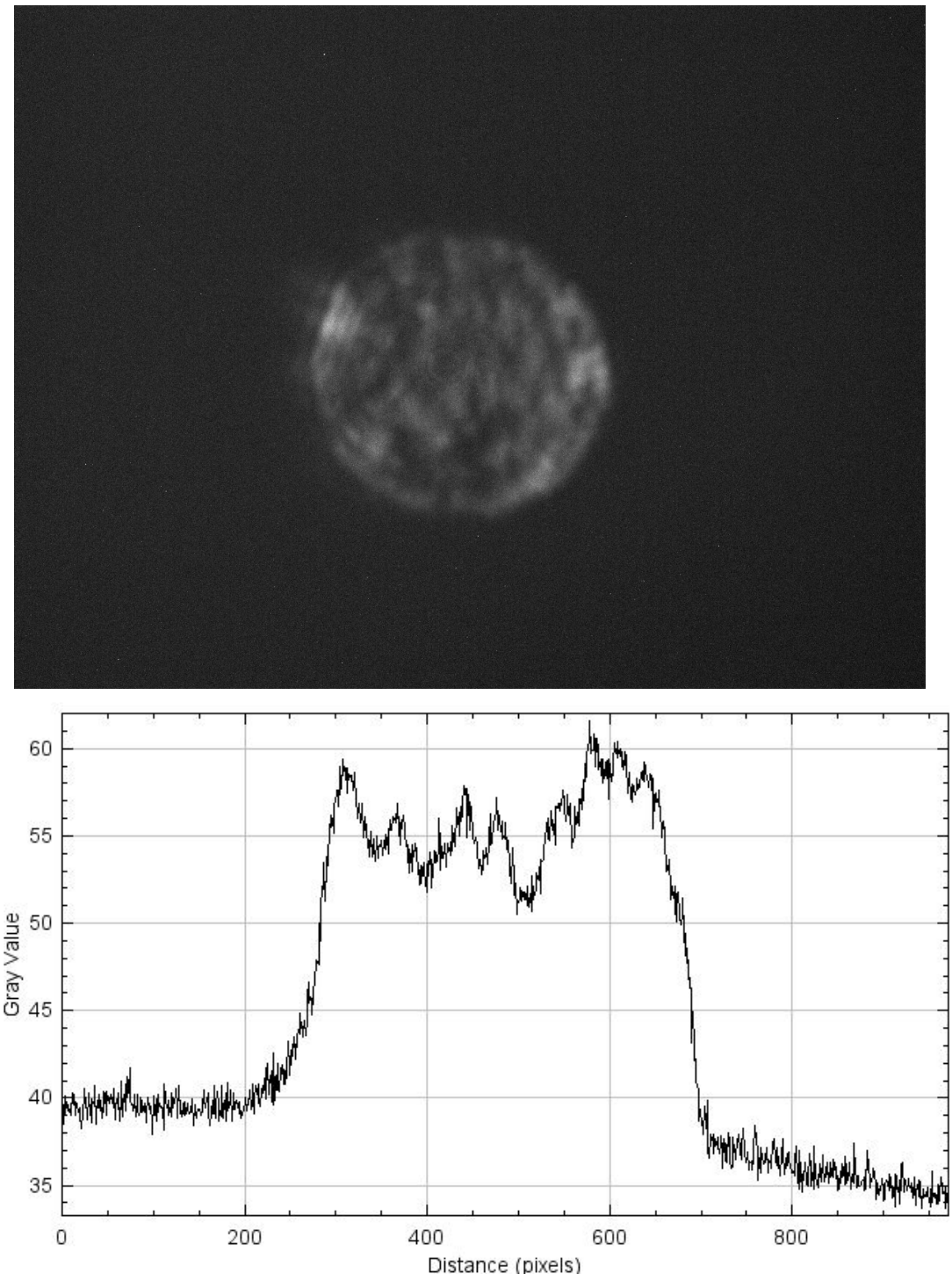

Figure C.1: Example of the Top-hat Beam profile applied in the experiment in Appendex C. (a) The greyscale image of the Top-hat beam obtained from a CCD camera.(b) Corresponded intensity distribution profile of the Top-hat beam.

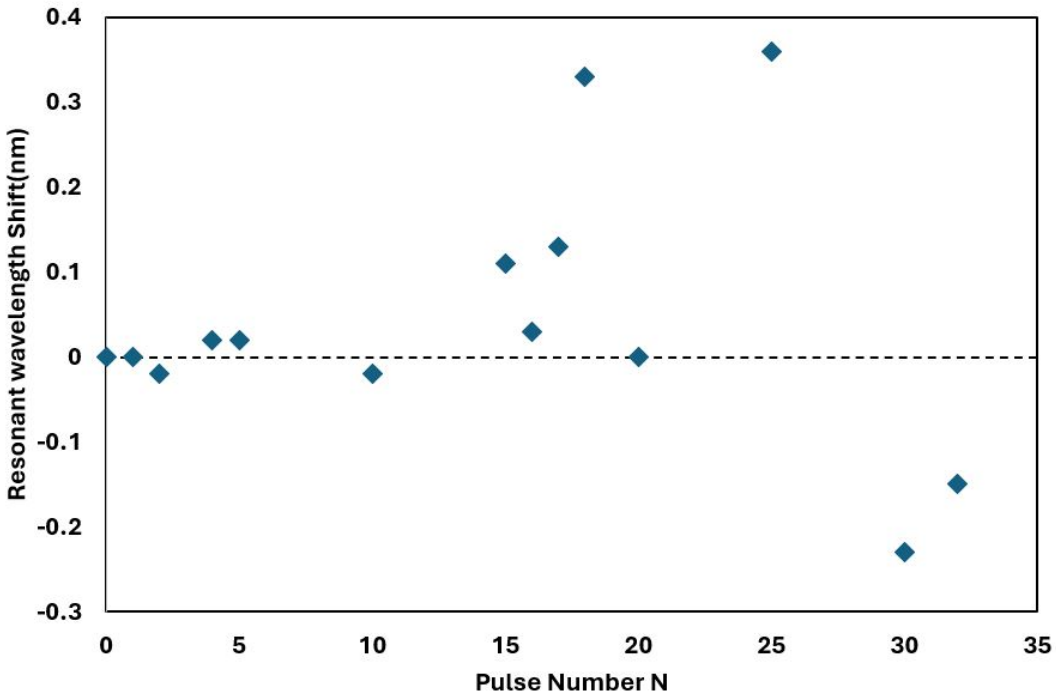

Figure C.2: The accumulated resonance wavelength shifts corresponding to different pulse numbers at a fluence of $0.0294 J/cm^2$.

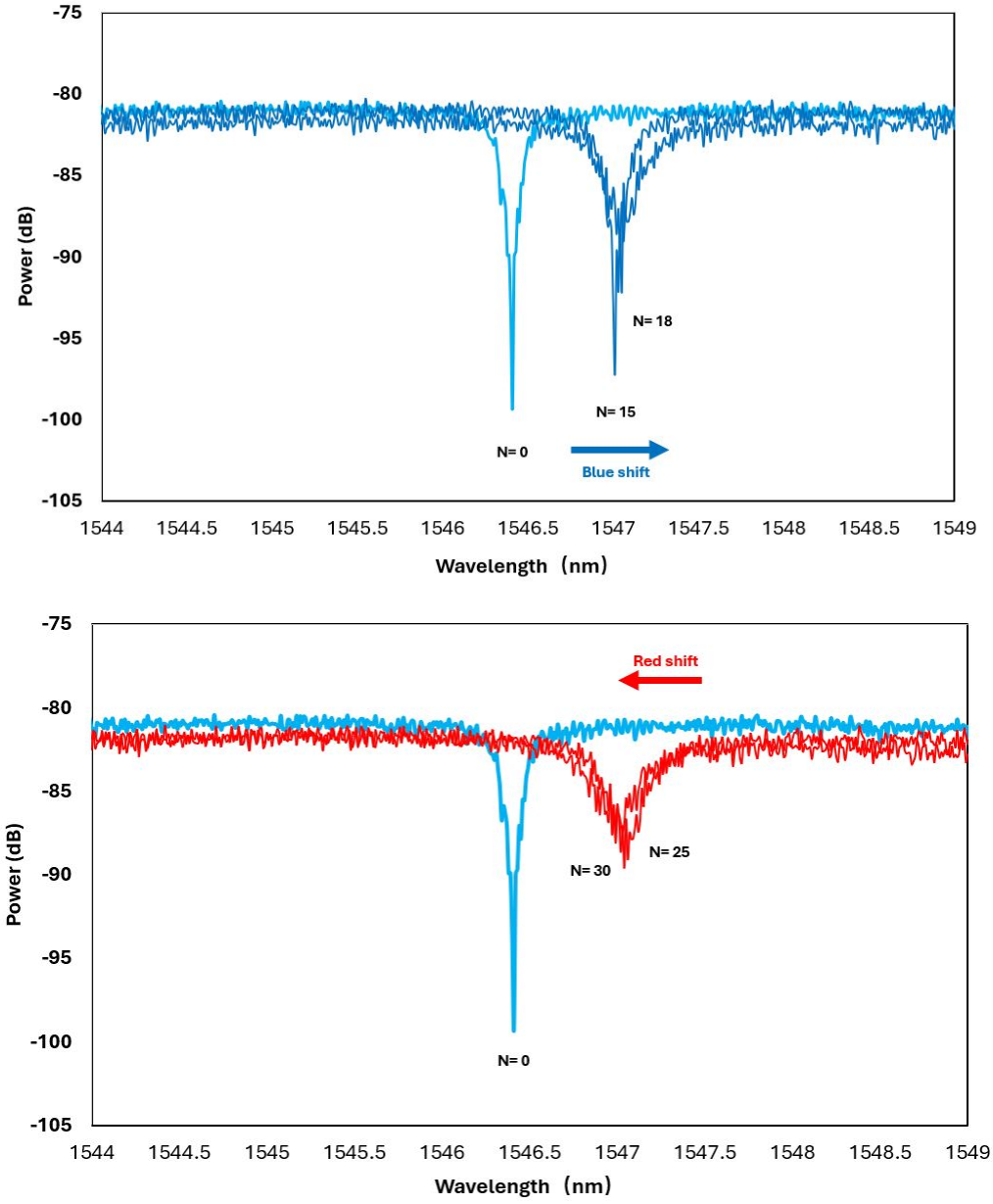

Figure C.3: Example of the spectrum of the accumulated resonance wavelength shifts corresponding to different pulse numbers at a fluence of $0.0294 J/cm^2$.

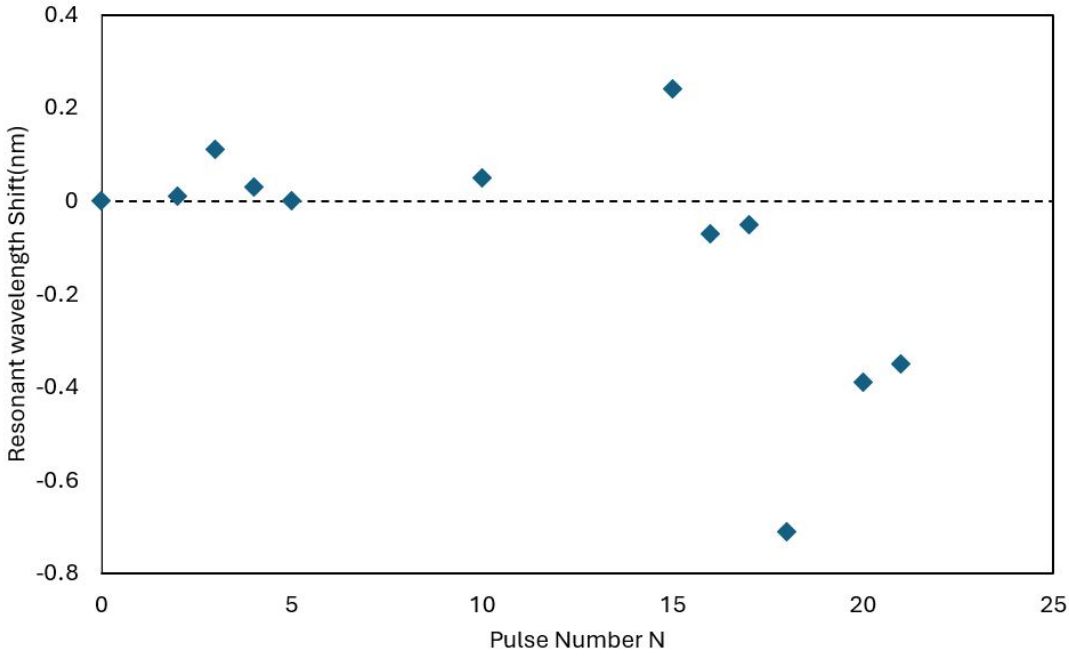

Figure C.4: The accumulated resonance wavelength shifts corresponding to different pulse numbers at a fluence of $0.0402 J/cm^2$.

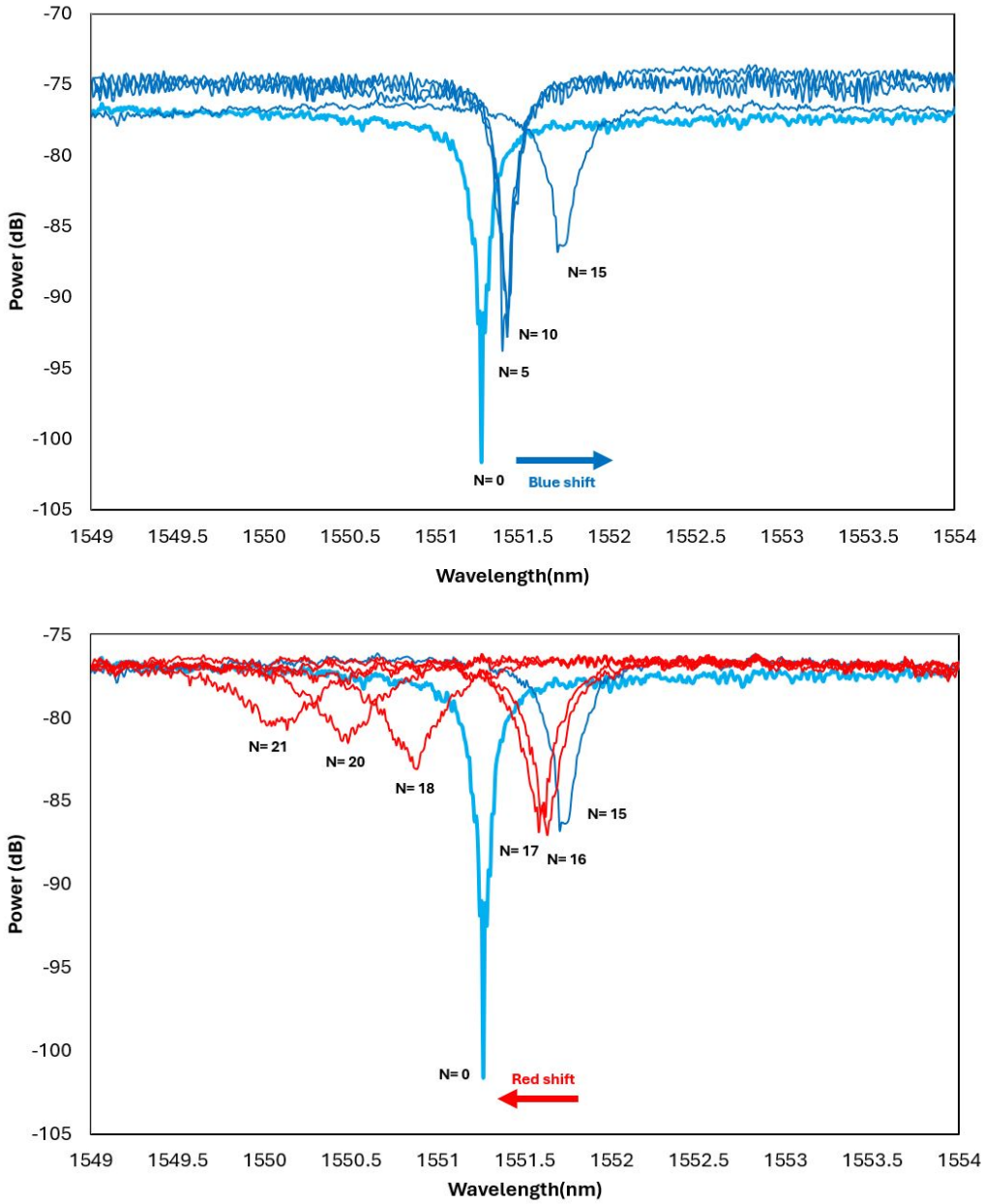

Figure C.5: Example of the spectrum of the accumulated resonance wavelength shifts corresponding to different pulse numbers at a fluence of $0.0294 J/cm^2$.